DEVELOPMENT OF MULTI-FUNCTIONAL POLYMERIC NANOPARTICLES AS DRUG DELIVERY VEHICLES TARGETING BACTERIAL BIOFILMS AND HEREDITARY HEMOCHROMATOSIS

by

SHUOLIN CUI

(Under the Direction of May P. Xiong)

ABSTRACT

Polymeric nanoparticles (PNs) including stimuli-responsive nanoparticles, as drug delivery systems, have gained much attention for the last several decades due to their ability to overcome the limitations of conventional therapeutic approaches. These nanoparticles are not only able to protect the active pharmaceutical ingredients (APIs), but they can also release the drugs in response to endogenous and exogenous stimuli, which improves therapeutic efficacy and minimizes adverse effects of the drugs. While stimuli-responsive nanoparticles are used in diverse therapeutic areas, the application of these nanoparticles is an especially advantageous strategy in combating bacterial infections and metabolic syndromes such as iron overload diseases, where the complications particularly accompany the production of specific stimuli such as pH, enzymes, reactive oxygen species (ROS), and toxins. In bacterial infections caused by planktonic bacteria, intracellular bacteria, and bacterial biofilms, stimuli-responsive nanoparticles can take advantage of the stimuli released from the infected areas to overcome both antimicrobial resistance (AMR) and diffusion

retardation to enhance the efficacy of antibiotics. In iron-overload disease, where the excess amount of iron accumulation causes multiple organ failure, polymeric nanoparticles can improve bioavailability and blood circulation and pharmacokinetic profiles of iron chelating agents, as well as reduce potential toxicity through target specificity and controlled release properties. In this dissertation, the effectiveness of polymeric nanoparticles as drug-delivery vehicles was investigated. Firstly, a pH-responsive nanoparticle for eliminating bacterial biofilm was studied. Secondly, an orally non-absorbable nanogel-DFO conjugate was evaluated as a potential long-term safe prophylactic treatment in reducing dietary iron absorption for hereditary hemochromatosis.

INDEX WORDS: Polymeric nanoparticles, stimuli-responsive, pH-responsive, Biofilm, Polyethylene glycol (PEG), Hereditary hemochromatosis, Iron chelation, Nanogel, Non-absorbable, Deferoxamine (DFO)

DEVELOPMENT OF MULTI-FUNCTIONAL POLYMERIC NANOPARTICLES AS DRUG

DELIVERY VEHICLES TARGETING BACTERIAL BIOFILMS AND HEREDITARY

HEMOCHROMATOSIS

by

SHUOLIN CUI

B.S. Yonsei University, Seoul, South Korea, 2012

M.S. Yonsei University, Seoul, South Korea, 2014

A Dissertation Submitted to the Graduate Faculty of The University of Georgia in Partial

Fulfillment of the Requirements for the Degree

DOCTOR OF PHILOSOPHY

ATHENS, GEORGIA

2023

DEVELOPMENT OF MULTI-FUNCTIONAL POLYMERIC NANOPARTICLES AS DRUG

DELIVERY VEHICLES TARGETING BACTERIAL BIOFILMS AND HEREDITARY

HEMOCHROMATOSIS

by

SHUOLIN CUI

Major Professor:	May P. Xiong
Committee:	David Crich
	Jin Xie
	Yao Yao

Electronic Version Approved:

Ron Walcott
Vice Provost for Graduate Education and Dean of the Graduate School
The University of Georgia
May 2023

ACKNOWLEDGMENTS

TABLE OF CONTENTS

CHAPTER

LIST OF TABLES

LIST OF FIGURES

CHAPTER 1

INTRODUCTION

The demand for developing novel vehicles in the area of drug delivery has been increasing over the past couple of decades due to surges in complexity of certain complications such as cancer and the limitations of conventional therapeutic agents. Drug delivery, or the drug-delivery system (DDS) is an area of designing and developing effective formulations through utilizing diverse approaches including synthetic polymers, lipid nanoparticles (LNPs) and inorganic materials. Major advantages of introducing DDS include protection of the active pharmaceutical ingredients (APIs), improving pharmacokinetic (PK) profiles, delivery to targeted areas, and reduction of potential toxicity of the APIs. Over the past two decades, since there has been numerous research focused on minimizing potential risks and enhancing therapeutic efficiencies of using formulations, the delivery systems have become increasingly sophisticated and complex, primarily focusing on enhanced controlled release of APIs, specificity in targeting, and avoiding adverse effects while maintaining therapeutic efficacy. In the sense technologies in designing and fabricating nanoparticles have gained much attention since nanoparticles potentially could be used as effective delivery systems.[1]

Conventional synthetic therapeutic agents such as small molecules and natural product extracts have been used for decades to treat various diseases. Nowadays, biopharmaceutical agents including peptides, proteins, monoclonal-antibody (mAbs) and RNAs have also been widely developed and used for treating certain types of diseases such as immune-related cancers and

1

neurodegenerative disorders that are difficult to treat with conventional methods such as small molecules. Nonetheless, there are limitations in utilizing these APIs to achieve acceptable therapeutic outcomes. The limitations of using these APIs, particularly biological ingredients, may include poor pharmacokinetic (PK) profile, lack of diversity in route of administration, metabolic instability, drug-induced toxicity, and lack of target specificity. Therefore, a surge in need to overcome such drawbacks of these agents have led scientists to develop more effective drug delivery systems, which has led to the development of several different types of polymeric nanocarriers (PNs) to enhance drug biodistribution, efficacy, and safety profiles. [2-5]

There are several types of frequently used polymeric nanoparticles (PNs) both for labs and clinical applications, particularly with the expectation of their functions in both diagnostics and therapeutics (**Table 1.1**). These PNs function as carriers for the APIs to provide improved PK profiles through conjugation with the hydrophobic/hydrophilic moieties of drugs to further enhance systemic biodistribution, efficacy of the drugs, and as well as targeted and controlled release. As a result of such functionalities, these PNs are capable of reducing the risk of potential drug-induced toxicity and enhancing the stability of the drugs to withstand degradation and hydrolysis by the cellular microenvironment and enzymes. [3, 6] Among a number of various types of PNs, most frequently used PNs may include polymeric micelles (PMs), nanogels, and polymeric capsules (PCs), hydrogels (HGs), and liposomes. Typically, the sizes of PNs that are reported to have therapeutic significance range from 10 nm to 300 nm depending on the type of polymers and the monomers. [7, 8] Since there are different kinds of APIs, the selection of NPs is primarily contingent on the type of payload, administration route, and expectations for desired therapeutic effects.
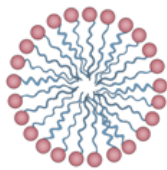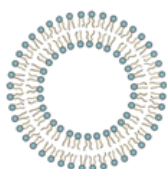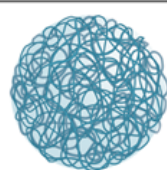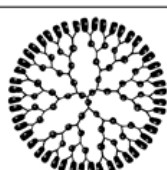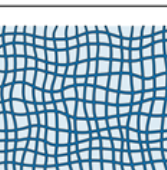
1.1 Multifunctional Polymeric Nanoparticles

Applications of conventional therapeutics has brought up cautions of lack of efficacy, side effects and lack of target specificity, a number of attempts have been made to develop and optimize actively participating stimuli responsive PNs for the delivery systems for clinical applications. Physiological stimuli are factors that can be produced by cellular pathways such as inflammation, and these stimuli are usually tissue specific. Types of stimuli include pH, reactive oxygen species (ROS), enzymes, and redox, and compared to healthy tissues, these stimuli are overexpressed and overproduced in certain diseases such as bacterial infections, cancers, and other metabolic syndromes. Thus, designing stimuli-responsive DDS is advantageous in enhanced targetability and controlled release of the cargos. In addition, due to the specificity, stimuli responsive PNs offer reduced administration dosage frequency, targeted delivery, and increased circulating time of the drugs in physiological conditions. [9, 10] Commonly used stimuli-responsive NPs include polymers that are sensitive to endogenous ROS, pH, cellular enzymes, and redox. For an example, pH-responsive NPs are commonly used for targeting cancers because pH is one of the overproduced stimuli in the tumor microenvironment, where the pH of the tumor cells ranges from 6.0 to 6.5, and this range is lower than extracellular regions of normal tissues and blood (pH 7.4). Design of such PNs is based on introducing pH-responsive moieties or monomers as building blocks, in which the PNs are stable and maintain morphological structure under normal pH but susceptible to degradation or structural instability when pH decreases, thus allowing targeted delivery and controlled release of the payload to the tumor area. This pH-responsive property allows slow release of drugs in the target area to further prevent drug tolerance and cancers from developing multidrug resistance. [11, 12] Other stimuli such as reactive oxygen species (ROS) are produced from mitochondria and

endoplasmic reticulum (ER) by NADPH oxidase in organs such as liver due to inflammation or tissue damage, and typical types of ROS include hydrogen peroxide (H_2O_2), superoxide (O_2^-), and hydroxyl radicals (HO•). In cancer or metabolic syndromes such as iron overload diseases, the production of ROS is one of the apparent physiological factors that the cellular systems report. [10, 13] Therefore, similar to pH-responsive NPs, ROS-sensitive PNs have also gained attention for the application as a stimuli-responsive delivery system, with similar advantages and characteristics in enhancing targetability and controlled drug release. As an example of the application of ROS for iron overload diseases, Liu et al. have reported utilizing thioketal-linked ROS-responsive PNs as degradable carriers, which provided a safer, long-circulating, and enhanced iron-chelating ability. [14] Both the pH and ROS-responsive PNs are also used in infectious diseases such as bacterial infections. Similar to cancers, bacterial infections induce inflammations to produce ROS, and depletion of nutrients at the infected sites generates low pH microenvironment, which is suitable for the application of stimuli responsive PNs for enhanced therapeutic outcomes. [15, 16] Similar to pH or ROS, enzyme responsive PNs are enzymatically cleavable which react to specific types of enzymes such as proteases, phospholipases, and oxidoreductases, which are typical overexpressed biological factors in diseases such as cancer. [17] The enzyme-responsive PNs have advantages in delivering biological agents such as genes, where the targeted site is intracellular and cell-specific rather than organ specific. Enzyme-responsive nanoparticles include lipid-based liposomes or lipid nanoparticles (LNP) with surface modification using synthetic moieties to enter cells since it is essential to complete the delivery inside cells due to the nature of gene therapies. Redox-responsive PNs use disulfide linker in the carrier that is sensitive to reductive activity and can be readily cleaved by thiol species such as tripeptide GSH, where the concentration is significantly elevated in diseases such as

neurodegenerative disorders, liver diseases, diabetes, and cancers. [18-20] Overall, multifunctional polymeric nanoparticles (PNs) have been developed to enhance the bioavailability and efficacy of the therapeutic agents with the properties of responding to certain stimuli such as pH, ROS, and enzymes allowing controlled releases and enhanced targeted delivery.

Table 1.1: **Summary of Diverse Polymeric Nanoparticles (PNs)**

Types of NP	Features	Sizes	Advantages	Limitations
Polymeric micelles	Self-assembled formation of both hydrophilic and hydrophobic copolymers	10 – 100 nm	Controlled release of hydrophobic drugs; Increases long blood circulation time;	Limited number of polymers that be used; Not always stable; Some polymers may induce immunological responses;
Liposomes	Lipid-bilayer membrane vesicles with aqueous core	100 – 200 nm	Able to entrap both lipophilic and hydrophilic compounds; Preventing compounds from degradation; Surface modification;	Unstable, vulnerable for metabolic degradation in the liver; Not suitable for scale-up;
Nanogels	Monomers crosslinked with polymers containing firm backbone	50 – 200 nm	Preventing degradation of drugs; Sustained drug release; Increases PK profiles of drugs; Enables surface modification for Biocompatible and safe;	Difficult in size control; Low cell permeability; Limited targeted delivery; Charged surface may induce toxicity;
Dendrimers	Branched and symmetrical identical molecules	< 10 nm	Precise molecular weight; Increased permeability; Targeted drug delivery; Decreases immunological interaction;	Polycationic surface induces toxicity; Uncontrolled release of drugs; Lack of cleavable ability at target site;
Hydrogels	A network of hydrophobic polymer chains as a colloidal gel	-	High absorbability; Biocompatible; Convenient;	Difficult to quantify dosage; Limitation in controlling drug loading; Low drug loading efficiency; Amino moiety induces toxicity;
Polyrotaxane	A mechanically interlocked molecule consisting of multiple rings and bulky caps	-	Bulky caps enable controlled release of compounds; Relatively small size enhances cell permeability;	Low bioavailability; Low drug loading efficiency; Difficult to scale-up;

1.2 Bacterial and Biofilm Infections

Antimicrobial resistance (AMR) is rapidly becoming a major healthcare security challenge with its ties to complications such as persistent chronic wound infection, surgical site infection, and sepsis. The global prevalence of AMR-associated fatality is expected to exceed 10 million by 2050, and this staggering projection is in large part due to the formation of biofilm, a lifeform of surface-related communities of bacterial cells that serves as a major obstinate fortress against antibiotics [21] The link between AMR and biofilm is made more evident by the fact that biofilm is capable of developing 100 to 1000 times more antibiotics resistance in comparison to the same strain of planktonic cells, which highlights the need of a method of effectively eradicating biofilm in order to reduce such risk of drug resistance. [22] Biofilm is formed when adhesion of bacteria to surfaces prompt the production of a stringy and complex network called the extracellular polymeric substances (EPS), which is composed primarily of proteins, lipids, polysaccharides and extracellular DNA (eDNA), as well as amyloids, cellulose, fimbriae and flagellae. [23, 24] Inside the biofilm, pores and channels between the microcolonies facilitate the transport of rudimental substances for bacterial growth, which contributes to biofilm's rapid growth and migration. [25] In the case of UTI, bacterial uropathogens such as *P. aeruginosa* and *E. coli*, which contribute to 90% of the total infections, harbor and colonize urinary mucosal surfaces to form biofilms and overcome the host defense mechanism to cause persistent and chronic infections. These pathogens belong to a category of bacteria called the ESKAPE (*E. coli, S. aureus, K. pneumoneae, A. baumanii, P. aeruginosa and Enterobacter pp*), a group of highly problematic pathogens linked to extensive multi-drug resistance (MDR) and recurrence in nosocomial infections. They are known to inhibit the entering of antibiotics through the EPS matrix of their biofilm, which in turn allows

6

bacteria within the biofilms to develop heterogeneous phenotypes for survival and escape from chemotherapy. [26, 27] This difficulty in treatment is especially concerning in the light of the fact that biofilm infection-associated sepsis is one of the leading causes of death worldwide, with urinary tract infection (UTI) contributing to 27 % of total sepsis cases, with this number increasing to 42% in post-surgery hospitalized patients, and this underlines an urgent need for new therapeutic approaches to eliminate biofilm for the treatment of UTI. [28, 29]

1.3 Current Approaches and Limitations

Antibiotics being susceptible to biofilm-mediated resistance is largely due to EPS, since antibiotics are likely to bind to components within the EPS matrix or be degraded by the enzymes in the biofilm. [26] As a result, only a small percentage of the antibiotics enter the biofilm, rendering the treatment ineffective in fully eradicating the bacteria, which in turn leads to drug resistance. In terms of *P. aeruginosa* and *E. coli* biofilms induced UTI, there has been a limited number of studies on elimination of the biofilms, however, they have faced multiple drawbacks. While decades of antibacterial research has enabled the use of antibiotics, such as beta-lactam drugs, quinolones and aminoglycosides, to target bacteria, diffusion-reaction of traditional antibiotics are limited due to both reaction with the EPS and chelation and degradation by bacterial enzymes. As a result, only a sublethal concentration diffuses inside, which ultimately leads to selection for tolerance and resistance of bacteria within the biofilm. [26, 30] It is also important to note that reduced antibiotic susceptibility of the biofilms contributes to exacerbation of the symptoms in UTI, especially in patients with implanted devices such as urethral catheter, and as the symptoms aggressively progress, planktonic cells from biofilms undergo migration and re-

adhesion to surrounding organs, such as bladder and kidney, which makes it more intractable to fully eradicate the biofilms and to treat infections. [28] Although the concept of nanoparticles has been actively used in healthcare sciences, studies regarding their antibacterial application are limited to inorganic nanoparticles and their efficacy in its elimination of planktonic bacteria. They have yet to be proven to be effective in the case of biofilm. Furthermore, while a small number of studies have been conducted on targeting biofilm using polymeric nanoparticles (PN), an organic form of nanoparticles, these approaches primarily focus on repelling bacterial adhesion and inhibiting biofilm development, which not only face the issue of cellular toxicity, but are also inapplicable for eliminating preexisting biofilms. Moreover, while a few other research presented approaches using either functionalized small molecule agents or PNs to eliminate preexisting biofilms, the ability of these PNs to diffuse into biofilm is yet to be discovered. [30, 31]

1.4 Proposed Strategies to Combat Biofilms

Therefore, there is a need to develop a method to (i) limit the interaction between antibodies and EPS to effectively deliver antibiotics to the biofilm microenvironment and (ii) ensure controlled release of antibodies only within the confines of the microenvironment. Efforts to overcome these limitations and combat ESKAPE biofilms without using high-dosage chemotherapy, which is linked to significant adverse effects and emergence of multi-drug resistant strains [32], include: (i) proteins and antibodies to target EPS components such as eDNA, proteins and polysaccharides [31]; (ii) functionalized materials with bacteria-repelling ability to prevent biofilm formation; (iii) materials bearing ability to eradicate preexisting biofilm. Among those strategies, nanoparticles, such as inorganic metal oxide NPs, liposomes and hydrogels, are widely

8

used for the purpose of overcoming limitations of mono-chemotherapy and are characterized by surface/chemical modifications for the elimination of bacteria and delivery of antibiotics. [33-36]. However, they are limited by their lack of efficacy, instability of the material, low solubility, poor PK profiles, damages to surrounding non-bacterial cells and limited clinical applications, and this has led to a need for a more effective therapeutic strategy [30, 37-39].

Our group previously reported constructing several stimuli-responsive PNs and such stimuli include reactive oxygen species (ROS), enzyme, and oxidation for controlled release of drugs [40-42]. Based on the reporting and the information that these PNs have been widely studied for diseases including cancer, hemochromatosis, and inflammatory syndromes [9, 40, 41], stimuli-responsive PNs were chosen as a viable candidate for this project, since these multi-functional PNs are capable of flexible surface modification, protection of drug, enhanced drug loading efficiency, reduction in potential toxicity and increasing drug efficacy through controlled release.

We designed **mPEG-*b*-p(DEAEMA)**, a novel pH-responsive multifunctional **Polymeric Vesicle (PV)** that has advantages in not only controlled release of the drug in specific conditions, but also in successful diffusion into the inner biofilm microenvironment. The PEG backbone of the carrier enables inhibition of non-specific absorption and adhesion to EPS components for enhanced permeability [43] to inside the biofilm, and it is also a biocompatible safe agent in drug delivery with non-biodegradability which enhances the structure of the nanocarrier and protection of encapsulated drugs [44]. The monomer DEAEMA is a pH-responsive molecule that is responsible for pH-stimulated drug-release. Under acidic conditions, the tertiary amine becomes protonated to form quaternary amine to make DEAEMA hydrophilic, which allows swelling and

morphological transformation of the carrier and grants positive charges to the carrier [45]. This pH-responsive mechanism of the carrier enables controlled release of encapsulated antibiotics inside the biofilm, which will eventually exhibit enhanced anti-biofilm efficacy. In addition, polymerization of such monomers and backbones will lead to generation of the amphiphilic vesicle, which is water-soluble and also allows encapsulation of both hydrophilic and hydrophobic antibiotics, and considering most antibiotics are hydrophilic, this particular property makes **PV** a better option than using other types of PNs such as micelles, which can only load hydrophobic agents. Additionally, although initially a neutral-charged nanovesicle **PV** will be given positive-charge inside the acidic biofilm microenvironment due to protonation of p(DEAEMA), which will result in significantly promoted binding and attachment to bacterial membrane as well as increased antibiotic efficacy.

1.5 Hereditary Hemochromatosis

Iron is an essential element that contributes to a number of cellular signaling pathways and physiological attributes, however, reactive oxygen species produced by excess accumulation of iron causes severe organ damages which ultimately leads to death. Hemochromatosis, also known as iron overload disease, is a metabolic syndrome where patients do not have control of regulating iron concentration in the body. This metabolic syndrome can be largely categorized into two: acquired hemochromatosis and hereditary hemochromatosis. Acquired hemochromatosis is a non-genetic condition of iron overload, where most patients develop symptoms after blood transfusion, which are results of several hem-associated diseases such as sickle-cell disease. On the other hand, hereditary hemochromatosis (HH) is a genetic disorder where patients lack the expression of iron-

regulating genes such as *HFE,* which develops under-expression of proteins involved in iron uptake and regulation, ultimately induces iron over-accumulation in the body. In the United States, the number of patients with *HFE* defects was presumably calculated to 1/227 of total adult population. The most prevalent phenotype of HH is the abnormal uptake of dietary iron, and patients with HH often fail to strictly regulate daily diet, which ultimately develops into iron overload in the body. Iron uptake occurs in the duodenum of the gastric-intestinal tract (GI tract), and compared to healthy adults, where the GI absorbs less than 10 % of total dietary iron, HH patients have been reported to uptake over 90 % of total dietary iron. [46-51] Therefore, in order to alleviate symptoms or prohibits exacerbation of the disease, HH patients must be strictly regulated of their dietary habits, which is an extremely difficult life-long process.
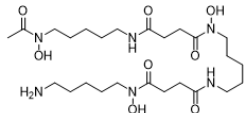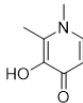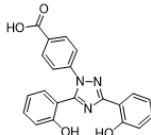
1.6 Current Therapeutic Advances and Limitations

Typical treatment for iron overload diseases is the use of synthetic iron chelators. Iron chelators are small molecule compounds that have functional groups to interact with and chelate free Fe (II) or Fe (III) iron to remove the iron from body. Currently, there are three FDA-approved iron chelators: Deferoxamine (DFO), Deferiprone (DFP), and Deferasirox (DFX). Among the three chelators, DFO has been the most widely prescribed chelator, which has three hydroxamic acid moieties that contribute to the binding of ferric iron Fe (III) with significantly greater affinity and specificity than other metal ions. DFO works by removing iron from the protein ferritin, an iron-storing protein, and DFO also inhibits iron uptake in many different cells. When the chelator binds to ferric iron with a 1:1 molar ratio, the complex shows a very high stability (log $K=10^{31}$), thus inhibiting access to other metals or oxygen (Table 2). [52, 53] The other two chelators DFP

and DFX are orally administered chelators, however, their poor efficacy and severe toxicity specifically associated with renal clearance have limited their clinical usage. In contrast, DFO has been known to exhibit the best efficacy with lease toxicity issues. However, one of DFO's limitations is its lack of administration routes, which is limited to only intravenous (IV) injection. Moreover, patients should take DFO through IV for at least 8 – 10 hours a day, 5 days a week, which also has been considered as a critical limitation in using DFO (**Table 1.2**). [48, 50, 54]

Table 1.2. Clinically Available Iron Chelators

Chelators	Route	$t^{1/2}$ (hr)	Advantage	Limitation	Structure
Deferoxamine (DFO)	IV, subQ (8-10hrs/day)	0.5	**Reversible toxicity Affordable Good efficacy**	**Administration route Poor bioavailability toxicity**	
Deferiprone (DFP)	Oral, TID	2-3	Oral	Poor efficacy toxicity	
Deferasirox (DFX)	Oral, QD	12-16	Oral	Expensive Severe toxicity	

Despite the presence of these iron chelators, treatment of HH still remains as an unmet need since the chelators are used for acquired hemochromatosis, but not for HH. Therefore, the need for developing alternative treatment for HH has surged over the past decade, and studies have been focusing on discovering a more effective delivery system for iron chelators.

As a result of the inconvenient administration routes and poor pharmacokinetic profiles of DFO, the drug has been reported to induce pain, infection, allergies, and adverse effects at the

administration site [55]. Moreover, it has also been reported that DFO may show toxicity issues in a long-term clinical application [56]. In particular, the terminal amino group of DFO has been identified to induce toxicities, and blocking the terminal significantly improved the toxicity file [57]. Therefore, there have been attempts to employ polymeric nanocarriers conjugated with DFO to address these issues. Nanocarriers conjugated with multifunctional polymers or moieties have been used to enhance the chelating efficacy of DFO and the detection of ferric iron. Our group has published an article regarding self-assembled micelles composed of Pluronics F127 polymer conjugated with DFO and tetraphenylethene (TPE) [58]. This DFO-F127-TPE (DFO-TFM, where T stands for TPE, F for F127, and M for micelle) generates a fluorescence quenching detection system of ferric iron since the absorption of DFO: Fe (III) complex overlaps with the fluorescence of TPE. Without the binding of ferric iron, the emission was 440nm, however, the intensity of emission decreased dose-dependently and was eliminated after chelating iron. Through quenching fluorescence, the complex can work as a method to monitor the chelation process in an iron overload model. Also, in vitro studies demonstrated that this DFO-TFM complex reduced cytotoxicity and improved the chelating efficacy of DFO.

Another article published by our group has implemented ROS-responsive thioketal polymer in fabricating pentafluorophenyl acrylate (PFPA) nano-gel conjugated with DFO, and upon a high concentration of ROS produced by excessive iron overload, the NG-DFO complex degraded to fragments and slowly released DFO [59]. This allowed the controlled release of DFO, which improved the circulating time and chelating efficacy of DFO. The size of the NG-DFO was 150 nm, and it was confirmed that by incubating NG-DFO with $100\mu M$ H_2O_2 for up to 24hrs, there was apparent size reduction, which indicated that thioketal linkage was cleaved and the nanocarrier

was successfully degraded. Subsequent in vitro ferritin reduction assays also confirmed that the NG-DFO complex showed significantly enhanced chelating ability compared to free DFO in iron overloaded (IO) J774A.1 cells. The same results were confirmed with in vivo studies using IO Balb/C mice. were significantly increased total iron excretion in urine and feces compared to free DFO treatment. IO mice treated with NG-DFO showed significantly increased total fecal and urine iron elimination compared to free DFO treated groups. Additional analysis of iron concentration in organs such as the liver, spleen, and kidney also indicated that NG-DFO treatment considerably reduced iron accumulation in these organs compared to free DFO.

In addition, our group utilized an enzymatically degradable nanocarrier to improve circulating time and efficacy and to reduce the cytotoxicity of DFO [60]. Poly(ethylene glycol) bis(amine) (PEG-BA) was threaded with a-cyclodextrin to form poly-rotaxanes (PR) which was conjugated with DFO and capped with Z-L-phenylalanine that is enzymatically degradable by proteases. Capping of PR dedicated to prolonged circulation time of the PR-DFO complex, which indeed enhanced chelating efficacy. Like other diseases, the iron overload condition causes severe inflammation and triggers the production of proteases such as B, L, and H [61]. Due to elevated levels of proteases especially in macrophages, which store iron, capping allows the complex more rapid endocytosis by macrophages, and after chelating iron, it also enables safe degradation and elimination of the complex. Significantly reduced cytotoxicity and enhanced efficacy were confirmed through both in vitro and in vivo studies.

Despite such effort in delivering DFO efficiently, most of these technologies are not suitable for treating HH since they are administered intravenously, and considering HH patients are not able

to regulate dietary iron absorption, all of the aforementioned methods fail to meet the unmet need of an alternative method in treating HH associated syndromes.

1.7 Study Design: A Prophylactic Treatment

Treatment of HH includes preventative measures such as phlebotomy and asking HH patients to minimize dietary iron intake. Moreover, iron chelators are not effective in treating HH since they are not capable of regulating the uptake of dietary iron. To address this unmet need, we designed prophylactic orally non-absorbable nanogel-deferoxamine (NG-DFO) conjugates to reduce excessive gut uptake of dietary iron. This study aimed to develop different sizes of NG-DFO conjugates and to evaluate their overall long-term safety and effectiveness at reducing dietary iron absorption in mice fed an iron-overload diet.

Nanogel as a nanocarrier was synthesized through reverse-phase free radical polymerization in water-in-oil emulsions and the resulting scaffolds were subsequently conjugated with the iron chelator Deferoxamine (DFO) to form NG-DFO of various sizes. Physicochemical properties of NG-DFO were evaluated using dynamic light scattering (DLS) and UV-vis absorption. Cellular permeability and endocytosis studies were conducted using NG-DFO-Cypate 5.5 (Cy5.5-NG-DFO) on Caco-2 cells grown in transwells as a monolayer to model gut enterocytes. In addition, in vitro digestive stability and cellular toxicity studies in Caco-2 cells were also conducted. Subsequently, biodistribution of Cy5.5-NG-DFO was evaluated in fasted Balb/C mice using IVIS imaging for up to 24 h. For the prophylactic efficacy study, mice were administered NG-DFO conjugates (50 mg equivalent of DFO/day) through oral gavage and fed

iron-overload (20,000ppm) diet ad libitum over 20 days, and serum ferritin, serum iron, and liver iron levels were evaluated. Long term GI toxicity due to increased iron uptake in the absence and presence of NG-DFO can be indirectly correlated to iron-associated liver damage, which was evaluated through liver histopathology analysis and ALT/AST functional assays.

Through these studies, we proposed to develop prophylactic NG-DFO conjugates, as a potentially useful treatment for HH, which are able to retain in the GI tract for reducing dietary absorption and iron-engaged organ toxicities as well.

CHAPTER 2

ANTIBACTERIAL AND BIOFILM ERADICATING ACTIVITIES OF PH-RESPONSIVE

VESICLES AGAINST PSEUDOMONAS AERUGINOSA [1]

_____

2.1 Abstract

The formation of biofilm by a microcolony of bacteria is a significant burden in the healthcare industry due to difficulty eradicating it. In this study, pH-responsive vesicles capable of releasing apramycin (APR), a model aminoglycoside antibiotic, in response to the low pH typical of established *P. aeruginosa* biofilms resulted in improved eradication of existing biofilms in comparison to the free drug. The amphiphilic polymeric vesicle (PV) comprised of block-polymer poly (ethylene glycol)-block-poly (2- (dimethylamino) ethyl methacrylate (mPEG-*b*-pDEAEMA) has an average size of 128 nm. The drug encapsulation content of APR in PV/APR was confirmed to be 28.2 % and the drug encapsulation efficiency was confirmed to be 51.2 %. At pH 5.5, PV/APR released >90% of APR after 24 h compared to <20% at pH 7.4. At pH 5.5, protonation of the pDEAEMA block results in a zeta potential of +23 mV compared to a neutral zeta potential of +2.2 mV at pH 7.4. Confocal microscopy, flow cytometry and scanning electron microscopy reveal that the positively charged vesicles can compromise the integrity of planktonic bacterial membrane in a pH-dependent manner. In addition, PV/APR is able to diffuse into mature biofilms to release APR in the acidic milieu of biofilm bacteria and PV/APR was more efficient at eliminating preexisting biofilms compared to free APR at 128 and 256 µg/mL. This study reveals that dynamic charge density in response to pH can lead to differential levels of interactions with biofilm and bacterial membrane. This effectively results in enhanced antibacterial and antibiofilm properties against both planktonic and difficult-to-treat biofilm bacteria at concentrations significantly lower than those of the free drug. Overall, this pH-responsive vehicle could be especially promising for treating biofilm associated infectious diseases.

2.2 Introduction

The formation of biofilm by a microcolony of bacteria is a significant burden in the healthcare industry due to its link to antibiotic resistance and death rate [34]. Although physical removal and high-drug dosage interventions are somewhat effective at combating biofilms, these methods often do not fully eradicate the biofilm and remaining bacteria can develop antimicrobial resistance (AMR) to drugs, wherein 100 to 1000-fold more drugs are needed to kill biofilm bacteria compared to the same strain of planktonic bacteria [23]. Antibiotics such as beta-lactams and aminoglycosides exhibit bactericidal efficacy against planktonic gram-negative bacterial cells, but their effectiveness can be hindered by limited diffusion through the biofilm due to drug interactions with the biofilm's extracellular polymeric substances (EPS) and degradation by bacterial enzymes present. This often results in a sublethal concentration of drugs reaching biofilm bacteria and results in the selection of bacteria with tolerance and resistance to the drug [23, 32]. The global prevalence of AMR-associated fatality is expected to exceed 10 million by 2050 due to the challenge of bacteria biofilm formation [21, 30].

In the hospital setting, the use of catheters, which is a tube inserted into the bladder through the urethra to drain urine, is a major cause of hospital-acquired urinary tract infections (UTIs) and can serve as a major route of persistent bacterial infection and biofilm formation inside the urinary tract, bladder, and kidneys of patients [29, 62]. Although there have been attempts to compromise or inhibit biofilm formation using nanoparticle formulations in the treatment of these recurrent UTIs, most of these applications are more effective at inhibiting biofilm formation early on rather

than eradicating preexisting biofilms that may have already formed [33, 39, 63]. Currently, the majority of catheter associated UTIs are most effectively managed by removing the catheter rather than treating it with antibiotics which may lead to AMR in persistent biofilms. Among challenging gram-negative bacterial strains present in catheter associated UTIs, *Pseudomonas aeruginosa* (*P. aeruginosa*) is a ubiquitous pathogen that is present in many infections ranging from the lungs in cystic fibrosis to chronic wounds to implant infections, and UTIs [64, 65]. Once established, this pathogen is difficult to eliminate due to its propensity to develop efflux pumps and enzymes conferring resistance to antibiotics such as beta-lactams and aminoglycosides [66] and its propensity to rapidly grow a biofilm that can lead to antibiotic resistance [26, 67].

Polymeric nanoparticles are a promising tool for delivering antibiotics and improving the treatment of bacterial infections [14, 68, 69]. Some of these nanoparticles can be readily designed to bear functional building blocks that are responsive to stimuli such as enzyme, pH, reactive oxygen species (ROS) and toxins in response to their surrounding environments [68, 70, 71]. Although demonstrated to be effective at killing planktonic bacteria and preventing biofilm development, few of these reports have demonstrated the capability to eradicate mature biofilms produced by *P. aeruginosa* [72-74]. One notable feature of *P. aeruginosa* biofilm is the development of a pH gradient when nutrients become depleted near the bacteria, a result of bacterial metabolism and the production of subsequent acidic byproducts such as lactic and acetic acids [75, 76]. This unique aspect of the biofilm environment means that pH-responsiveness is ideal to incorporate into the design of polymeric nanoparticles to facilitate their diffusion through the biofilm and triggering antibacterial and anti-biofilm properties.

Herein, we designed and constructed pH-responsive polymeric vehicles (PV) comprised of self-assembled amphiphilic diblock copolymer poly (ethylene glycol)-block-poly (2-(dimethylamino) ethyl methacrylate (mPEG-b-pDEAEMA). This nanoparticle is neutral at physiologic pH, thus facilitating its diffusion through the biofilm, and is designed to respond to the lower pH condition of the biofilm to release encapsulated antibiotics once the inner block transitions from hydrophobic to hydrophilic while acquiring a positive charge. The PEG block of PV prevents non-specific absorption and adhesion to EPS components [43, 44] for improved penetration into the biofilm and the pDEAEMA block is responsible for low pH-stimulated drug release and cationic interactions with the bacterial membrane. The cationic interactions are due to the tertiary amine of pDEAEMA protonating to a quaternary amine at low pH, which increases the hydrophilic nature of the block. This hydrophobic to hydrophilic transition of the inner block allows for swelling and morphological transformation of the vesicle, resulting in drug release at low pH in the vicinity of bacteria, and the positive charge generated simultaneously enhances adhesion to the bacterial membrane through electrostatic interactions (**Table 2.1**) [45, 77].

More specifically, the amphiphilic diblock copolymer mPEG-b-pDEAEMA was prepared via reversible addition-fragmentation chain transfer (RAFT) of the hydrophilic mPEG$_{2K}$-CTA as the initiator and hydrophobic 2- (dimethylamino) ethyl methacrylate (DEAEMA), followed by the formation of the amphiphilic vesicle through self-assembly. The mPEG$_{2k}$ length in conjunction with the length of the pDEAEMA block were specifically chosen here, as previously reported and characterized [78], to avoid micelle formation since amphiphilic vesicles are needed to effectively encapsulate aminoglycosides. The aminoglycoside chosen for encapsulation was apramycin (APR) since it is hydrophilic and reported to be effective against *P. aeruginosa* at a 90% minimum

inhibitory concentration (MIC) of 32 µg/mL [79]. The pH-responsive property of the vesicle was confirmed by measuring size (z-average diameter) through dynamic light scattering (DLS), bilayer structure of vesicles was confirmed through transmission electron microscopy (TEM), charge was measured through zeta potentials, and pH-responsive drug release was confirmed using APR as a model drug. The polymeric vesicle-encapsulated with APR (PV/APR) showed enhanced antimicrobial efficacy against *P. aeruginosa* due to the vesicle's ability to compromise bacterial membrane integrity and by internalizing into the bacteria to deliver a potentially larger payload of APR into the bacterial cell. Penetration studies using polymeric vesicles conjugated with the fluorophore Rhodamine B (PV-RhoB) inside established biofilms indicated that the vesicle was able to penetrate and diffuse through the complex biofilm structure. The biofilm eradication study confirmed that pH-responsive PV/APR readily penetrated through the biofilm and the combination of the delivered APR and the pH-induced cationic interactions of the vesicles on bacterial membrane resulted in enhanced antibacterial and biofilm eradicating activities compared to free APR and empty PV. These pH-responsive PV may better be able to penetrate through biofilms of *P. aeruginosa* compared to the free drug to deliver greater concentrations of the drug and combined with the cationic-induced membrane interactions at low pH, may be especially beneficial for eradicating pre-existing biofilms.
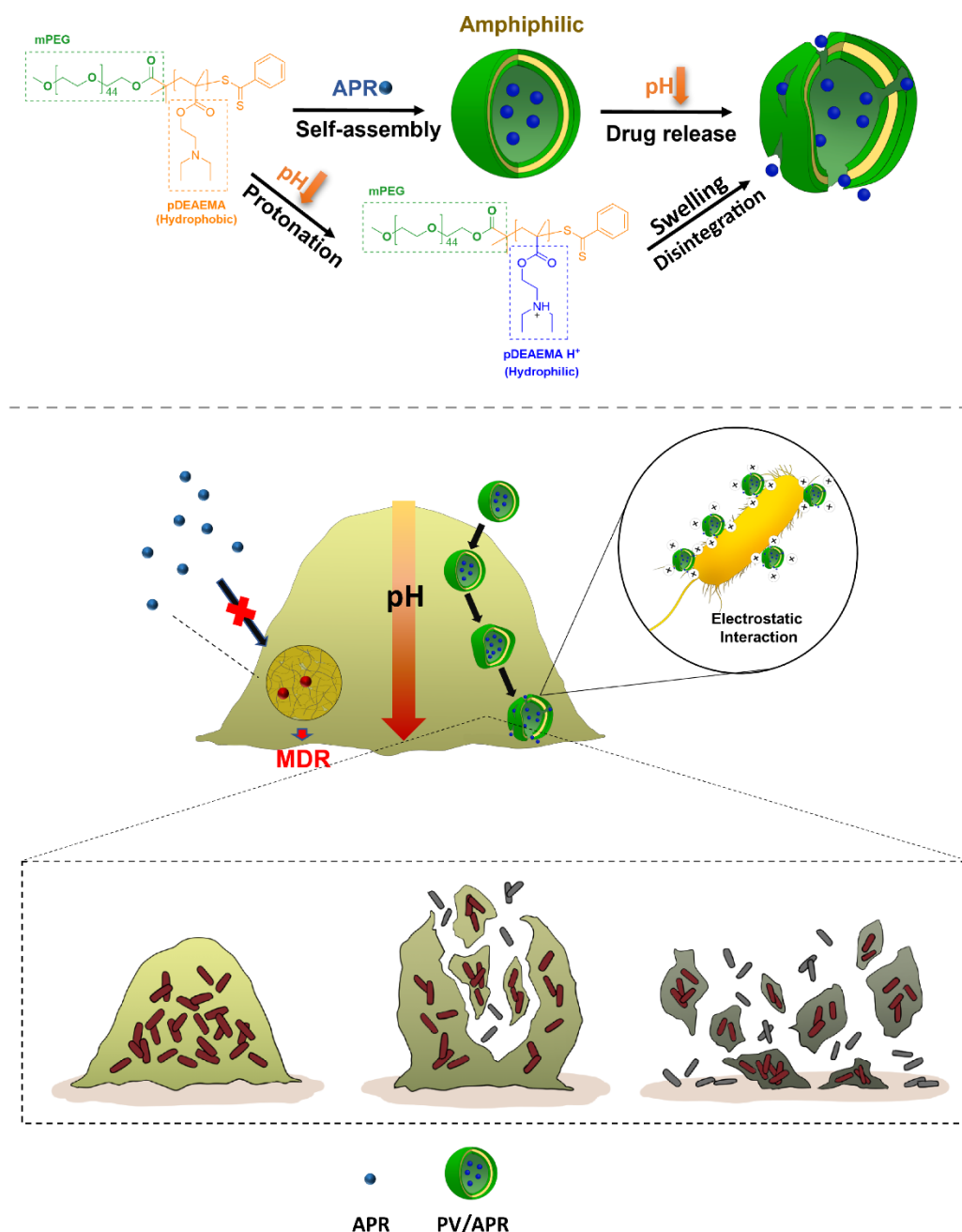
Table 2.1. Mechanism of PV Against Biofilm (A) Self-assembly and pH-responsive feature of amphiphilic mPEG-*b*-pDEAEMA vesicle (PV) results in release of APR in the *P. aeruginosa* biofilm. As the pH decreases, the hydrophobic pDEAEMA block protonates and becomes hydrophilic, destabilizing PV and releasing APR. (B) A pH gradient exists in the biofilm when

nutrients become depleted near bacteria. Neutral PV can penetrate into the biofilm and becomes positively charged as the pH decreases, resulting in electrostatic interactions between vesicle and biofilm bacteria, and leads to enhanced antibacterial and anti-biofilm properties.

2.3 Experimental

2.3.1 Preparation and physicochemical characterization of mPEG-*b*-pDEAEMA (PV) and fluorescent mPEG-*b*-p(DEAEMA-RhoB) (PV-RhoB)

The detailed synthesis of block polymer poly (ethylene glycol) poly (2-(Diethylamino) ethyl methacrylate) (mPEG-*b*-pDEAEMA) and fluorescent poly (ethylene glycol) poly (2-(Diethylamino) ethyl methacrylate–Rhodamine B) (mPEG-*b*-p(DEAEMA-RhoB) are summarized in **Table S2.1-S2.2**. The preparation of mPEG-*b*-pDEAEMA or mPEG-*b*-p(DEAEMA-RhoB) vesicles was conducted through the solvent evaporation method. Briefly, 40 mg of the mPEG-*b*-pDEAEMA or mPEG-*b*-p(DEAEMA-RhoB) block polymers were dissolved in 3 mL of tetrahydrofuran (THF), and the solution was slowly added dropwise to 10 mL of 5 mM pH 7.4 phosphate buffer (PB), while stirring at room temperature for 24 hours. The solution was then evaporated and filtered through syringe filters (d = 0.45 µm) to yield the desired nanovesicles at a concentration of 4.0 mg/mL in pH 7.4 PB buffer. The average hydrodynamic size distribution, polydispersity (PDI), and Zeta (ζ) potential of the vesicles was monitored and characterized using dynamic light scattering (DLS, Malvern Nano-ZS). The morphology of the vesicles was observed through transmission electron microscope (TEM, JEOL-JEM1011) with tungstate negative staining.

The pH-responsive property of mPEG-*b*-pDEAEMA vesicles was characterized by measuring zeta-potential as a function of pH and the z-average size distribution was measured by DLS after incubating the vesicles in different pH buffers. Briefly, buffers with pH ranging from 3 to 8 were prepared using either acetates or phosphates, and the vesicles were incubated in each buffer at 1:1 volume ratio for 24 hours followed by measurements of the zeta-potential and size in corresponding pH buffers. The fluorescent property of mPEG-*b*-p(DEAEMA-RhoB) was verified by fluorescence spectrometry. Briefly, the mPEG-*b*-p(DEAEMA-RhoB) vesicles in different pH buffers as described above were excited at 560 nm and the corresponding emission spectrum was monitored.

2.3.2 APR encapsulation, characterization, and release properties of PV/APR

To prepare drug-encapsulated vesicles, 40 mg of the block polymer mPEG-*b*-pDEAEMA in 4 mL of THF was slowly added dropwise to pH 5.5 PB buffer containing 80 mg of APR, followed by slowly increasing the pH to 7.4 using 1N NaOH and stirring for 48 hours at room temperature. After the encapsulation, unencapsulated free APR was removed through dialysis (3.5 kDa MWCO) in pH 7.4 aqueous solution for 72 hours. The drug encapsulation efficiency (DEE) was indirectly determined based on a calibration curve generated from free APR and 2,4,6-trinitrobenzene sulfonic acid (TNBS). This previously reported method allows for quantitative amine detection based on drug-TNBS interactions and the generation of a calibration curve based on concentration-dependent absorbance at 334 nm [80]. Briefly, 0.5 mL from each 2-fold serial dilution solutions starting with 50 µg/mL concentration of free APR dissolved in 0.1 M sodium bicarbonate buffer was added with 0.5 mL of the 0.01 % (w/v) solution of TNBS in the same

buffer, followed by thorough mixing, and incubation at 37°C for two hours. Each resulted solution

was then measured at 335 nm using UV-vis spectrometer to generate a linear relationship between

free APR concentration and absorbance values. The drug-encapsulation content (DEC) and DEE

of PV/APR were calculated using Equations 1 and 2:

$$DEC(wt\%) = \frac{weight\ of\ encapsulated\ drug}{weight\ of\ encapsulated\ drug\ and\ polymer} \times 100 \qquad \text{(Equation 1)}$$

$$DEE(wt\%) = \frac{weight\ of\ encapsulated\ drug}{weight\ of\ drug\ in\ feed} \times 100 \qquad \text{(Equation 2)}$$

APR release from the pH-responsive vesicles was conducted by incubation in pH 6, 5, and

4 buffer solutions. Briefly, PV/APR suspensions (1 mL for each pH condition) were transferred

into narrow dialysis tubing (3.5 kDa MWCO) and placed into 50 mL centrifuge tubes containing

15 mL of each individual pH buffers as release media to mimic the sink conditions for incubation

at 37 °C for 24 hours. At various time points, 1 mL of media outside the dialysis tubing was

collected and 1 mL of fresh buffer of each different pH was added to the centrifuge tubes to

maintain a total of 15 mL release media. The collected media was then lyophilized and its

absorbance at 335 nm was measured using the TNBS method previously described.

2.3.3 MIC, MBC, and drug resistance studies

The MIC studies of free APR, PV/APR and blank PV were conducted against wild type *P.*

aeruginosa (PAO1) through the serial dilution method, in which the MIC here is defined as the

lowest concentration of the drug capable of preventing the visible growth of a microorganism after overnight incubation in LB media. Briefly, a series of 2-fold dilution of either free APR or equivalent PV/APR in 135 µL aliquot of the LB medium was added and mixed with 15 µL aliquot of each bacterial solution (OD600 = 0.001) in LB in a 96-well plate and incubated in a shaker at 37 °C for 24 hours. Then, the absorption of the suspension (A_s) in each well at 600 nm (OD600) was measured using a microplate reader (Spectramax® Plus 384 Microplate Reader). Wells with only medium was used as the27egateve control (A_N) and bacteria grown in the media without treatment was used as the positive control (A_p). For MIC studies conducted at pH 5.5 against PAO1, the pH of LB medium was adjusted to pH 5.5 using 1N HCl during the incubation period.

The minimum bactericidal concentration (MBC) of visible bacterial growth in the presence of free APR or PV/APR at pH 7.4 or pH 5.5 buffer solution against PAO1 was determined via similar method to that of the MIC study. In brief, 2-fold serial dilutions of the agents in different pH buffers were added into aliquot of PAO1 in the same pH buffer at an initial OD600 value of 0.1 in 96-well plates. After incubating at 37 °C for 24 hours, OD600 value (A_s) of each well was measured. The relative growth of bacteria in this study was calculated using Equation 3.

$$Relative\ growth = \frac{A_S - A_N}{A_P - A_N} \qquad \text{(Equation 3)}$$

After determining the MBC, the bactericidal efficacy of free APR versus PV/APR was monitored more closely to better assess time-dependent differences between the formulations. As before, in 96-well plates, agents at fixed drug concentrations in either pH 7.4 or pH 5.5 buffer were

added to PAO1 in buffer (initial OD600 = 0.1) and the plates were incubated for 6 hours. At various time points, the absorption from each well was measured and relative growth was monitored.

To investigate the drug resistance susceptibility of PAO1 in the presence of free APR or PV/APR, bacteria in pH 7.4 or pH 5.5 LB medium with initial OD value of 0.1 bacteria was treated at the MBC of PV/APR (determined to be 256 µg/mL equivalent APR) for up to 8 hours. At each time point, the bacterial growth was measured via absorption at OD600. All studies were conducted in quadruplicates, wherein the error bars represent the standard deviation of the mean values measured from four independent experiments.

2.3.4 Probing the pH-dependent behavior of vesicles against PAO1

To probe the nature of the electrostatic interactions between PV with the bacterial membrane at pH 7.4 and pH 5.5, confocal microscopy and flow cytometry studies were conducted. PAO1 was inoculated and grown at 37 °C for 24 hours. After incubation, 1 mL of bacteria from the growth medium was added to different microcentrifugation tubes and the medium was removed by centrifugation (12,000 rpm, 10 min). Each individual tube was then washed with pH 7.4 buffer or pH 5.5 buffer solutions and centrifuged again three times, followed by dilution with each buffer to a final OD600 0.5. To the tubes containing bacteria in corresponding pH buffers, 0.2 mg/mL of the fluorescent PV-RhoB was incubated for 2 hours at 37 °C. After incubation, buffers were removed, and the tubes were washed with buffers to completely remove remaining compounds. The bacterial cells in the tubes were labeled with green-fluorescent membrane marker FM^{TM} 1-43FX (Invitrogen^{TM}), fixed, and membrane interactions were assessed by confocal microscopy

(LSM710 Confocal Microscope and ELYRA S1 Super Resolution Microscope, Carl Zeiss) and flow cytometry studies (CytoFLEX, Beckman Coulter).

To further visualize the morphological bacterial membrane effect of the interaction between PV and the bacteria, PAO1 incubated with PV at different pH were collected through centrifugation, fixed with 4% glutaraldehyde for 4 hours, then washed and dehydrated with water and ethanol through serial dilution. The resulting morphology of the bacteria was assessed using scanning electron microscopy (SEM, FEI Quanta 200, The Netherlands) with an acceleration voltage of 20 kV.

To investigate the outer membrane (OM) permeability of PAO1 in the presence of PV at different pH, the nitrocefin (NCF) assay was utilized. Briefly, PAO1 bacterial cells in stationary states were collected, suspended into 10 mM PBS (OD600 = 0.05) in 96-well microplates, and incubated with 0.2 mM NCF and 200 µg/mL of PV at 37 °C for 3 hours. When the bacteria membrane is permeabilized, NCF can enter the bacteria and undergoes hydrolysis catalyzed by bacterial enzymes. This hydrolysis of NCF can be monitored at OD486 as a function of time, as previously reported [16, 68]. Studies were carried out in triplicate.

2.3.5 Biofilm penetration studies

To probe the biofilm penetration behavior of PV, confocal microscopy studies were conducted on PAO1 biofilm established following the method reported by Fulaz et al [76]. Briefly, a 10 mL volume of PAO1 with initial OD600 1.0 in LB medium was added to a sterile 50 mL

centrifuge tube containing a glass coverslip (Globe Scientific, 24 × 50 mm), followed by gentle agitation on a shaker at 37 °C for 72 hours. After confirming that the biofilm was successfully grown on the coverslip, the coverslips were removed, washed with DPBS, and placed into a new 50 mL of centrifuge tube containing 10 mL of DPBS diluted with SYTO^{TM}-13 Green Fluorescent Nucleic Acid Stain and incubated for 20 min at room temperature. After staining, the coverslips were washed with DPBS, placed, and fixed on the slide for imaging using Zeiss 710 confocal laser scanning microscope with a 40x objective oil lens.

To verify that the inner pH of established biofilm is acidic, a pH sensitive fluorophore Fluorescein isothiocyanate (FITC, fluoresce max at 520 nm) was incubated with the biofilm, followed by analysis using confocal microscopy. Briefly, since FITC was reported to show decreased fluorescence intensity [81], we first conducted an *in vitro* evaluation of FITC in different pH buffers. Same concentration of FITC was incubated in pH 7.4, 6.0, 5.5, 4.0, and 3.0 buffers for 30 min, and the fluorescence spectrum was analyzed using SpectraMax Gemini (**Figure S2.8**). After confirming the pH sensitive property, FITC was incubated with the biofilm for 12 h, followed by staining with FM^{TM} 4-64 membrane stain, and the biofilm was analyzed using 3D imaging by confocal microscopy.

After confirming that the biofilms were well established, the biofilms were treated with fluorescent PV-RhoB and the control micelle DEX-PLGA-Cy 7.5. The synthesis of DEX-PLGA-Cy 7.5 is summarized in the supporting information (**Table S2.3**). Biofilms grown on the cover glass for 3 days were co-incubated with 0.2 mg/mL PEG-*b*-p(DEAEMA)-RhoB vesicles for 2 h, followed by incubation with 0.2 mg/mL DEX-PLGA-Cy 7.5 for 2 h in 15 mL of DPBS in a 50 mL

centrifuge tube at 37 °C for 2 hours, followed by washing, staining with syto-13, and fixed on slides prior to 3D-confocal laser scanning microscopy (3D-CLSM, LSM710 confocal microscope model) imaging with 40x objective oil lens.

2.3.6 Biofilm eradication studies

The preparation of established 3-days old *PAO1* biofilms was conducted as described above. Next, APR at 2, 4, and 8-fold the MIC for the free drug or equivalent PV/APR was added to each 50 mL of tube containing glass slides with full grown biofilms in DPBS. The tubes were incubated on a shaker at 37 °C for 24 hours. Glass slides were carefully removed, washed with DPBS three times, and stained with syto-13 fluorescent nucleic acid stain (green) and propidium iodide (red) to detect live and dead bacterial cells through CLSM. Analysis of the biofilm eradication efficacy was analyzed with 3D-CLSM through rendered imaging of biofilms. More specifically, 488 and 568 nm lasers with 40x objective oil lens were used to provide z-stack of multi-channel and illumination images to determine the depth of biofilms and live/dead bacterial composition after treatments.

2.4 Results and discussion

2.4.1 Synthesis and physicochemical characterization of the block polymer

The syntheses of pH-responsive mPEG-*b*-pDEAEMA or fluorescent mPEG-*b*-p(DEAEMA-RhoB) polymers were conducted as described in the supporting information (**Table S2.1 and**

S2.2). The physicochemical characterizations of mPEG-*b*-pDEAEMA are summarized in **Table 2.1**. The block polymer was synthesized through RAFT polymerization of mPEG$_{2K}$-CTA as the initiator and 2-(diethylamino) ethyl methacrylate (DEAEMA) as the pH-responsive monomer (**Scheme S2**). Based on NMR estimates and GPC analysis, the molecular weight of the synthesized amphiphilic mPEG-*b*-pDEAEMA block polymer ranged approximately between 16.9 kDa and 17.1 kDa (**Table 2.1**), with approximately 1:90 molar ratio of mPEG$_{2k}$ to hydrophilic pDEAEMA repeat units in order to form vesicles, as previously reported [78]. The DLS and TEM analysis confirmed that the polymer self-assembled into spherical amphiphilic vesicle with a z-average of 128 ± 1.2 nm for blank vesicles (PV) and 168 ± 0.83 nm for PV/APR (**Figures 2.1 A-C**). The synthesis of fluorescent mPEG-*b*-p(DEAEMA-RhoB) (PV-RhoB) used in confocal laser scanning microscopy (CLSM) and flow cytometry studies was prepared at 1:0.5 molar ratio of mPEG$_{2k}$ to fluorescent monomer RhoB, followed by self-assembly to form the amphiphilic vesicles as confirmed by TEM (**Figure 2.1D**). To verify the pH-responsive behavior of these vesicles, empty PV was incubated in different pH buffers and the zeta potential was measured. As the pH decreased, pDEAEMA transitioned from hydrophobic to hydrophilic due to protonation at the tertiary amine and was characterized by a maximum zeta potential of approximately +30 mV at pH 3.0; this was also accompanied by an increase in the transparency of the solution (**Figure 2.1E**). The drug encapsulation content (DEC) of APR in PV/APR was confirmed to be 28.2 % and the drug encapsulation efficiency (DEE) was confirmed to be 51.2 %. The pH-mediated protonation of pDEAEMA has been reported to induce swelling of vesicles formed from this material [45], which leads to instability of vesicles and was evidenced by increasing size and polydispersity of PV incubated at lower pH (**Figure 2.1F**). The pH-induced instability of the PV was also observed through TEM analysis. The PV incubated at pH 5.5 condition showed apparent swelling and disintegration as the arrows indicate (**Figure S2.4**). These

findings corroborate that drug release of APR from PV likely occurs during this destabilization phase at low pH wherein PV swells and undergoes unstable morphological transformations which leads to the pH-dependent release of APR (**Figure 2.1G**). At pH 7.4, cumulative APR released from the vesicle did not exceed 20% up to 24 hours of incubation whereas more than ca. 90% of APR released at pH 5.5.

Table 2.1. Physicochemical Characterizations of PV

Samples (pH)	Mn, NMR[a]	Mn, GPC[b]	ζ	D[c]	DEC[d]	DEE[e]	MIC (µg/mL)	MBC (µg/mL)
	kDa	kDa	mV	nm	(wt%)	(wt%)	PAO1	PAO1
mPEG2k-b-pDEAEMA	17.7	16.9	–	–	–	–	–	–
PV (7.4)	–	–	3.38±0.9	128±12	–	–	> 2000	> 2000
PV (5.5)	–	–	24.5±1.9	–	–	–	> 2000	> 2000
APR (7.4)	–	–	–	–	–	–	32	> 256
APR (5.5)	–	–	–	–	–	–	32	> 256
PV/APR (7.4)	–	–	2.19±0.6	168±0.83	28.2±3.3	51.2±6.8	64	> 256
PV/APR (5.5)	–	–	23.2±1.1	–	–	–	32	256

[a] Calculated from ^{1}H NMR, [b] Determined by GPC using polystyrene as standards, [c] D = diameter was determined by DLS. [d] Drug Encapsulation Content (DEC) defined as APR encapsulated [e] Drug Encapsulation Efficiency (DEE) defined as encapsulated APR / APR in feed (×100%). MIC refers to minimal inhibitory concentration for an initial OD600 0.1 at 24 h; MBC refers to minimal bactericidal concentration for an initial OD600 of 0.1 at 12 h.
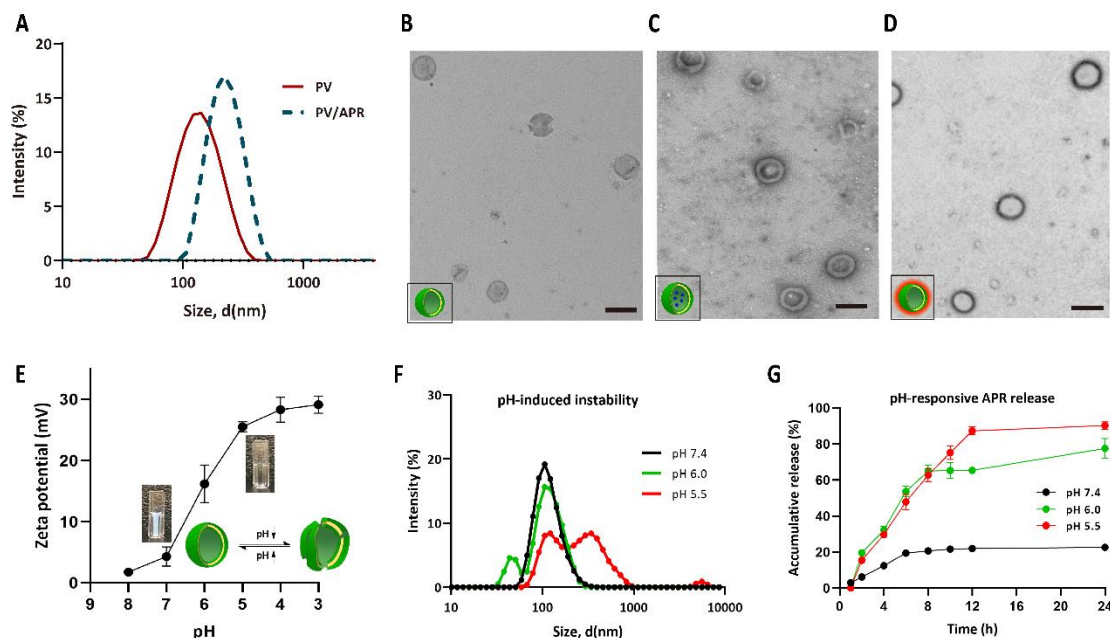
Figure 2.1. (A) Size of blank PV and PV/APR was evaluated by DLS. (B-D) Morphologies of blank PV, PV/APR and PV-RhoB as imaged by TEM reveals a bilayer vesicle structure. (E) Zeta potential of blank PV at different of pH; inset image also reveals a transition from a cloudy to a clear suspension as the zeta increases with decreasing pH, (F) Instability of PV as a function of pH based on size distribution (G) Cumulative release of APR from PV/APR at pH 7.4, 6.0, and 5.5 buffers after 24 hours.

2.4.2 MIC, antibiofilm, MBC, and drug resistance studies

Free APR displayed a MIC of 32 µg/mL and PV/APR was characterized by an MIC of 64 µg/mL in LB medium pH 7.4 (**Figure 2.2A),** confirming less antibiotic was freely available in the media due to <20 % drug release from PV/APR at this pH (**Figure 2.1G**). The MIC of PV/APR decreased 2-fold to 32 µg/mL in pH 5.5 LB medium, supporting that more drug released under

low pH and resulted in better antibacterial properties. As a control, at a concentration equivalent to that of PV/APR, blank PV exerted no antibacterial activity regardless of the pH (**Figure S2.3**).

The MBC of PV/APR at pH 5.5 was 256 µg/mL and bacteria remained >40% viable for all the other agents tested (**Figure 2.2B**). To investigate further the time-dependent differences at the MBC of PV/APR compared to free APR, drugs were incubated with PAO1 for 12 hours and bacterial viability was assessed at 0, 4, 8 and 12 h timepoints at pH 7.4 (**Figure 2.2C**) and pH 5.5 (**Figure 2.2D**). There was no viability difference between PV/APR and APR at pH 7.4 but at pH 5.5 PV/APR significantly decreased the bacterial viability an additional ca. 2-fold after >8 h incubation. At the corresponding polymer concentration of 256 µg/mL APR, blank PV had no effect on the viability of bacteria at either pH (**Figure S2.3**), suggesting that the combination of PV/APR has a pronounced effect on the bacteria at low pH but not at pH 7.4.
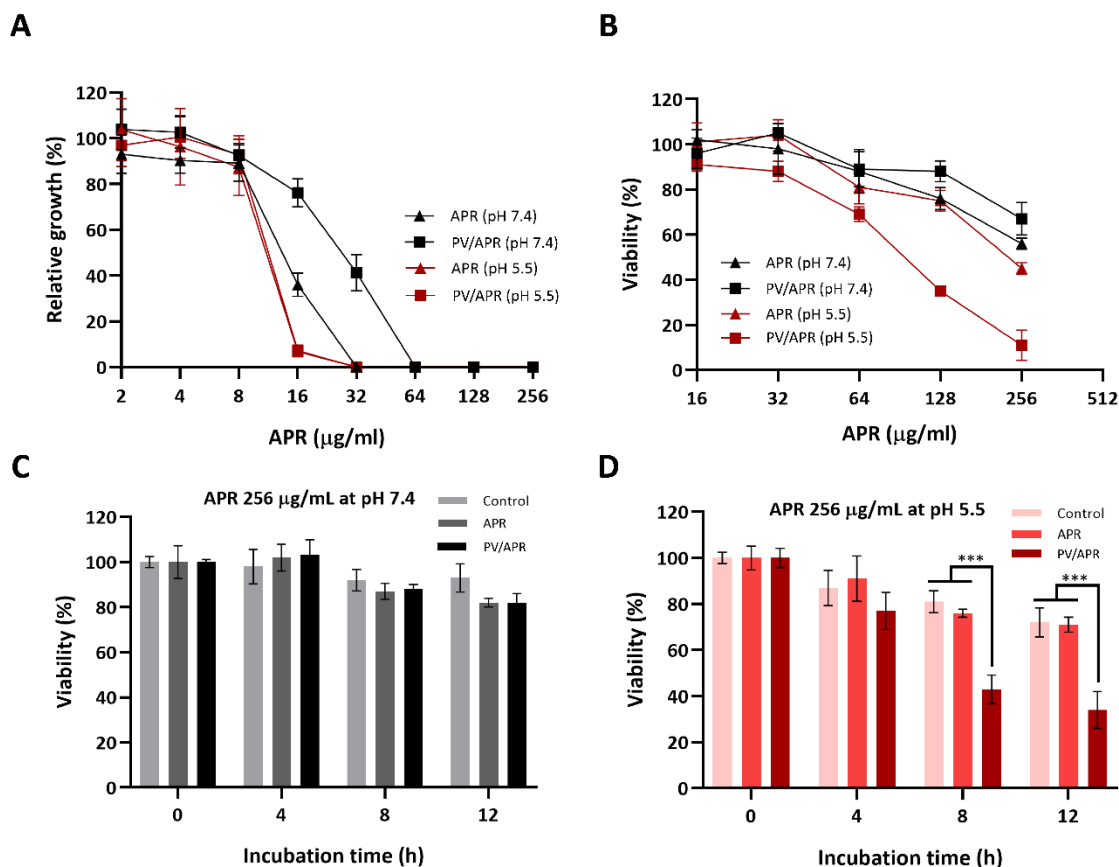
Figure 2.2. (A) MIC and (B) MBC curves for free APR and PV/APR in LB medium at pH 7.4 and pH 5.5 against PAO1. (C, D) Time-dependent bactericidal studies at the MBC of 256 µg/mL for PV/APR at pH 7.4 and pH 5.5.

For the time-dependent growth inhibition study conducted above at a concentration above the MIC of APR and PV/APR, bacteria was co-incubated with 256 µg/mL free APR or PV/APR in LB medium for 8 hrs. Results suggest susceptibility of bacteria to free APR after 2 hours in both pH 7.4 and 5.5 conditions whereas the PV/APR treatment resulted in prolonged inhibition of bacterial growth compared to the free drug, perhaps due to the sustained pH-responsive release of drug at pH 5.5 (**Figure 2.3**). As a control, blank PV showed slightly better growth rate inhibition of bacteria at pH 5.5 compared to pH 7.4 but was not as effective as PV/APR.
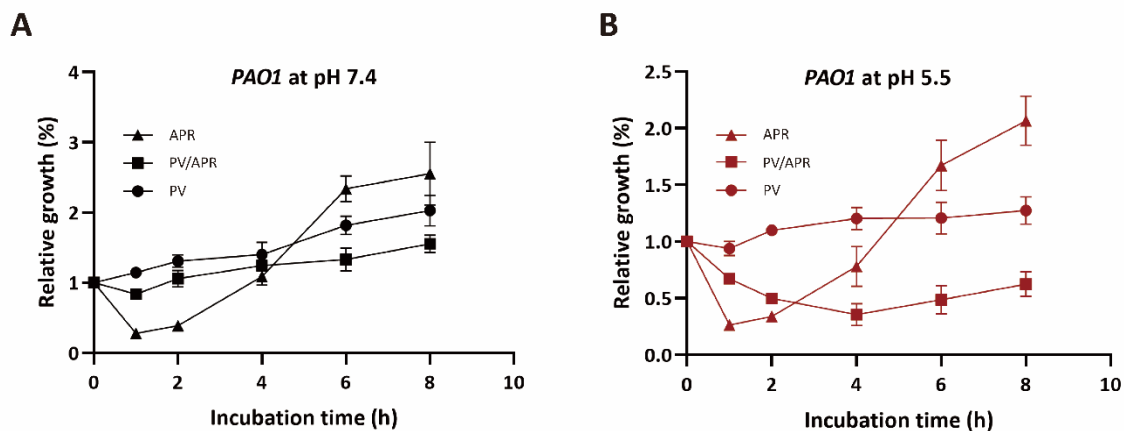
Figure 2.3. (A) Evaluation of bacterial susceptibility against APR at pH 7.4 and (B) pH 5.5 was conducted by monitoring the relative growth of bacteria in LB medium with pH 7.4 or 5.5 in the presence of 256 µg/ml equivalent drug of free APR or PV\APR over 8 hours. Drug susceptibility of the bacteria was confirmed against free APR within 2 h, while the susceptibility was prolonged with PV/APR after 2 h at pH 5.5. Study was carried out in triplicates.

2.4.3 Probing the pH-dependent behavior of nanovesicles against PAO1

PV/APR results in enhanced inhibitory and bactericidal activity against planktonic PAO1 at low pH (**Figure 2.2**) and improves inhibition of bacterial resistance compared to free APR or blank PV alone at pH 5.5 (**Figure 2.3**). Physical characterizations of PV at low pH demonstrate that the vesicle undergoes unstable morphological changes as the tertiary amines of pDEAEMA protonate and the block transitions from hydrophobic to hydrophilic. This destabilization may also result in the positively charged pDEAEMA block interacting more effectively via electrostatic interactions with the negatively charged bacterial membrane at low pH compared to pH 7.4. Indeed, positively charged antimicrobial nanoparticles can interact via electrostatic interactions, as previously reported for PAO1 [82, 83]. To probe the nature of this interaction, fluorescently

conjugated vesicles (PV-RhoB) were prepared and incubated with the bacteria at different pH for 2 hours prior to imaging with the confocal microscope. Compared to pH 7.4, there was visibly more localization of the vesicles with bacterial cells at pH 5.5 (**Figures 2.4A and S2.4**). This suggests that the positive charge due to protonation of the pDEAEMA block enhances localization of vesicles onto the bacterial cells via electrostatic interactions. To quantitate this observation, flow cytometric analysis indicated that only 33.9 % of cells interacted with PV-RhoB at pH 7.4 but this number drastically increased to 94.1 % at pH 5.5 (**Figure 2.4B**).
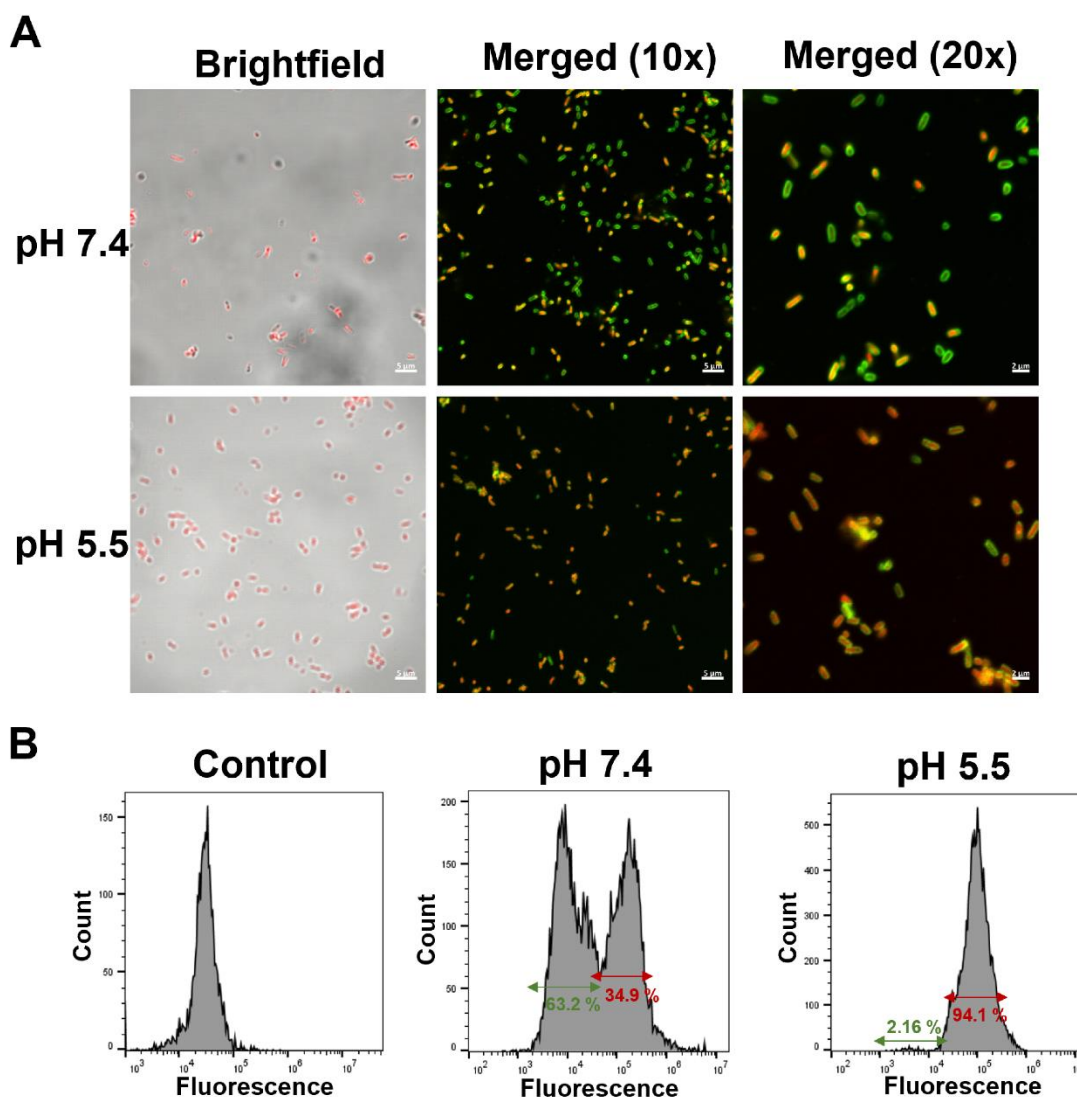
Figure 2.4. (A) Bacterial cells were co-incubated with 0.1 mg/mL fluorescent PV-RhoB for 2 h in pH 7.4 or 5.5 buffers. The green channel represents bacterial membrane stained with FM™ 1-43FX and the red channel represents the fluorescent PV (scale bars = 5 µm for 10x lens, 2 µm for 20x lens). (B) Quantitative flow cytometry reveals that 34.9 % bacterial cells interact with PV-RhoB at pH 7.4 and increases to 94.1% at pH 5.5.

To determine if electrostatic interactions between vesicles and bacteria lead to permeabilization of the OM, the NCF assay was utilized. The chromogenic β-lactam compound

NCF undergoes hydrolysis in the presence of β-lactamase enzymes typically located in the periplasm of the bacteria. An increase in hydrolysis of NCF is an indicative of increased membrane permeability and this change can be monitored by absorbance at 486 nm wherein the rate of hydrolysis is primarily limited by the rate of enzyme crossing the permeabilized OM and the integrity of the membrane [68]. PAO1 cells co-incubated with NCF in the presence of PV clearly revealed increased hydrolysis of NCF at lower pH (**Figure 2.5A**), indicating that the positively charged PV increases OM permeability. The effect of charged vesicles on bacterial OM morphology was visually assessed by SEM. PAO1 cells incubated with PV at pH 5.5 appeared more corrugated compared to bacteria treated with pH 5.5 buffer alone or PV at pH 7.4 (**Figure 2.5C**).

The confocal images of PV and the quantitative flow cytometry demonstrate that PV favorably co-localized with the bacteria at both pH 7.4 and 5.5 but accumulated more substantially at lower pH. To investigate further between the nature of this co-localization, super resolution imaging confocal microscopy was conducted was conducted on individual bacteria cells (Zeiss ELYRA S1 Super Resolution Microscope). Bacterial cells were incubated with 0.1 mg/mL of PV-RhoB in pH 7.4 or pH 5.5 buffers for 2 hours, and super resolution confocal images were taken. Compared to pH 7.4 images of individual bacteria wherein PV is mostly found associated with the OM, images reveal that the vesicle can penetrate into the bacteria at pH 5.5 (**Figure 2.5B**). In **Figure S2.5**, a horizontal cross section of each planktonic cell was analyzed, and the fluorescence intensity (Y-axis) across the length of a cross section of the bacteria (X-axis) was measured to visualize the internalization of PV into the bacteria cell. The data from bacteria from pH 5.5 shows that there is a significantly stronger intensity of PV-RhoB between the two membrane layers and suggests that PV-RhoB successfully penetrated the bacteria, whereas histogram of bacteria from

pH 7.4 showed no intensity for PV-RhoB between the membrane layers, confirming that at pH 7.4 PV is mostly found on the bacterial membrane. The penetration of PV/APR at low pH into the bacteria may result in more drugs being taken up by bacteria and explains why this combination enhanced the antibacterial activity observed compared to free APR (**Figure 2.2**) or blank PV alone (**Figure S2.3**).
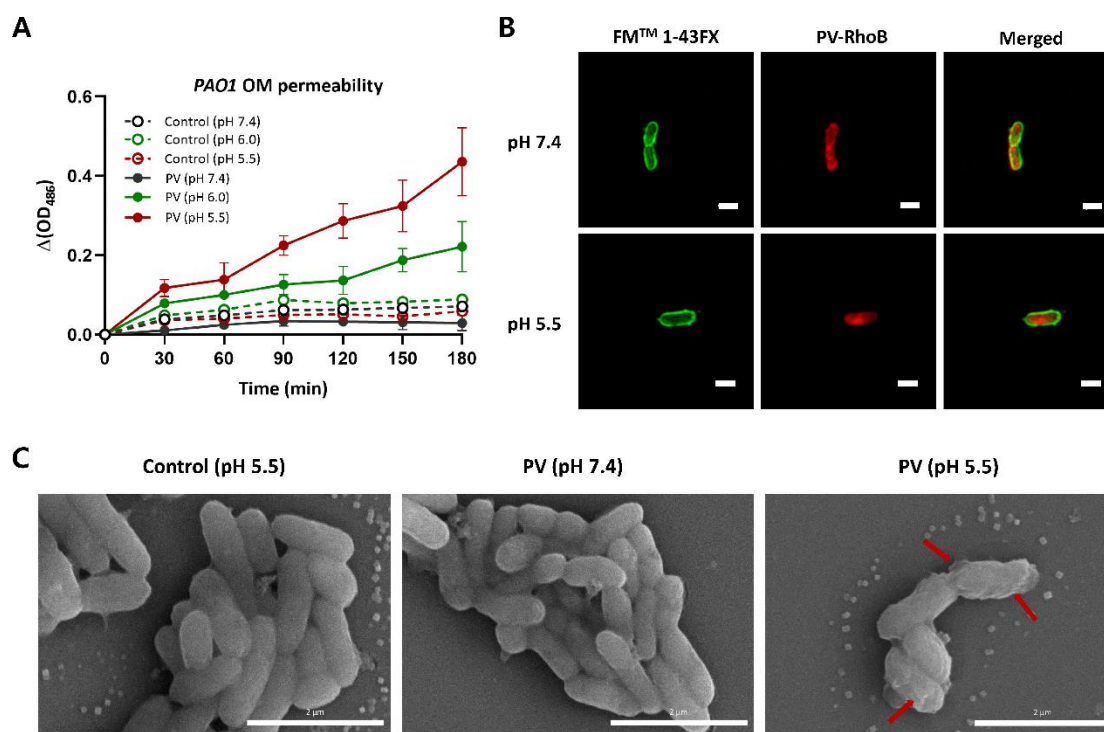
Figure 2.5. (A) OM permeability of PAO1 was enhanced in the presence of PV-RhoB as pH decreased. (B) Super resolution confocal microscopy images of PV-RhoB accumulation at the bacterial membrane at pH 7.4 in contrast to penetration into a PAO1 cell at pH 5.5 (scale bar = 1µm). (C) SEM images (scale bar = 2 µm) of PAO1 after incubating with 0.1 mg/mL blank PV in pH 7.4 and pH 5.5 buffer for 2 hours. Controls for pH 5.5 were carried out without any treatment. Arrows indicate compromised bacterial membrane.

2.4.4 Established biofilm penetration studies

The ability of a drug-encapsulated nanoparticle to successfully diffuse through the biofilm to nearby bacteria is a crucial factor to assess. The incorporation of a non-ionic hydrophilic PEG block in the design of PV is expected to minimize non-specific interactions of the vesicle with the EPS components of the biofilm and should facilitate penetration into the biofilm [43].

Before conducting penetration studies, we conducted a study using pH-sensitive fluorophore Fluorescein isothiocyanate (FITC) to verify that the inner microenvironment of established biofilm is acidic. Since FITC was reported to show decreased fluorescence intensity as pH decreases [81], we firstly incubated same concentrations of FITC in pH 7.4, pH 6.0, pH 5.5, pH 4.0, pH 3.0 buffers and analyzed the intensity of fluorescence to confirm the pH-sensitive property. The *in vitro* result showed apparent reduction in the fluorescence intensity upon decrease in pH, as shown in **Figure S2.8**. Then, a fully grown biofilm was incubated with FITC for 12 h, and the 3D confocal images showed that the fluorescence intensity decreased inside the biofilm (**Figure S2.9**). In detail, at the highest height of the biofilm (z = 18 µm), the intensity of FITC (green) was similar to that of FM^{TM} 4-64 (red, membrane stain), in the thickest area as indicated by the white arrow (**Figure S2.9A**). However, the intensity of FITC significantly decreased inside the biofilm (z = 10 to 2 µm), which was also indicated by the mean relative intensity (**Figure S2.9B**). This result showed that on the surface area of the biofilm where the pH is neutral, FITC was not affected, while as it goes deeper into the biofilm, FITC lost fluorescence due to acidic microenvironment of the biofilm.

Mature biofilms were prepared and incubated with PV-RhoB, and the biofilm was stained (green fluorophore) and analyzed by 3D-CLSM. Results confirm that PV-RhoB (red fluorescence) can successfully penetrate deep into a 3-days grown mature biofilm (**Figure 2.6**). In addition, to further strengthen the ability of PV in penetrating biofilms, a control DEX-PLGA micelle with size similar to PV (**Figure S2.10**) was conjugated with a fluorophore Cyanine 7.5 (Cy 7.5) and was incubated with the biofilm. For comparison, the same concentration of PV-RhoB and the control DEX-PLGA-Cy 7.5 were incubated for 2 h, and 3D confocal images were analyzed. The result showed that PV-RhoB (red) was evenly distributed over the biofilm, while the control DEX-PLGA-Cy 7.5 (purple) did not (**Figure S2.11**). The majority of the DEX-PLGA-Cy 7.5 remained on the surface area of the biofilm, suggesting a possible explanation that the poor penetration profile is likely due to degradation by microbial enzymes existing inside the biofilm such as dextranhydrolases [84]. As a result, PV showed significantly greater penetration profile compared to that of the control polymer, further enhancing the importance of PEG backbone in the design of PV.
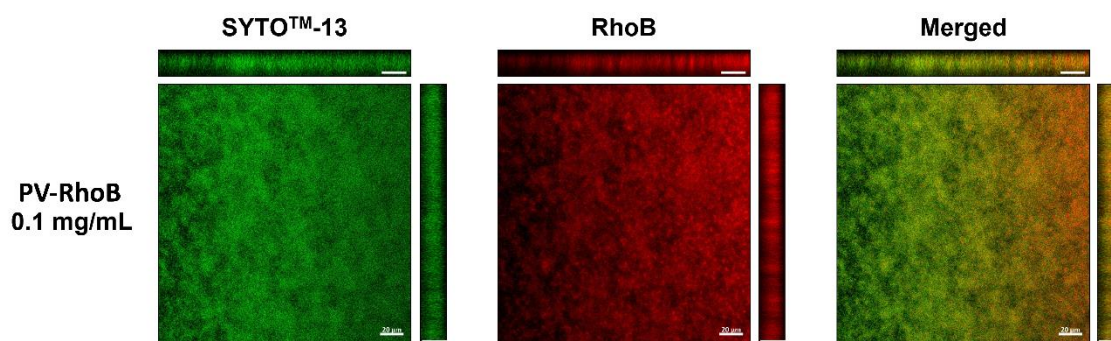

Figure 2.6. 3D-view CLSM images with XY, YZ, XZ projections of *PAO1* biofilms co-incubated with PV-RhoB (scale bar of 20 µm). Vesicles were identified to be evenly distributed.

2.4.5 Established biofilm eradication studies

PV/APR can increase the antibacterial efficacy of APR by interacting with the planktonic bacterial membrane and increasing OM permeability of the bacteria to the drug (**Figures 2.4 and 2.5**), but it has been reported that antibiotics require 10–1000 times higher administration doses to eliminate the biofilms formed by the same strain of planktonic cells [85]. To identify the minimum dosage of free APR in eradicating biofilm, mature *PAO1* (3-day grown) biofilms were incubated with 256, 512, and 1024 µg/mL of APR, which corresponds to concentrations 8, 16, and 32-fold the drug's MIC. Elimination of biofilms was analyzed by observing a decrease in biomass and discontinuity of biofilm structures via confocal images. Results for free APR reveal that a minimum elimination activity ranged between 256 µg/mL and 512 µg/mL (**Figure S2.12**), therefore, 256 µg/mL of APR was chosen as the maximum concentration to compare against equivalent PV/APR in eradication studies on established biofilms.

To compare the biofilm eradication properties of PV/APR, PAO1 biofilms were incubated with 128 and 256 µg/mL equivalent free APR or equivalent PV/APR, followed by staining with SYTO^{TM}-13 and propidium iodide (PI) to identify live/dead cells. Eradication of biofilms was analyzed by observing the reduction in biovolume, calculating the thickness (depth of the thickest section), and by quantitative analysis of fluorescence intensity of live/dead cell staining. Results indicate that APR monotherapy is not as effective at eradicating biofilms at 256 µg/mL APR. In contrast, a significant reduction in biovolume and thickness was observed in the biofilms treated with PV/APR (**Figure 2.7A**), suggesting that the application of the pH-responsive vesicle encapsulated with APR was more successful at eliminating biofilms. In addition, the green

fluorescence intensity from biofilms treated with free APR was not reduced (note that the SYTO^{TM}-13 green fluorescence indicates live cells) and remained between 100-200 a.u. whereas the fluorescence of biofilms treated with PV/APR decreased drastically more, indicating that the vesicle superbly enhanced the bactericidal activity of APR against bacteria inside the biofilm (**Figure 2.7B**). At an even lower APR concentration of 128 µg/mL, PV/APR significantly reduced biovolume and live planktonic cells whereas free APR exerted no effect (**Figure S2.13**). Taken together, the pH-responsive PV interacted superbly with the bacterial membrane via pH-mediated electrostatic interaction and also efficiently protected and delivered APR inside the complex biofilm substructure, thus effectively resulting in better biofilm eradication compared to free APR.

Overall, this study reveals that charge density as a function of pH can lead to differential levels of interactions with the bacterial membrane, ranging from electrostatic membrane adhesions to permeabilization and penetration of the vesicle into the bacteria. Dynamically varying the surface charge of PV as a function of pH enables PV to diffuse throughout the biofilm while retaining positive attributes, such as increased charge density at lower pH, in the vicinity of bacteria biofilm. This effectively results in enhanced antibacterial and antibiofilm properties against not only planktonic bacteria but also difficult-to-treat biofilm bacteria at concentrations significantly lower than those of the free drug.
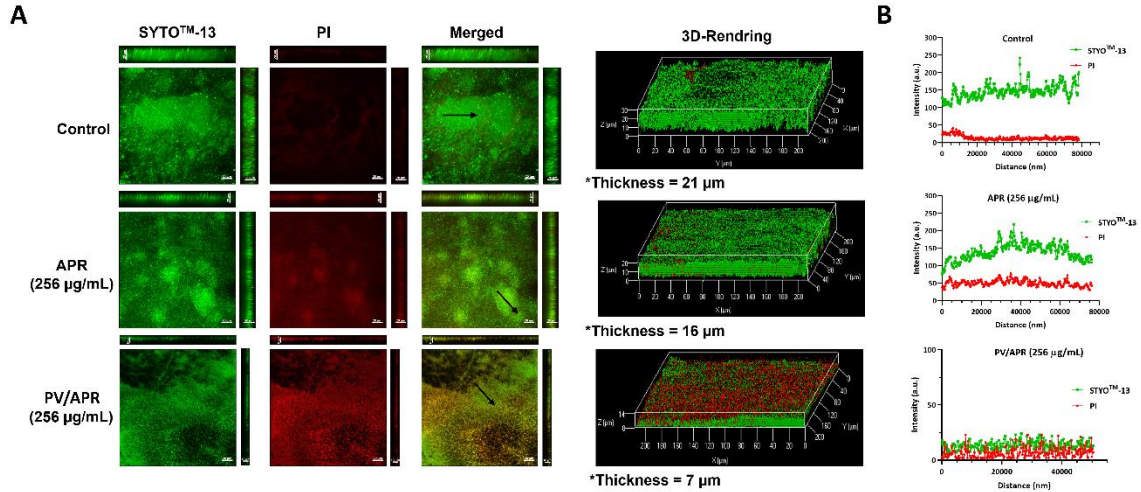
Figure 2.7. The eradication efficacy of PV/APR against established PAO1 biofilm 256 µg/mL equivalent APR. Biofilm was stained with SYTO^TM-13 (green) and propidium iodide (red) was used to identify live/dead cells. (A) 3D-confocal images (XY, XZ, YZ coordinates and rendering) of biofilms reveal a decrease in biovolume and thickness of the biofilms (note that thickness refers to the depth of the thickest section of the biofilm in each image and that arrows indicate the thickest sections in each sample). (B) A quantitative analysis of fluorescence intensity (ZEISS ZEN software) to identify live/dead cells in biofilms. All images were taken with scale bars of 20 µm.

2.5 Conclusions

The amphiphilic diblock copolymer mPEG-*b*-pDEAEMA formed vesicles through self-assembly for encapsulating APR. The pH-responsive property of PV was confirmed by measuring size (z-average diameter) through DLS, bilayer structure of vesicles was confirmed through TEM, charge was measured through zeta potentials, and pH-responsive feature was confirmed through drug release studies. Biofilm penetration studies using PV-RhoB inside established biofilms indicate that the vesicle is able to diffuse through the complex biofilm structure. The biofilm eradication study confirmed that PV/APR showed enhanced antimicrobial and antibiofilm efficacy due to the vesicle's ability to penetrate the biofilm, compromise bacterial membrane integrity, and penetrate into the bacteria to deliver a potentially larger payload of APR at pH 5.5 compared to pH 7.4. Overall, this study reveals that charge density as a function of pH can lead to differential levels of interactions with the bacterial membrane, ranging from electrostatic membrane adhesions to permeabilization and penetration of the vesicle into the bacteria. Taking advantage of the natural low pH in biofilms, this pH-responsive polymeric vesicle was more effective at eradicating existing biofilms compared to free APR and may be especially promising for eradicating pre-existing biofilms in patients suffering from persistent urinary tract infections.

2.6 Supplementary Information: ANTIBACTERIAL AND BIOFILM ERADICATING ACTIVITIES OF PH-RESPONSIVE VESICLES AGAINST PSEUDOMONAS AERUGINOSA

S2.1 Materials and Instruments

Apramycin (APR), mPEG$_{2k}$ (Mn: 2 kDa), 2-(Diethylamino) ethyl methacrylate (DEAEMA), 4-cyano-4-(phenylcarbonothioylthio)pentanoate (CTA), rhodamine B (RhoB) and other chemical compounds were purchased from Sigma-Aldrich. *Pseudomonas aeruginosa PAO1* was purchased from American Type Culture Collection (ATCC). Phosphoryl Chloride (POCl$_3$), Dimethylformamide (DMF), sodium acetate, acetic anhydride, hydroxyethylmethacrylate (HEMA), dicyclohexylcarbodiimide (DCC), 4-dimethylaminopyridine (DMAP), dichloromethane (DCM), Poly (ethylene glycol) methyl ether (Mn 2000), acryloyl chloride were purchased from Millipore-Sigma, TCI, and Fisher scientific and used without further purification.

For chemical analysis, ^{1}H NMR spectra were obtained using a Bruker Advance 400 MHz spectrometer with deuterated deuterium dimethyl sulfoxide (d6-DMSO), methanol (MeOD) and chloroform (CDCl3) as solvents. Spectramax® Plus 384 Microplate Reader (Molecular Devices) were used for UV-Vis spectra analysis. Confocal laser scanning microscopy (CLSM) images of samples were captured using an LSM710 confocal microscope (Carl Zeiss). Flow cytometry studies were conducted using CytoFLEX (Beckman Coulter). Morphological analysis of the polymeric carriers and bacteria were conducted using Transmission electron microscopy (TEM) with the instrument JEOL-JEM1011 with an acceleration voltage of 120 kV and scanning electron microscopy (SEM) on FEI Quanta 200 equipped with accelerating voltage (20 kV). Particle size and Zeta potential were measured with Zeta-sizer Nano ZS instrument (Malvern).

Gel permeation chromatography (GPC) with Shimadzu LC-20 series liquid chromatography instrument was used to characterize the molecular weight distribution of the synthesized polymers after calibrating with polystyrene (PS) standards with DMF as the eluent at flow rate of 0.5 mL/min under room temperature, and the data was analyzed by LCsolution GPC postrun software.

S2.2 Synthesis
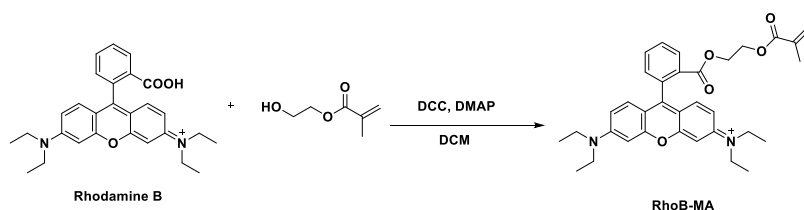
Table S2.1. Synthetic scheme of the fluorescent monomer RhoB-MA

S2.2.1 Synthesis of monomer RhoB-MA

Rhodamine B (1 g, 2.25 mmol) and 2-hydroxyethyl methacrylate (HEMA, 550 µl, 4.5 mmol) were dissolved in dry DCM (15 mL) under nitrogen atmosphere, and the mixture was cooled to 0 ^{0}C, followed by addition of DCC (650 mg, 3.15 mmol) and DMAP (38 mg, 0.31 mmol). The reaction mixture was then stirred for 48 h at room temperature. After the reaction, the mixture was filtered, and the resulted liquid phase was washed with saturated brine for three times and dried over magnesium sulfate. Solvents were removed by vacuum evaporation, and the crude product was further purified by column chromatography on silica gel with DCM/MeOH (10:1 to 6:1) as the performing eluent to obtain red colored RhoB-MA. ^{1}H NMR (400 MHz, CDCl$_3$) δ 8.54

– 8.16 (m, 1H), 7.96 – 7.62 (d, *J* = 7.2 Hz, 2H), 7.11 – 6.99 (d, *J* = 7.4 Hz, 2H), 6.99 – 6.88 (m, 2H), 6.79 (t, *J* = 6.7 Hz, 2H), 6.01 (d, *J* = 12.2 Hz, 1H), 5.65 – 5.49 (m, 1H), 4.42 – 4.26 (m, 2H), 4.19 (dd, *J* = 5.8, 3.6 Hz, 2H), 3.68 – 3.46 (m, 8H), 1.97 – 1.81 (m, 3H), 1.23 (dd, *J* = 8.5, 5.5 Hz, 12H).

Table S2.2. Synthetic scheme of the pH-responsive diblock copolymer mPEG-*b*-pDEAEMA (PV) and diblock copolymer mPEG-*b*-p(DEAEMA-RhoB) (PV-RhoB).

S2.2.2 Synthesis of the mPEG$_{2k}$ macro-RAFT agent (mPEG$_{2k}$-CTA)

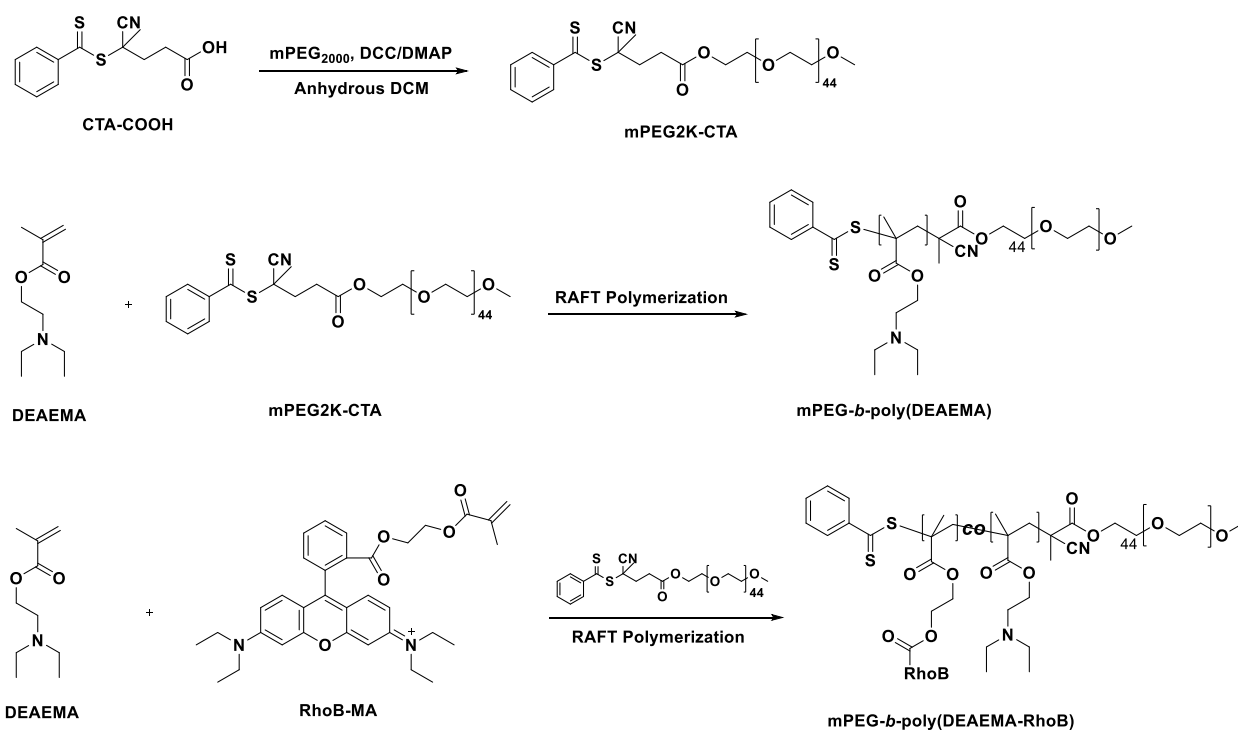The chain transfer agent mPEG$_{2k}$-CTA was synthesized through the reaction of Polyethylene glycol monomethyl ether (Mn 2000) with -cyno-4- ((thiobenzoyl)sulfanyl) pentanoic acid, the chain transfer agent (CTA). Briefly, in a 500 mL one-neck round-bottom flask, CTA (0.82 g, 3.0 mmol) and mPEG–OH (10 g, 5.0 mmol) was dissolved in 100 mL of DCM, and at 0 ^{0}C, 4-dimethylaminopyridine (DMAP) and dicyclohexyl-carbodiimide (DCC) in DCM was added to the solution. After 30 min of initial stirring at 0 ^{0}C, the solution temperature was slowly raised to room temperature and was stirred for another 48 hours. After the reaction, the precipitates were removed by filtration. And the liquid filtrate was evaporated, concentrated, and precipitated into diethyl ether for three times to remove the unreacted starting materials. Then, the crude product was recrystallized three times using EtOH to yield the red-colored product mPEG$_{2k}$-CTA.

S2.2.3 RAFT polymerization of diblock polymer mPEG-*b*-pDEAEMA

The synthesis of mPEG-*b*-pDEAEMA was carried out through the Reversible addition-fragmentation chain-transfer polymerization (RAFT) of the monomer DEAEMA and mPEG$_{2k}$-CTA. Briefly, mPEG$_{2k}$-CTA (100 mg, 1.0 equiv.), DEAEMA (1 mL, 100 equiv.), and 1,4-dioxane (3 mL) were added to a Schlenk flask equipped with a magnetic bar, and the flask was carefully degassed through four times of freeze-pump-thaw cycles and tightly sealed under nitrogen protection. The resulted solution was then heated at 80 °C in an oil bath and stirred for 48 hours, followed by precipitation into an excess of n-hexane, and the precipitates were dissolved into DCM and precipitated again. This precipitation-dissolution cycle was repaired at least three times, and

the resulted final product was dried under a vacuum pump for 48 hours. The molecular weight distribution of mPEG-*b*-pDEAEMA was determined by GPC using anhydrous DMF as the performing eluent, polystyrenes (PS) as the standards, showing an Mn of 16.8 kDa and Mw/Mn of 1.1 (**Table 2.2**). Then, DP of DEAEMA of the synthesized polymer was determined to be 90 by ^{1}HNMR analysis using MeOD as the solvent.
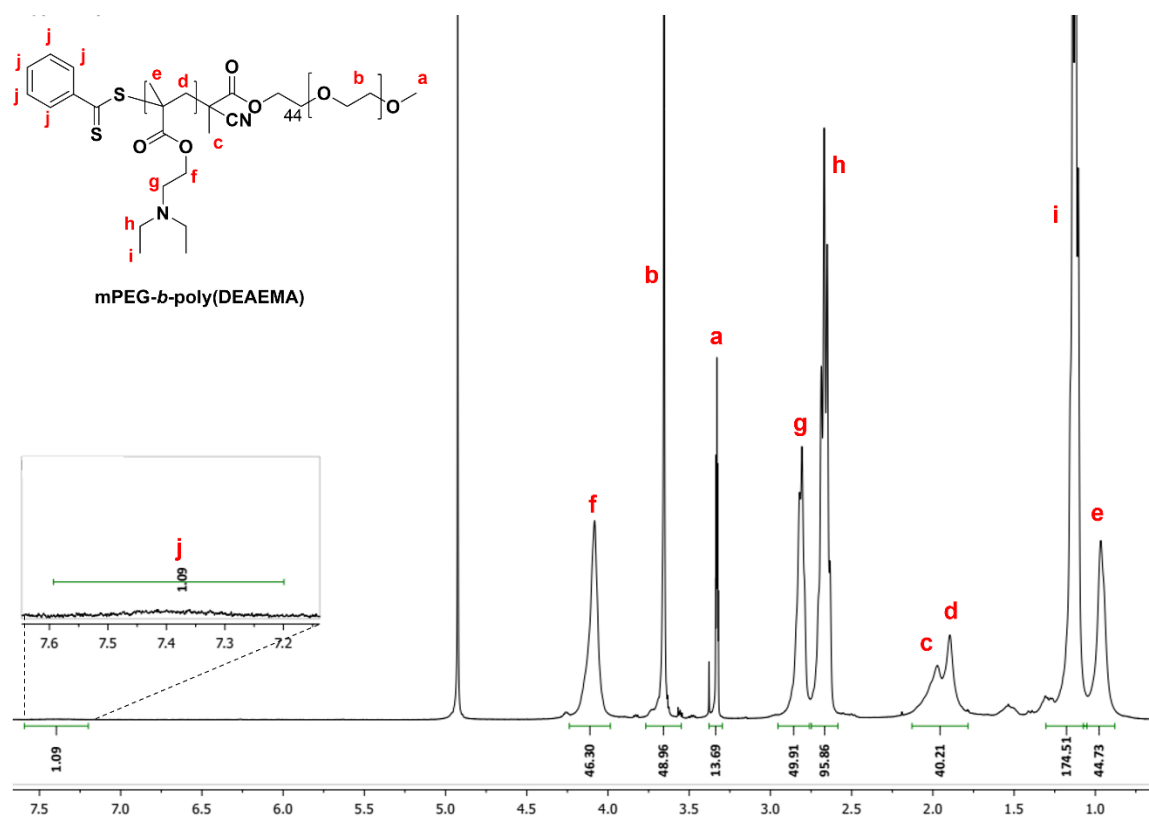
Figure S2.1. ^{1}H NMR of mPEG-*b*-pDEAEMA reveals a degree of polymerization of 90 for DEAEMA relative to PEG$_{2K}$. Peak j corresponds to benzyl peaks of CTA and peak b corresponds to the ethylene protons of PEG; peaks f, g, h, and i corresponds to DEAEMA.

S2.2.4 Synthesis of the fluorescent mPEG-*b*-p(DEAEMA-RhoB)

The fluorescent mPEG-*b*-p(DEAEMA-RhoB) were synthesized as summarized in **Tables S2.1-S2.2**. Detailed synthetic processes and characterization of the monomers (mRhoB), polymer poly (ethylene glycol) RAFT chain transferring agent (CTA) and copolymers are described in **Table S2.2**. The structure was confirmed via ^{1}H NMR analysis using CDCl$_3$ as the solvent.
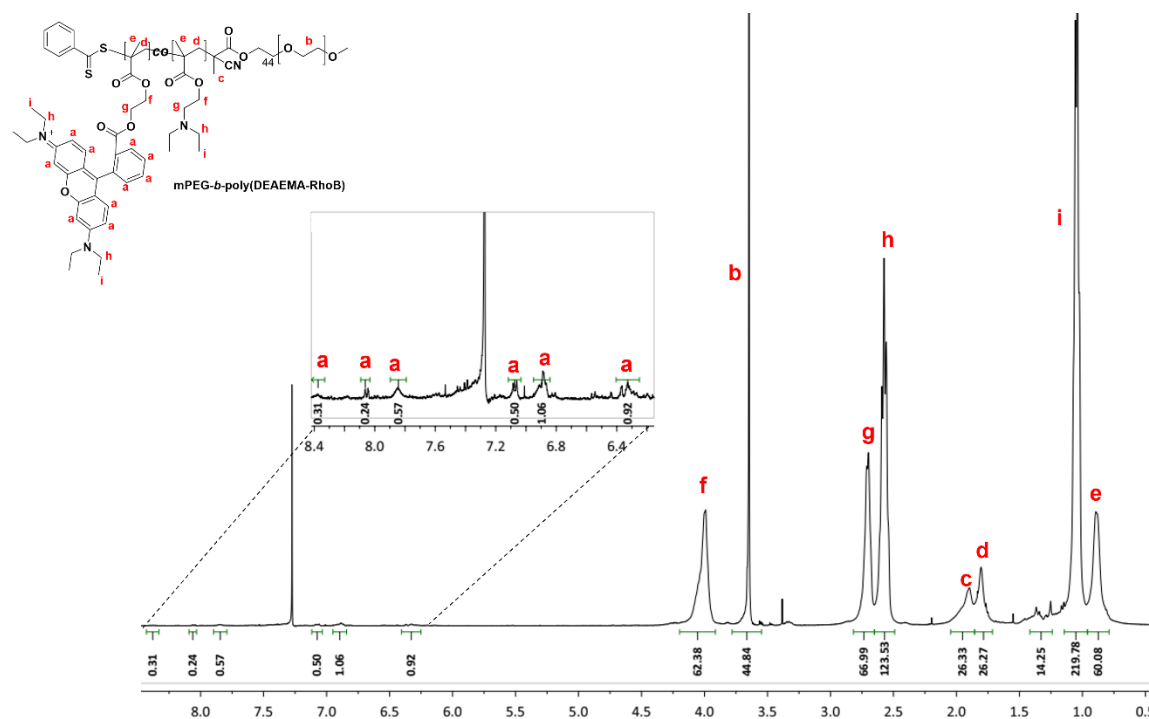
Figure S2.2. ^{1}H NMR spectra of the fluorescent polymer mPEG-*b*-p(DEAEMA-RhoB). The degree of polymerization of RhoB and DEAEMA with respect to PEG$_{2K}$ is based on the integration of peaks a (benzyl peaks of RhoB), ethylene peaks b of PEG, and peaks f, g, h, and i of DEAEMA. The synthesis was conducted at a molar ratio of 0.5:1 RhoB to mPEG$_{2K.}$

S2.2.5 Synthesis of the Dextran-PLGA (DEX-PLGA) and DEX-PLGA-Cy 7.5 and preparation of the micelles.
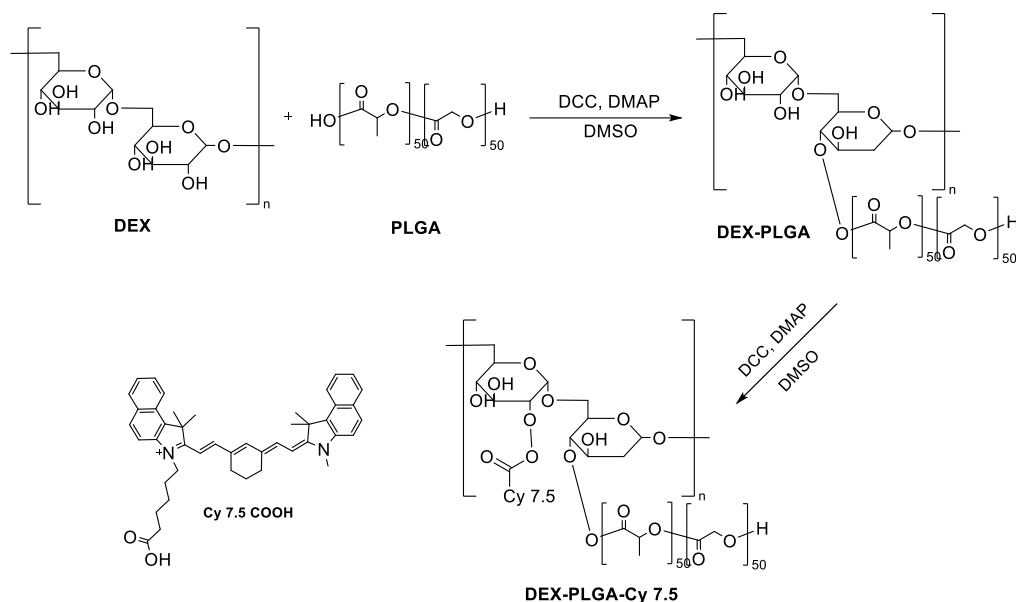
Table S2.3. Synthetic Scheme of the control polymer DEX-PLGA and DEX-PLGA-Cy 7.5

The synthesis of DEX-PLGA was conducted based on previously reported methods with some modifications [86]. Briefly, Poly (D, L-lactide-co-glycolide) (50/50 PLGA, acid terminated, MW 15,000, 100 mg) was in 5 ml of anhydrous DMSO was added with DCC (90 mg) and DMAP (10 mg), and the mixture was reacted for 6 h under nitrogen condition. Then, Dextran (MW 25,000, 200 mg) was added, and the mixture was reacted for additional 48 h at 60 °C. After the reaction is completed, the mixture was added with 10 ml of DI water and went through dialysis in a dialysis tubing (MW 10,000) for 72 h, followed by lyophilization. Then, NMR of the copolymer was analyzed. The synthesis of DEX-PLGA-Cy 7.5 was conducted with similar method. Briefly, 0.5: 1 molar ratio of Cy 7.5 COOH to DEX was reacted with DEX-PLGA after the activation of COOH group with DCC and DMAP. After reaction is completed, the mixture was dialyzed and lyophilized to obtain DEX-PLGA-Cy 7.5.

Preparation of the micelles were conducted through o/w emulsification method, based on the previously reported method to obtain the adequate micelles [86]. Briefly, DEX-PLGA or DEX-PLGA-Cy 7.5 was dissolved in the 1 ml of DMSO, and 10 ml of DI water was added dropwise over 2 h, while the mixture was stirring at room temperature. Then, the mixture was stirred for another 6 h, followed by lyophilization for 72 h for completely removing DMSO. The size of the micelles was confirmed using DLS (**Figure S2.10**).
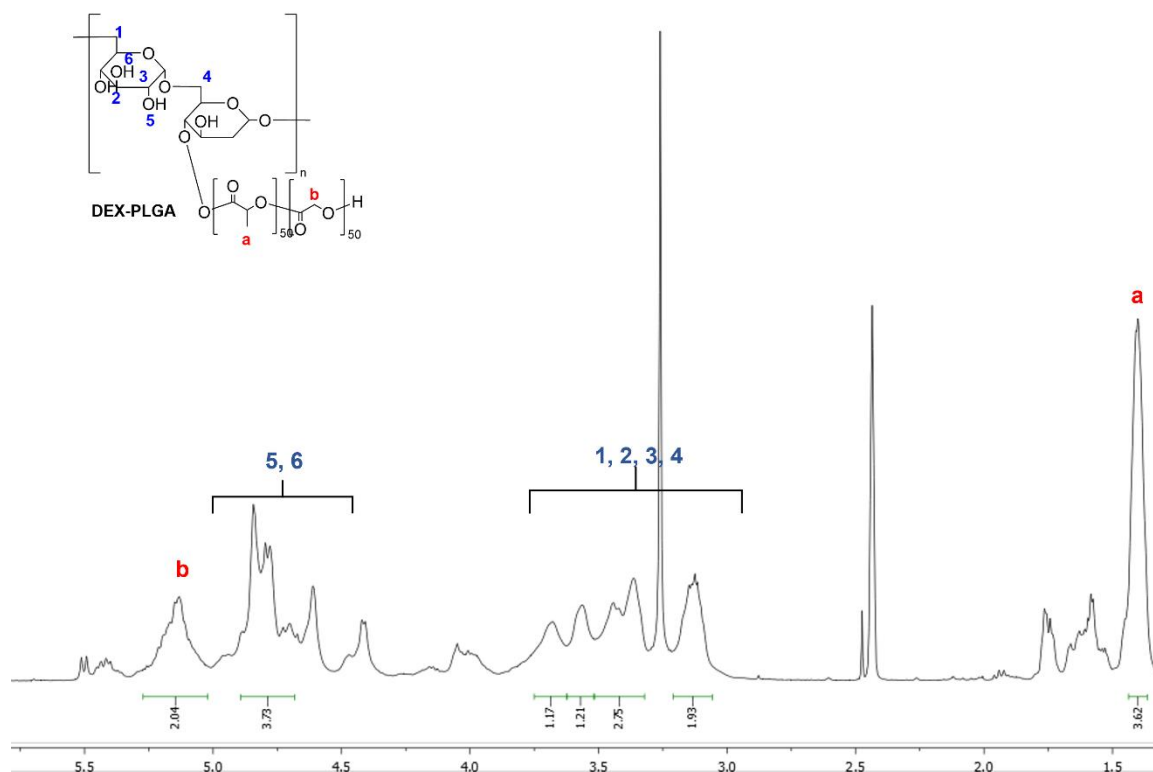
Figure S2.3. ^{1}H NMR spectra of the control polymer DEX-PLGA. The degree of polymerization of PLGA with respect to DEX is based on the integration of peaks a and b (CH_3 and CH_2 of PLGA) and peaks 1 to 6 of dextran.
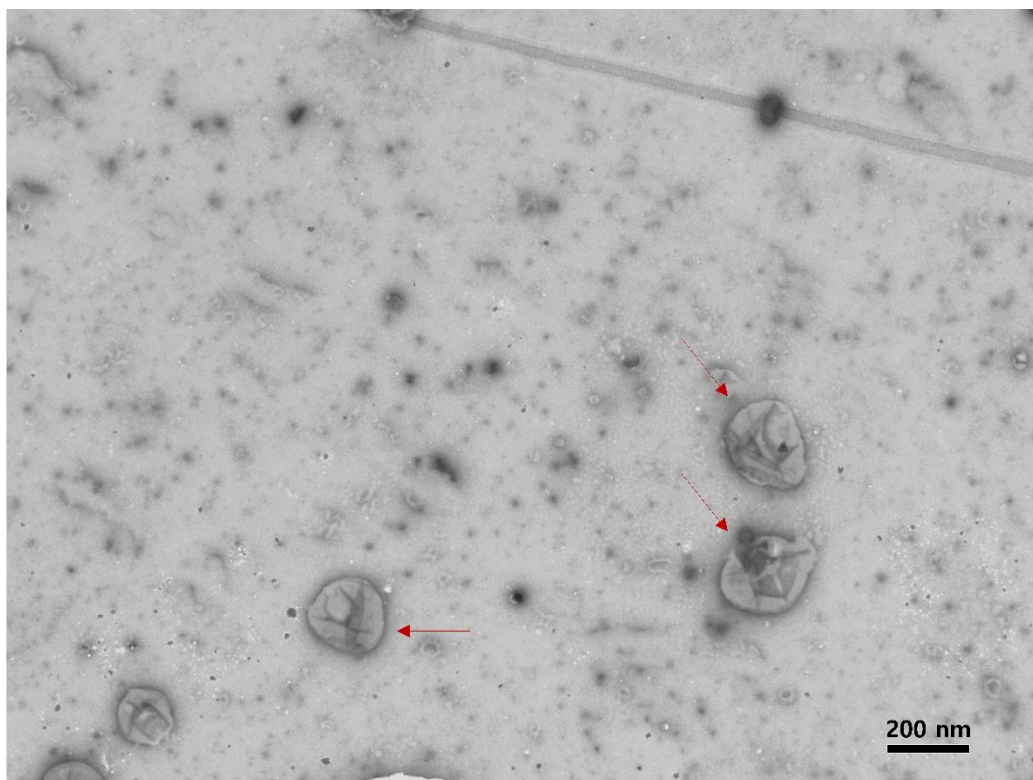
Figure S2.4. TEM image of PV-APR at pH 5.5. Arrows indicate enlarged and disintegrated vesicles upon protonation.
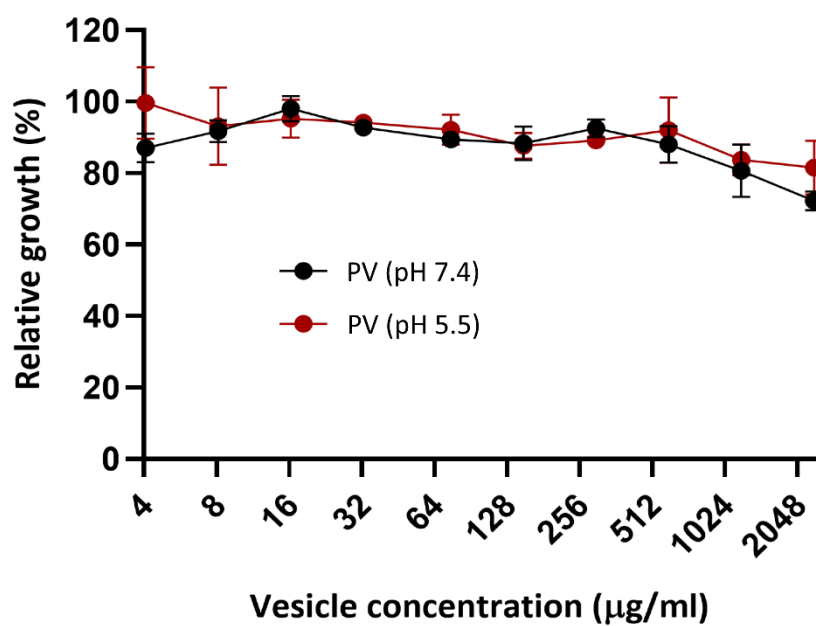
Figure S2.5. MIC of blank PV against PAO1. No significant antibacterial activity was observed.
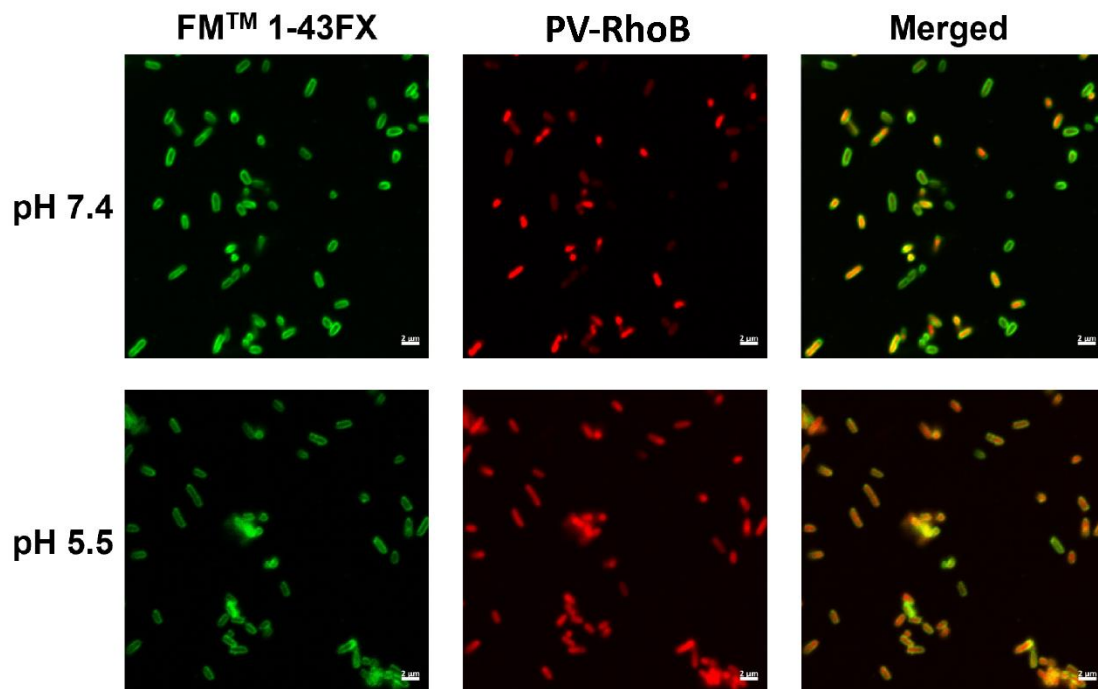
Figure S2.6. Confocal images to visualize the differential degree of interaction between PV-RhoB (Red) with PAO1 bacteria membrane stained with FM^{TM} 1-43FX (green). Images were taken using 20x lens with scale-bar of 2µm.
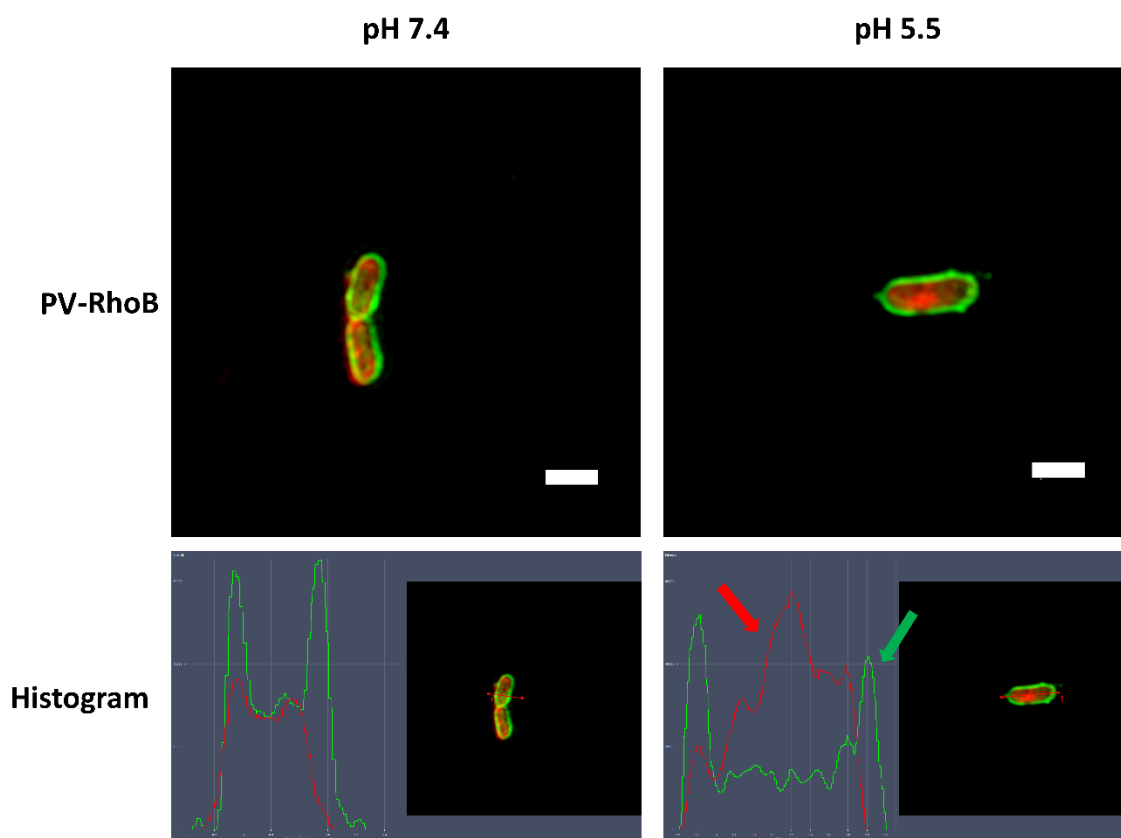
Figure S2.7. Super resolution confocal imaging showing internalization of PV-RhoB (Red) into a single planktonic PAO1 bacteria stained with FM™ 1-43FX (green) at pH 7.4 and 5.5 (scale bar of 1 µm). The histogram represents a horizontal section of bacterium, where the x-axis in the graph represents diameter of the section (bacteria) and y-axis represents intensity of the fluorescence. The green arrow indicates the boundaries of the bacterial membrane, and the red arrow reveals internalization of PV inside the bacterium.
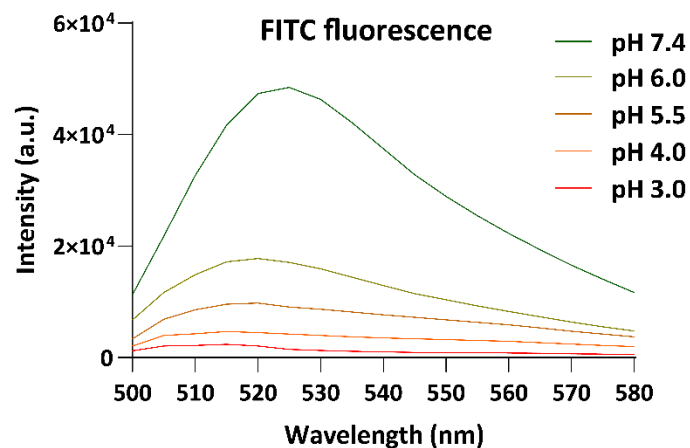
Figure S2.8. The fluorescence intensity of FITC in different pH buffers.
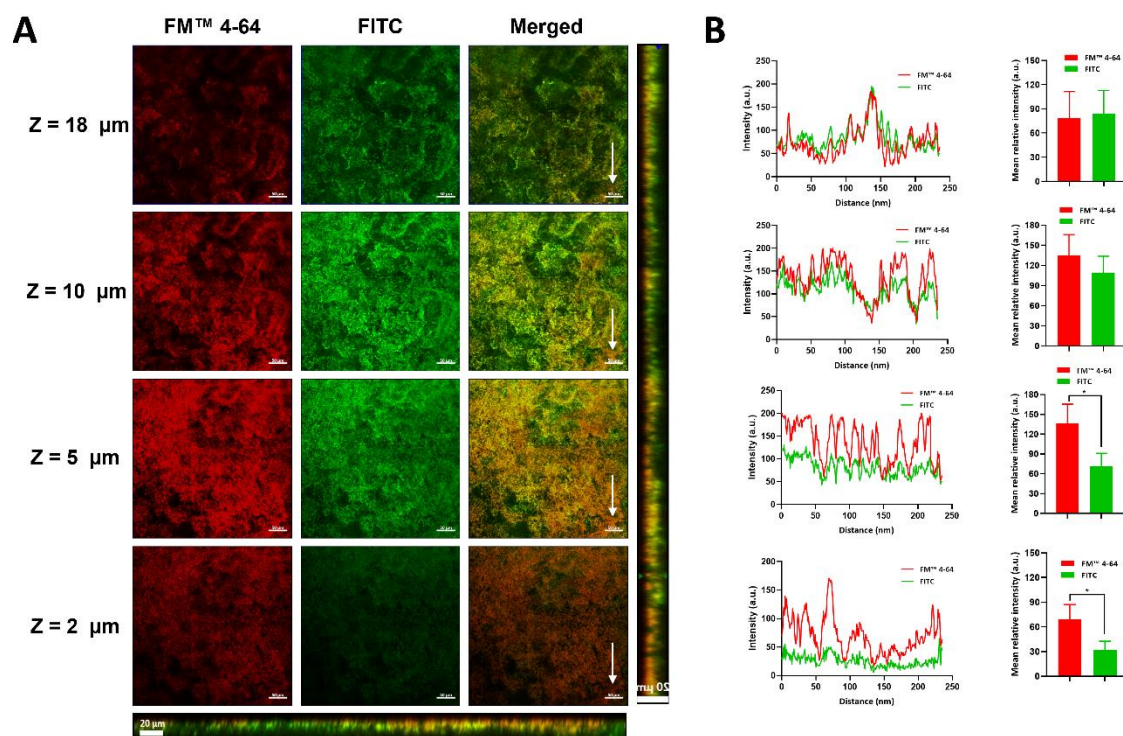
Figure S2.9. Evaluation of acidic inner biofilm microenvironment using pH sensitive FITC. (A) 3D images of the biofilms incubated with FITC (green) for 12 h, followed by staining with the membrane stain FM^{TM} 4-64 (red). The z values indicate height from the bottom of the thickest area

of the biofilm (white arrow). (B) The fluorescence intensity and mean relative intensity of FITC compared to FM^{TM} 4-64 (* p < 0.1). Results showed that the fluorescence of FITC was significantly reduced inside the biofilm.
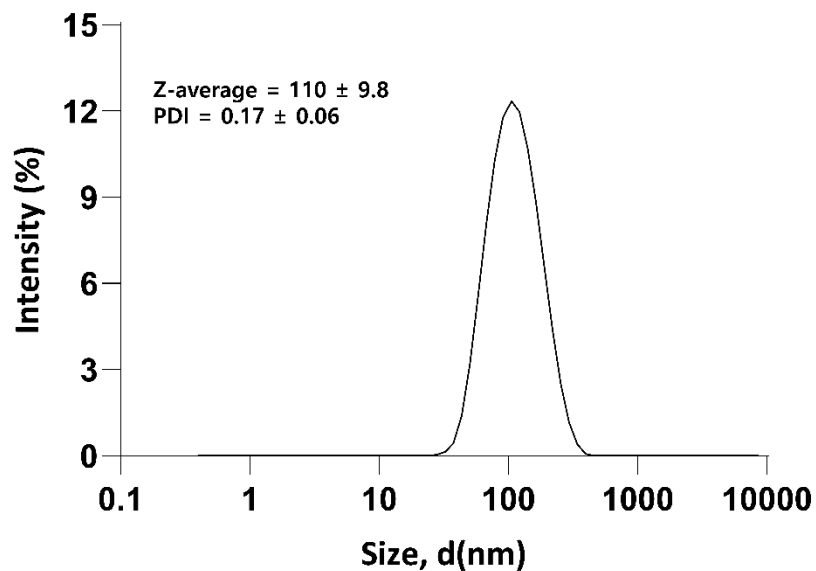
Figure S2.10. Size distribution of the control DEX-PLGA micelle. The average size is 110 ± 9.8 nm. Analysis was carried out in triplicate.

Merged (PV-RhoB + DEX-PLGA-Cy 7.5 + Syto 13)

PV-RhoB + Syto 13

DEX-PLGA-Cy 7.5 + Syto 13

PV-RhoB + DEX-PLGA-Cy 7.5
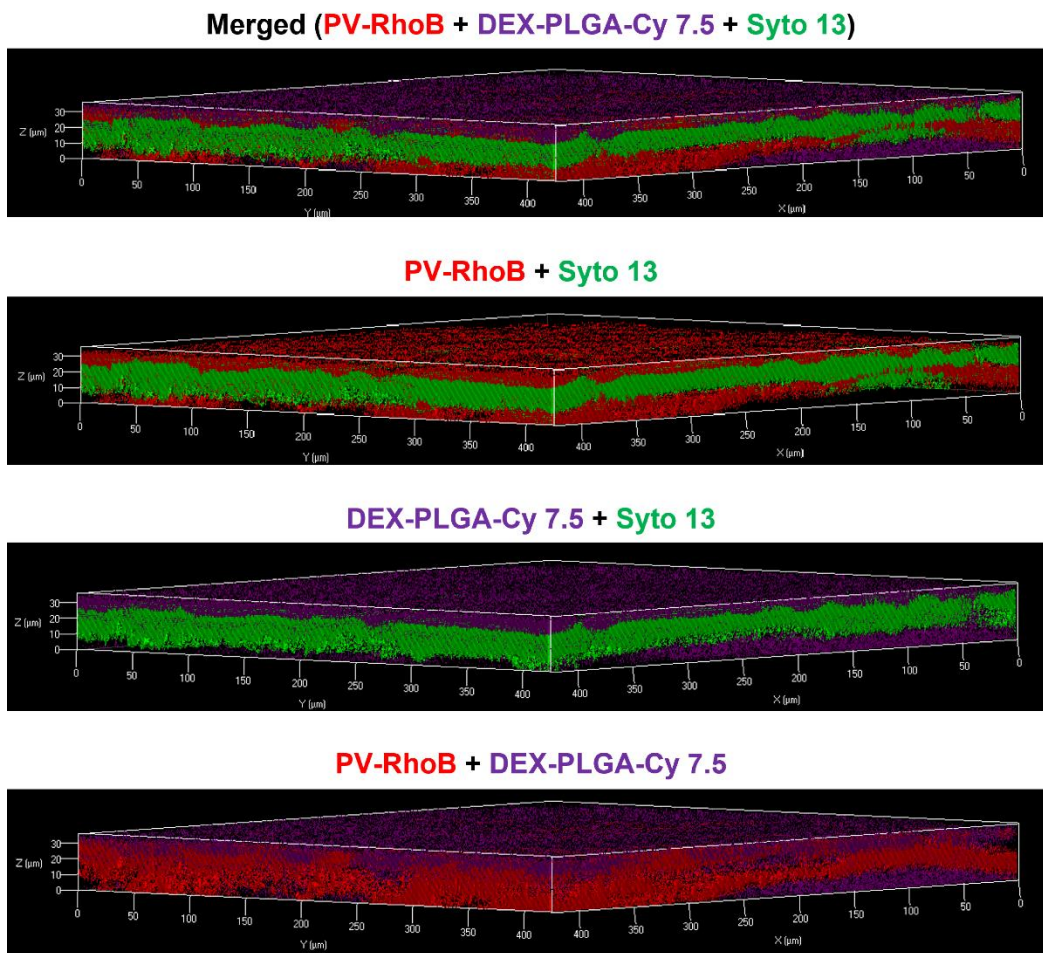
Figure S2.11. Distribution of PV-RhoB and the control DEX-PLGA-Cy 7.5. The 3D images showed that PV-RhoB was evenly distributed inside the biofilm, while majority of the control DEX-PLGA-Cy 7.5 remained on the surface area of the biofilm.
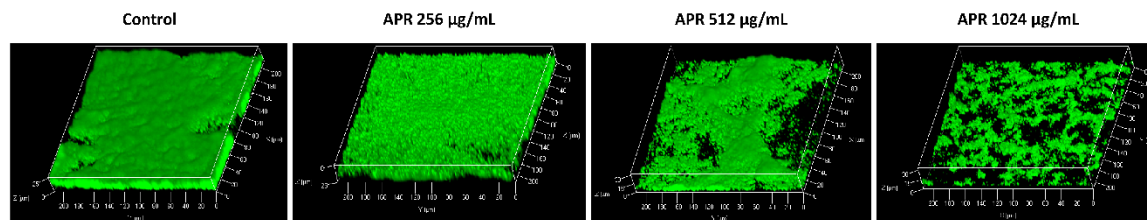
Figure S2.12. PAO1 biofilms treated with 256, 512, and 1024 µg/mL of APR (8, 16, 32-fold of MIC). A clear decrease in biomass is observed at concentrations above 512 µg/mL free APR.
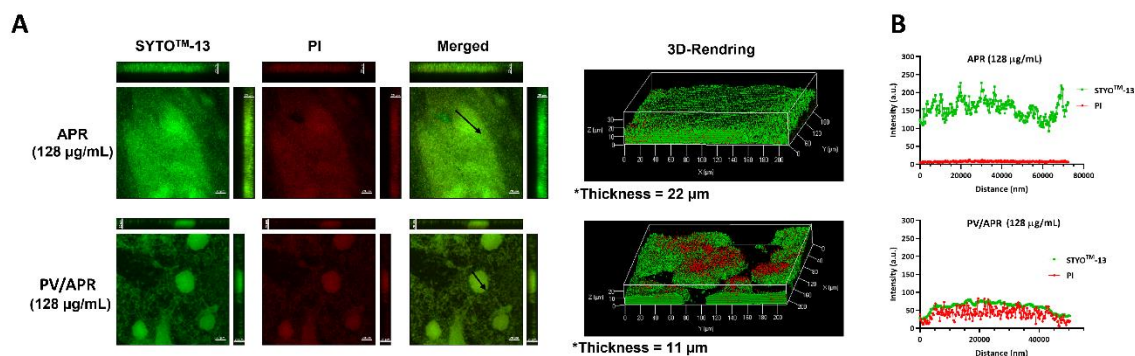
Figure S2.13. PAO1 biofilms were incubated with 128 µg/mL free APR or equivalent PV/APR on a shaker at 37 °C for 24 hours, followed by staining with SYTO^{TM}-13 (green) and propidium iodide (PI, red) for live/dead cell analysis.

CHAPTER 3

ORALLY NON-ABSORBABLE DFO-POLYMER CONJUGATES FOR REDUCING

DIETARY IRON ABSORPTION [2]

_____

3.1 Abstract

Hereditary hemochromatosis (HH) is a non-transfusional genetic iron overload disease where the patients are not able to regulate dietary iron absorption, which ultimately leads to excess cellular iron accumulation. Preventative measures for HH mainly include phlebotomy and asking the patients to minimize dietary iron intake. To investigate alternative iron reduction strategies, we report on prophylactic non-absorbable polymer-deferoxamine conjugates capable of chelating dietary iron and reducing excessive gut uptake of dietary iron. Three different sizes of the conjugates (56 nm, 256 nm, 7.4 µm) were prepared and their physicochemical properties, transit times in the gut under fed/fasted conditions, acute safety, and efficacy at reducing dietary iron absorption in a dietary iron overload mouse model were investigated. The conjugates were synthesized through reverse phase water-in-oil (w/o) emulsification, followed by conjugation of the DFO. *In vitro* studies using Caco-2 transwell assays showed that the conjugates could not permeate across the monolayer, were poorly endocytosed and did not induce cellular toxicity. *In vivo* mice studies indicated that oral gavage of the conjugates remained in the gastric-intestinal (GI) tract for up to 12 h and significantly prevented escalation of serum ferritin levels and excess liver iron accumulation. *Ex vivo* images of the duodenum suggests that smaller sized conjugates perform better at reducing dietary iron due to their longer retention time (entrapment in the villi of the duodenum) and overall slower clearance from the GI tract compared to the larger micron-sized conjugates which transited faster through the gut. Overall, the NG-DFO conjugates designed are orally non-absorbable, safe, and may be suitable for reducing dietary iron absorption when taken with non-heme containing food.

3.2 Introduction

Under normal circumstances, iron homeostasis is maintained in the body and iron is recycled or absorbed from food only as needed. There are two etiology of iron overload in patients: non-transfusional iron overload (NTIO) and transfusional iron overload (TIO). NTIO occurs in hereditary hemochromatosis (HH) when erythropoiesis is normal but too much iron is absorbed through the digestive tract, causing the excess iron to accumulate in hepatocytes of the liver and eventually into the mononuclear phagocyte system (MPS) macrophages and other organs.[87] The danger with iron overloading the hepatocytes in the liver first is that these cells typically don't have a very efficient means of protection against excess iron compared to macrophages. In contrast, TIO is due to inherited hemoglobinopathies and the need for lifelong blood transfusions which result in increased breakdown of senescent red blood cells (RBC) followed by iron accumulation in MPS macrophages first and then parenchymal cells of the body.[87] Regardless of the etiology of iron overload, both NTIO and TIO can progress to iron-induced generation of reactive free radicals in cells and can irreparably damage major organs, including the liver, heart, spleen, and pancreas.[88-91]

NTIO mainly results from increased gastrointestinal (GI) iron absorption in thalassemia intermedia and other hereditary variants of hemochromatosis.[92-94] There are various types of genetic hemochromatosis (Type 1-4) but Type 1 is the most common in the United States and affects about 1 million people of European descent.[46] Symptoms of mild IO are nonspecific, especially at early onset, and phlebotomy is usually recommended to help minimize the more serious side effects of IO. Unfortunately under more severe IO, the high frequency of phlebotomy

required to bring iron loads back to normal range can result in poor patient compliance.[95] Since there is currently no cure for HH, preventative measures are recommended to patients and mainly include minimizing dietary iron intake or increased phlebotomy to reduce iron burden in the body. Herein, an alternative prophylactic approach to reduce GI dietary iron absorption at mealtimes is investigated. The idea of sequestering undesirable ionic species in the gut is not new and FDA-approved products such as Cholestyramine, Welchol, and Renagel currently exist. These non-absorbable polymers can sequester bile acids (Cholestyramine, Welchol) or phosphates (Renagel) from the GI tract to treat various diseases but there are currently very few non-absorbable polymers [96] for sequestering dietary iron to reduce iron uptake by gut cells.

In this paper we report on the preparation, characterization, and administration of non-absorbable DFO-nanogel (NG-DFO) and DFO-microgel (MiG-DFO) conjugates under fasted and fed conditions; specifically, we investigate their transit behaviors in the GI tract and ability to reduce dietary iron absorption in the mouse. We have previously reported that NG-DFO conjugates with acrylamide (AAm) and hydroxyl-glycidyl methacrylate (hGMA) as monomers crosslinked with poly (ethylene glycol) (PEG) remained stable under acidic (pH < 3) and basic conditions (pH >8) for up to 7 days, and displayed good iron chelation efficacy and improved pharmacokinetics in vivo[97]. Considering these stable physicochemical properties, polymeric nanogels as scaffolds are expected to be stable under the harsh conditions of the digestive tract and therefore polymeric scaffolds conjugated to DFO were prepared and investigated as potential non-absorbable macromolecules to chelate and reduce dietary iron absorption.

Since size may play a critical role in the transit of macromolecules through the GI tract, we investigated the effect of polymeric carrier size on GI tract retention time and their overall efficacy in reducing dietary iron absorption *in vivo*. Work by others have demonstrated that smaller nanoparticles (<100 nm) with heavily PEGylated surfaces can enhance oral absorption of some nanoparticles by facilitating their diffusion through the mucus layer and increase bioavailability of drugs[98, 99]. To develop non-absorbable nanocarriers of DFO, we prepared nanogel scaffolds below and above this 100 nm size threshold and synthesized a microgel (MiG) scaffold to investigate the effect of size on GI transit time and oral chelation in a dietary mouse model of iron overload (**Table 3.1**).
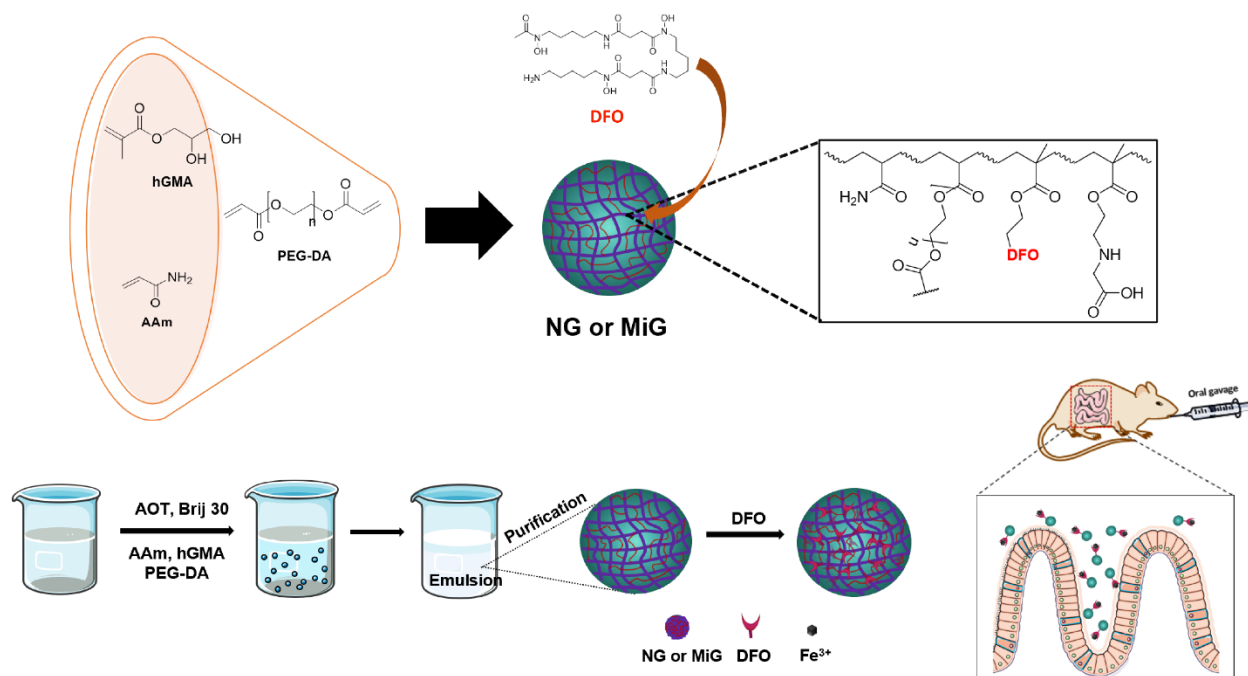
Table 3.1. Preparation of NG/MiG scaffolds as orally administered non-absorbable polymeric carriers of DFO. The scaffolds investigated were synthesized through surfactant-stabilized reverse-phase w/o emulsions followed by polymerization of AAm and hGMA monomers crosslinked by PEG-DA.

3.3 Experimental

3.3.1 Preparation of NG/MiG-DFO conjugates

The polymeric-DFO conjugates were synthesized through water-in-oil reverse-phase polymerization (**Table S3.1**), following previously reported method.[97] Briefly, we chose to synthesize a nanogel scaffold less than 100 nm and another nanogel scaffold larger than 100 nm to investigate the effect of this cutoff size on absorption and GI transit time. To prepare nanogels

less than 100 nm (termed NG1), surfactants AOT:Brij (1g:2g, 1:2 ratio, w/w) were added to 25ml of hexane in 100ml round flask and stirred at 1,500 rpm under vigorous N_2 condition for at least 30 min to eliminate oxygen. Next 50 mg of AAm, 560 µl of hGMA solution (56 mg of hGMA) as monomers, and 125 mg of PEG_{700}-DA as the crosslinker (molar ratio of AAm:hGMA:PEG-DA = 100:50:25) were added with ddH_2O to form 1ml of solution. The hGMA solution was prepared through overnight reflux reaction using 2.7g of GMA in 27ml of ddH_2O. The monomer solution was added dropwise to the hexane solution to form water-in-oil emulsions and the combined mixture was stirred for another 30min under N_2. Ammonium persulfate (APS) solution was prepared using 10mg of APS in 100 µl of ddH_2O and added to the mixture dropwise, stirred for 30 min, and 100 µl of TEMED was added. The final solution was stirred overnight at 25 ºC and hexane was evaporated. The resulting emulsion was washed for 1 h with 50ml of EtOH three times by removing the EtOH layer using centrifugation (3,000 rpm, 10 min). Lastly, 10 ml of ddH_2O was added to the emulsion and sonicated to obtain NG1 averaging 50 nm. The final solution was further purified of excess surfactants using dialysis against ddH_2O (10,000 MW dialysis tube). Synthesis of nanogels larger than 100 nm (termed NG2) was conducted similarly, with the only difference being the surfactant ratio used to control the scaffold size (AOT:Brij = 2:1, w/w). Finally, the microgel scaffold (termed MiG) control in the micrometer range was also prepared using a similar technique but varying the surfactant and monomer/crosslinker ratio. Briefly, 2 ml of Span 85 was added to 200 ml of cyclohexane and the solution was stirred vigorously at 1,500 rpm for 1 h under N_2 condition. Monomer/crosslinker solution was prepared by adding 200 mg of AAm, 250 µl of hGMA, and 1 g of PEG-DA in ddH_2O to form 10 ml of solution. Next, the solution was added dropwise to the cyclohexane stabilized with Span 85 and stirred for another 1 h. Polymerization started by adding 15% w/w APS dropwise in ddH_2O solution to the mixture and

subsequently adding 200 µl of TEMED. The mixture was stirred at 50 ℃ overnight, followed by purification as described above.

Once the polymeric scaffolds of desired sizes were prepared, the conjugation of DFO to these scaffolds were accomplished via Schiff base reaction.[100] Briefly, 10 ml of NG/MiG solution was added with 100mg of NIO_4 and the vicinal diol of the hGMA was cleaved and converted to aldehyde moiety. Next, after purification through dialysis (10,000 MW) with ddH_2O for 24 h, 280 mg of DFO (approximately 1.2:1 molar ratio to aldehyde) was added to the solution and reacted overnight through Schiff base reaction. Subsequently, the imine (N=C) group of the conjugate was further reduced with 100mg $NaCNBH_3$ and remaining unconjugated aldehyde groups were capped with excess glycine to reduce reactivity. The resulting solution was purified through dialysis (10,000 MW) against ddH_2O for 72 h to afford final NG/MiG-DFO conjugates.

3.3.2 Synthesis of Cy5.5-NG/MiG-DFO conjugates

The preparation of the Cy5.5-NG/MiG-DFO conjugates was conducted through amide coupling reaction (**Table S3.1**). Briefly, in 25 ml round flask covered with aluminum foil, 5 mg/ml of NG/MiG-DFO conjugates in ddH_2O was added EDC, NHS, and 20 µl of $Cy5.5-NH_2$ (5 mg/mL), and the resulting mixture was stirred overnight. Unreacted Cy5.5 and excess EDC and NHS were removed through dialysis (10,000 MW) against ddH_2O for 24 h.

3.3.3 Physicochemical properties

Size and polydispersity (PDI) of the NG-DFO conjugates prepared were measured using Dynamic Light Scattering (DLS) and surface properties was studied by monitoring the zeta-potential (Zetasizer Nano ZS, Malvern Instruments, UK). More specifically, analysis of size and PDI was obtained by calculating the z-average diameter (intensity) of NG-DFO conjugates in PBS (2mg/ml) and the zeta-potential was determined by measuring electrophoretic mobility of the conjugates. To verify the morphology and size of the conjugates, Transmission Electron Microscopy (TEM) images were also taken (Georgia Electron Microscopy lab, UGA). Size evaluation of fluorescent Cy5.5-MiG-DFO was determined through confocal microscopy (Zeiss LSM 710 confocal) and analyzed using ImageJ software. Fourier-transform infrared spectroscopy (FTIR) analysis for the conjugates were also conducted using ATR-CRYSTAL FTIR (Bruker).

The ability of NG/MiG-DFO conjugates to chelate ferric iron was verified by monitoring UV-Vis absorption spectra by scanning between 350–650 nm with a SpectraMax Plus spectrophotometer (Molecular Devices) and confirming the magnitude of the absorbance peak at 430 nm, a well-known peak characteristic of DFO chelating ferric iron at a 1:1 ratio.

To determine the conjugation level of DFO to the various scaffolds, the UV-Vis method was utilized as we previously described in detail.[97] Briefly, serial dilutions of 1 mg/ml of DFO in saturated Fe(III) solution provided a reference for absorption curves at 430 nm. Next, 1 mg/ml of NG/MiG-DFO in saturated Fe (III) solution at 430 nm was evaluated, and using the standard

reference curve, DFO concentration was calculated. The w/w ratio conjugation of DFO to the polymeric scaffold was determined using Equation 1:

$$DFO\ ratio\ (wt\%) = \frac{weight\ of\ DFO}{weight\ of\ Polymer-DFO} \times 100 \text{(Equation 1)}$$

3.3.4 Cellular toxicity, permeability, and cell uptake studies

Cultivation of Caco-2 cells was conducted as previously reported.[101] Briefly, Caco-2 cells (ATCC) at ten passages were cultivated for two passages before seeding, and DMEM (without pyruvate) with 50 ml FBS, 5 ml of 100× nonessential amino acids, and 5 ml of PEST (penicillin 10,000 U/ml + streptomycin 10,000 µg/ml solution, 100×) was used as culture medium. The seeding density was 2.27×10^5 cells/cm^2 and cells were incubated at 37 °C, 5% CO_2 in a humid atmosphere for 21–29 days. Maintenance of cells consisted of exchanging medium every other day. To confirm the monolayer integrity of the Caco-2 cells, microscopy, and TEER (Transepithelial electrical resistance) measurements were verified, as previously reported.[101, 102]

For the cytotoxicity studies, free DFO and NG/MiG-DFO conjugates were assessed in Caco-2 cells through a metabolism-based resazurin assay. Briefly, Caco-2 cells were incubated in 96-well plates for 21 days, followed by incubation of free DFO and NG/MiG-DFO conjugates prepared at an initial stock concentration of 400 µM of DFO that was serially diluted 2-fold and incubated for 24 h. After the incubation, the cells were washed with PBS and100 µl of resazurin (stock of 44 µM) was added to each well and incubated for 4 h. Cell viability was determined by

measuring fluorescence intensity at 590 nm using the SpectraMax microplate reader. Cell viability was determined based on fluorescence readings using Equation 2:

$$Caco2\ cell\ viability\ (\%\ decrease) = \frac{F\ (Sample) - F\ (Blank)}{F(Control) - F(Blank)} \times 100$$

(Equation 2)

In addition to cytotoxicity, TEER values were measured using EVOM2[TM] to verify the integrity of the monolayer of Caco-2 cells. Briefly, TEER(Initial) represents the value of intact cell monolayers before administration of formulations and TEER(Final) represents the final value at each time point of the assay after administration of the formulations. Monolayer integrity was calculated using Equation 3:

$$TEER\ (\%\ decrease) = \frac{T\ (Final) - T\ (Blank)}{T(Initial) - T(Blank)} \times 100$$

(Equation 3)

For the cell permeability study, Caco-2 cells were seeded in 12-well transmembrane plates containing filters of pore size < 200 nm. Medium from apical layer and basolateral layer were replenished every other day for 21 days until the cells formed monolayers. Next the media was removed, and cells were washed with HBSS. Based on results obtained from the cell toxicity study, 100 µM of DFO did not adversely affect the viability of cells (>95 % viable) and this concentration was utilized in the permeability study. More specifically, 500 µl of 100 µM DFO or equivalent NG/MiG-DFO conjugates in HBSS solution was added to wells and incubated for up to 24 h. At

different time points (0, 0.5, 1, 2, 4, 8, and 24 h), 50 µl of solutions from both apical and basolateral chambers were collected and added to saturated Fe (III) in HBSS to monitor their absorbance at 430 nm. At the same time, the TEER values were also measured using EVOM^2 (WPI, 240V 50Hz with STX2 electrode) at each time point. Determination of NG/MiG-DFO permeability across the monolayer was investigated by monitoring differences in absorbance at 430 nm between the two chambers. In addition, cell permeability of the formulations was also assessed via fluorescence (more sensitive than UV-Vis) by repeating the studies and monitoring through an IVIS imaging system. Briefly, Cy5.5-NG/MiG-DFO conjugates were seeded in the apical layer of 12-transwell chambers and at each time point 50 µl of solutions from the basolateral layer was collected and fluorescence was evaluated using IVIS at 675 nm.

Finally, for the cellular uptake study Caco-2 cells were seeded in an 8-well chamber slide (Lab-Tek) and cultured for 21 days. After incubation, medium was removed, and cells were washed with DPPS three times. Next, 50µg/ml of Cy5.5-NG/MiG-DFO conjugates and Cy5.5 as control in DPPS were seeded in each well (500 µl) and incubated for 4 h. Solutions were removed and cells were washed with DPPS, fixed with 4 % formaldehyde solution and labeled with the general cell membrane dye FM^{TM} 1-43 FX prior to analysis by confocal microscopy (Zeiss LSM 710 confocal).

3.3.5 NG/MiG-DFO transit study in normal Balb/C mice

All animal experiments were performed in accordance with the guidelines and protocols approved by the University of Georgia Athens's Animal Care and Use Committee guidelines and

the NIH Guide for the Care and Use of Laboratory Animals. Normal Balb/C mice (6 - 8 weeks) were housed in cages in a room maintained at 20 ± 1 ℃ and with 12 h light and dark cycle, with free access to regular chow (Harlan Teklad 5053, no fluorescence, iron content 220 ppm) and water *ad libitum*. Briefly, Cy5.5-NG/MiG-DFO conjugates (100 mg DFO equivalents) solution in 200 µl of PBS were administered into mice fasted for 14 h [103] (n = 3) through oral gavage. Whole body fluorescence images of mice were taken at various time points for up to 24 h by anesthetizing animals with 1.5 % isoflurane/98.5 % oxygen during each imaging event. For ex vivo imaging, mice were euthanized, organs (GI tract, heart, lung, liver, spleen, kidney, and brain) were harvested, and images were immediately taken. All images were captured through sequential acquisition spectra unmixing mode, binning factor of 4, f number of 0.5, and field of view of 12.5 cm. The fluorescence intensity in organs over time was monitored relative to the first time point by selecting fixed regions of interest (ROI) and storing the fluorescence emission signals generated in efficiency units for calculations.

3.3.6 Assessing the efficacy of NG/MiG-DFO conjugates at reducing dietary iron absorption in a mouse model of dietary iron overload

To set up the dietary iron-overload mouse model, female Balb/C mice were either fed with normal chow (Teklad 5053, iron level 200 – 300 ppm) or iron-overloaded chow (carbonyl iron, TD.190344; 20,000 ppm) *ad libitum* for 30 days. Then, mice were sacrificed, and blood samples were collected to assess the serum ferritin levels.

For the efficacy study, female Balb/C mice (6 – 8 weeks) were fed either normal chow (Teklad 5053, iron level 200 – 300 ppm) or iron-overloaded chow (carbonyl iron, TD.190344; 20,000 ppm) *ad libitum* from day 1 to day 28. The mice were divided into six groups: control (normal chow, normal iron level, no treatment), iron-overload control (IO chow, high iron level, no treatment), DFO treated (IO chow, DFO), NG1-DFO (IO chow, NG1-DFO), NG2-DFO (IO chow, NG2-DFO), and MiG-DFO (IO chow, MiG-DFO). The oral gavage dose administered was 500 mg/kg of DFO or equivalent NG/MiG-DFO conjugates in PBS, administered to each respective group through oral gavage every 12 h starting from day 1 to day 28 (4 weeks). At the 2-week and 4-week timepoints, mice were sacrificed, blood was collected through retro-orbital puncture and organs were then harvested. The blood was centrifuged (4,500 rpm, 15 min) to obtain serum and ferritin levels were evaluated using Mouse Ferritin ELISA Kit (ICL ANTIBIODIES, INC). Liver iron concentration for the different treatment groups was evaluated relative to the weight of the freeze-dried liver tissue and the Fe (III) concentration in the sample was measured using ICP-MS (Center for Applied Isotope Studies, UGA). Organs including livers, stomach, small intestine and large intestine were collected and immunohistology studies were conducted by preparing tissue samples in cassettes (UGA histology lab) and iron-induced liver toxicity profiles were analyzed by evaluating liver alanine transferases (ALT) and liver aspartate transferases (AST) in mice serums (UGA Veterinary Teaching hospital).

3.4 Results and discussion

3.4.1 Physicochemical characterizations

Two nanogel scaffolds averaging 56 and 246 nm were synthesized following previously published procedures [97]. The apparent sizes were confirmed using DLS (**Figure S3.1A**) and TEM (**Figure 3.1A and B**) whereby z-average (d) of 56 ± 4 nm with PDI 0.16 was obtained for NG1-DFO and 246 ± 8 nm with PDI 0.14 was obtained for NG2-DFO. Size of Cy5.5-MiG-DFO averaged 7.39 ± 1.9 µm using confocal microscopy (**Figure 3.1C**) and ImageJ software-mediated statistical analysis (**Figure S3.1B**). Next, DFO conjugation to NG and MiG scaffolds was confirmed through UV-Vis by adding excess concentration of Fe(III) solution to the conjugates since iron is known to chelate to DFO at 1:1 molar ratio [104]. Samples were repeatedly washed with centrifugal filter tube (MWCO 10,000) to successfully remove excess iron or unconjugated free DFO prior to UV analysis. DFO:Fe(III) complex shows absorbance at 430 nm under UV-vis, [14] with samples tested confirming that DFO was successfully conjugated to the polymeric carriers (**Figure 3.1D**). FTIR spectra of the conjugates were analyzed to further confirm that the conjugation was successful (**Figure S3.2**).
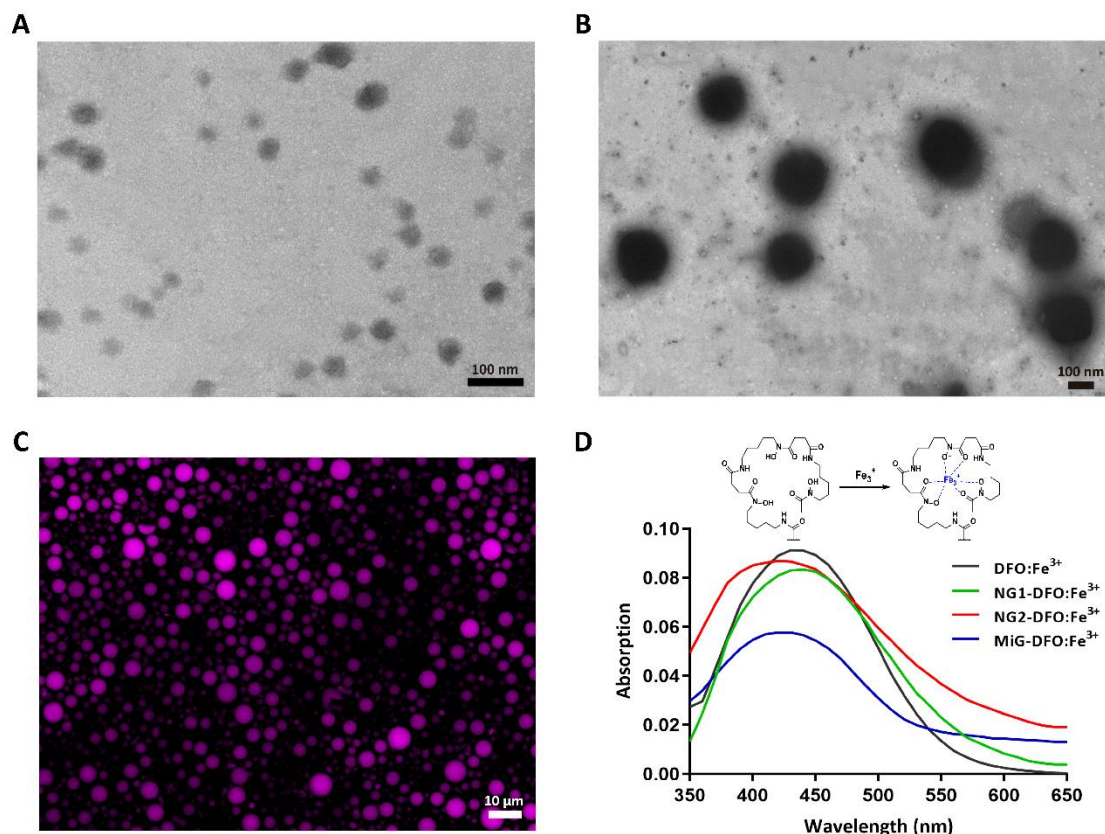
Figure 3.1. (A) and (B) Transmission electron microscopy (TEM) images of NG1-DFO and NG2-DFO (scale bars of 100 nm). (C) Size of MiG-DFO was confirmed through CLSM after labeling with Cy-5.5 and was analyzed using ImageJ. (D) UV-vis absorption of the conjugates complexed to Fe (III) showed strong absorbance at 430 nm for all conjugates.

The conjugation level of DFO to NG/MiG-DFO scaffolds was calculated based on UV-Vis absorption with respect to a standard reference curve. The standard curve was generated by mixing 1mg of free DFO with 1ml of standard Fe (III) solution (1 mg /ml) for 1 h, followed by 2-fold serial dilution and monitoring the absorbance at 430 nm. The absorbance of free DFO-Fe (III) generates a linear equation. Next, 1 mg of NG/MiG-DFO conjugates were thoroughly mixed with the same standard Fe (III) solution for 1h, and their absorbance at 430 nm was evaluated. Based

on the absorbance of samples and using the standard linear equation generated, the amount of DFO present in NG/MiG-DFO scaffolds was calculated. All physicochemical characterization data are summarized in **Table 3.2**.

Table 3.2. Physicochemical Characterizations of NG/MiG-DFO conjugates

Samples	Surfactants	Surfactant ratio	ζ	D^a	PDI^a	DFO ratio^b
			mV			(wt%)
NG1-DFO	AOT:Brij30	1 : 2 (w/w)	2.38 ± 0.4	56 ± 4 nm	0.16 ± 0.02	19.8 ± 6.7
NG2-DFO	AOT:Brij30	2 : 1 (w/w)	1.49 ± 0.8	246 ± 8 nm	0.14 ± 0.07	18.7 ± 2.3
MiG-DFO	Span85	1 % (v/v)	−	7.39 ± 1.9 µm	−	11.6 ± 1.9

^{a} D = diameter and PDI were determined by DLS. ^{b} DFO ratio was defined by measuring absorbance at 430nm using UV-vis after incubation with Fe (III) solution. The standard curve was prepared by measuring absorbance at 430 nm using 2-fold dilutions of free DFO- Fe (III) solutions to calculate total w/w percentage of DFO conjugated to scaffolds in each formulation.

3.4.2 Cellular toxicity and permeability studies

Cell viability study on Caco-2 cells using the resazurin assay revealed very little evidence of cytotoxicity when up to 400 µM free DFO or equivalent NG/MiG-DFO was added to cells (**Figure S3.3B**). Cells were incubated with free DFO or NG/MiG-DFO conjugates for 24 h, and results showed no evidence of mitochondrial disruption with over 95% cell viability.

To evaluate the permeability of NG/MiG-DFO conjugates across endothelial cells of the gut, an *in vitro* model based on Caco-2 cells was established as previously reported (**Figure S3.3A**)

[101]. Briefly, cells were seeded in transwells placed into plates to generate a culture system with an apical layer and basolateral layer. Then, NG/MiG-DFO conjugates (100 µM equivalent DFO) were added to the apical layers and the cells were incubated up to 24 h. At 0, 2, 4, 8 and 24 h time points, 50 µl of solutions from both apical and basolateral layers were collected and mixed with excess Fe (III) solution and the absorbance at 430 nm was evaluated. Results based on absorbance from the DFO:Fe(III) complex reveal that NG/MiG-DFO conjugates were incapable of permeabilizing the Caco-2 cell monolayer (**Figures 3.2A and B**). Interestingly, monolayers treated with free DFO showed differences in absorbance over time suggesting that the monolayer was not intact and/or that cell growth was affected by the free drug. In addition to absorbance, we also measured TEER values for all monolayers treated with free DFO or NG/MiG-DFO conjugates at 0, 4, 8, 12, 16, 20, 24 h time points to try and tease apart cellular toxicity from monolayer integrity. A decrease in TEER values could indicate compromised caco-2 cell monolayer integrity but the decreased TEER could also be due to the formulations being cytotoxic and thus indirectly affecting monolayer integrity. Overall, cells treated with NG/MiG-DFO conjugates did not show decrease in TEER values over time, but free DFO treated cells did show reduced TEER values, with approximately over 70% decrease (**Figure 3.3C**). To start teasing apart the effect of free DFO toxicity from monolayer integrity, we narrowed the timeframe investigated from 24 h down to 2 h. Results revealed that at 2 h, both conjugates and free DFO are not permeable and have no effect on the monolayer integrity based on TEER values (**Figures S3.3D and S3.3E**). At longer times, free DFO is known to induce cellular toxicity and adverse effects when administered to patients,[105] and cytotoxicity may also partially be attributed to the reactive terminal amine of the free drug since conjugation of this end group to polymers tends to correlate with an increase in cell viability at the same equivalent concentration.[57]. Although free DFO did not show any

toxicity directly to cells at 2 h based on the resazurin assay (**Figure S3.3B**), it is likely that high concentration of DFO with long incubation time may hinder the monolayer integrity **(Figure 3.2C).** Thus, this study suggests that NG/MiG-DFO are less toxic to caco-2cell monolayers than free DFO but that both the free drug and the conjugates do not cross intact endothelial cell monolayers.

The cellular permeability of NG/MiG-DFO conjugates was also confirmed through fluorescence detection which is more sensitive than UV-Vis by labeling constructs with Cy 5.5 (1 % w/w) and conducting the trans-well mediated assay as before. Briefly, at 0, 0.5, 1, 2, 4, 8, 12, and 24 time points, solutions from basolateral layers were collected and the fluorescence was evaluated using IVIS. As seen in **Figure S3.3C**, no fluorescence was detected from the basolateral layers, thus confirming that the conjugates cannot permeate across the intact caco-2 cell monolayer.
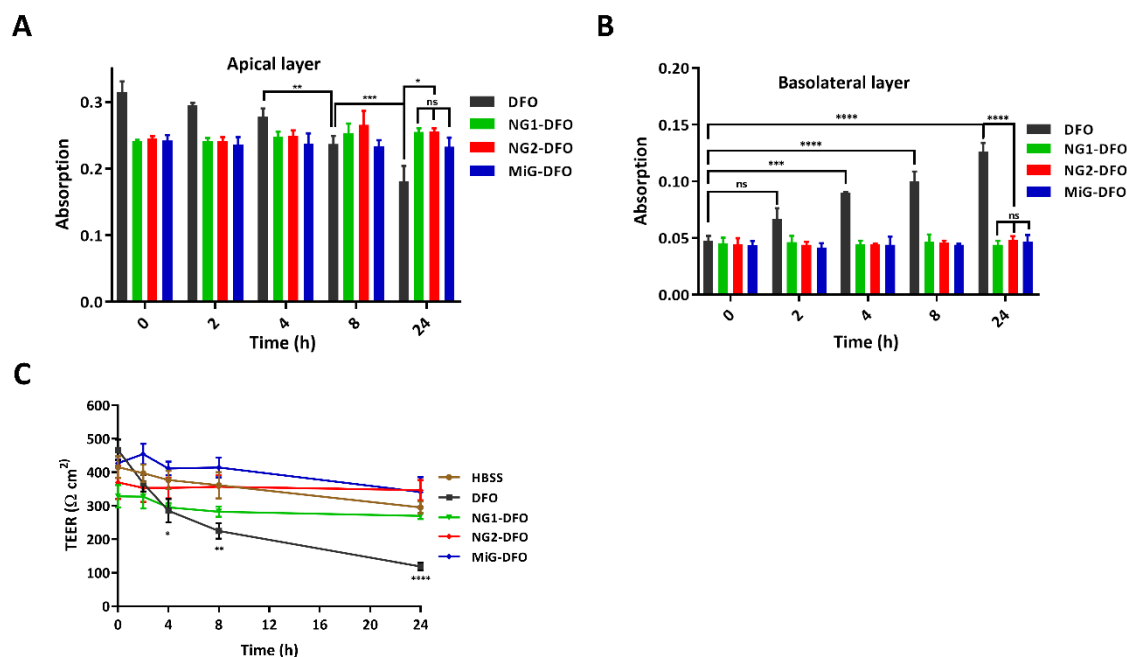
Figure 3.2. (A) Absorbance of apical layer and (B) basolateral layer indicated that DFO was permeable over time while the conjugates were not. (C) TEER values of the monolayers treated with free DFO or NG/MiG-DFO conjugates. All results are presented as mean ± SD (n = 6) where * p < 0.05, **p < 0.01 and *** p <0.001.

3.4.3 Cellular endocytosis assay

NG/MiG-DFO conjugates cannot permeate through the *in vitro* caco-2 cell monolayer however the cells may still be able to endocytose the conjugates. To investigate this further, Cy5.5-NG/MiG-DFO conjugates (100 μM equivalent of DFO) was incubated with caco-2 cells for 8 h and evidence of endocytosis was monitored through Confocal Laser Scanning Microscopy (CLSM). Briefly, cells were incubated with the conjugates and washed with DPPS three times before labeling the cell membranes with a fluorescent dye (FMP 1-43FX. After labeling, cells were

washed again three times, followed by fixing and imaging using CLSM. The dye Cy5.5 was used as a positive control for uptake into cells via co-treatment with triton to compromise the cell membrane. Results revealed that free Cy5.5 indeed localized inside cells and also adhered to the membrane (**Figure 3.3**). In contrast, NG/MiG-DFO conjugates showed no evidence of uptake into cells and low adherence to the membrane. This study demonstrates that Caco-2 cells do not endocytose NG/MiG-DFO conjugates nor do the neutral surface properties of the nanocarriers result in adherence to the cell membrane at the 8h timepoint tested.

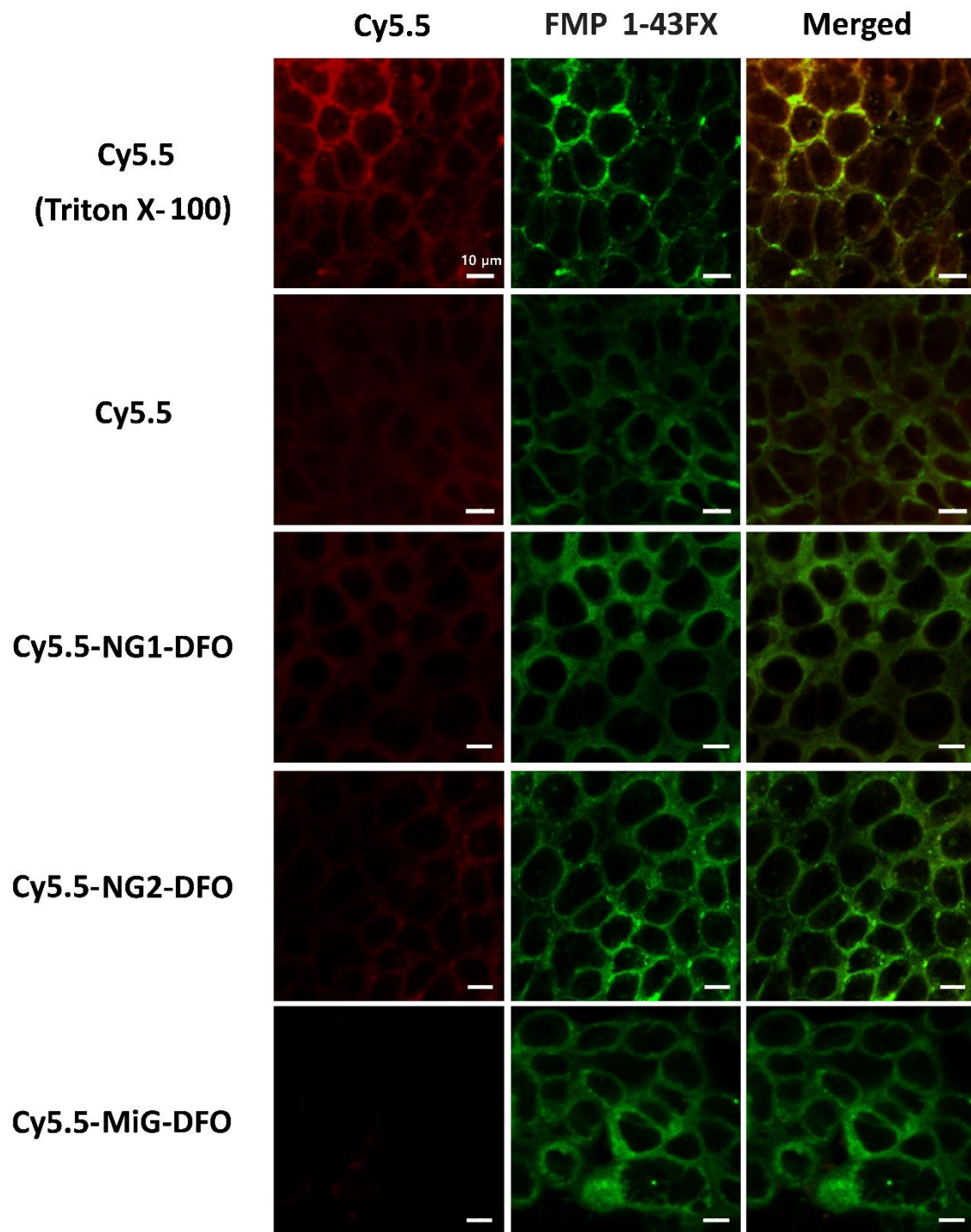|	Cy5.5	FMP 1-43FX	Merged
Cy5.5 (Triton X-100)			
Cy5.5			
Cy5.5-NG1-DFO			
Cy5.5-NG2-DFO			
Cy5.5-MiG-DFO			

Figure 3.3. Cell endocytosis assays at 8 h were performed in caco-2 cells treated with NG-DFO and MiG-DFO conjugates labeled with Cy5.5. Other controls included free Cy5.5, and Cy5.5 and

Triton X-100. All images were captured using CLSM (scale of 10 µM). Results indicate that neither NG1-DFO and NG2-DFO or MiG-DFO were endocytosed.

3.4.4 *In vivo* GI transit of NG/MiG-DFO conjugates in fasted Balb/C mice

To investigate the absorption properties of NG/MiG-DFO conjugates in vivo, we monitored the transit behavior of formulations in fasted female Balb/C mice (6 – 8 weeks). Mice were fasted for 24 h prior to being administered 200 µl of the conjugates (500 mg/ml equivalent DFO) in PBS buffer through oral gavage and full body fluorescent images were taken using IVIS at 1, 2, 4, 8, 12, and 24 h time points. Results revealed that the intensity of fluorescence for all conjugates decreased over time, but the rate of decrease was more rapid in mice administered MiG-DFO and is indicative of the larger micro conjugate transiting through the GI tract faster (**Figure 3.4A**). There was no obvious difference in transit time between the ca. 56 and 246 nm NG-DFO conjugates. The relative intensity of fluorescent region at each time point investigated was monitored by fixing the Region of Interest (ROI) of fluorescence at the 1h time point at 100% and then monitoring the decrease in ROI fluorescence over time to evaluate the retention property of NG/MiG-DFO conjugates in the mouse (**Figure S3.4A**). In the graph, the time point for 50 % of reduction in ROI for both NG-DFO formulations occurred ca. 4–6 h and at ca. 2 h for MiG-DFO. For example, in **Figure 3.4A**, the fluorescent images for the two NG-DFO formulations did not drastically change at 2 h whereas the intensity was visually more reduced for mice administered MiG-DFO. This visual difference in transit time between NG-DFO and MiG-DFO was also observed at 8 and 12 h time points (**Figure 3.4A and S3.4A**). In general, all three conjugates remained in the mouse GI tract for at least 4 h but there was a significant difference in transit time

between smaller nanometer-sized Cy5.5-NG-DFO conjugates compared to the larger sized Cy5.5-MiG-DFO.

To investigate the distribution of the conjugates further, fasted mice were administered Cy5.5-labeled formulations via oral gavage and sacrificed at 4 h; organs such as the GI tract (stomach, small and large intestines), liver, lung, spleen, kidneys and heart were then harvested. Through ex vivo IVIS fluorescence imaging of these organs, we noticed no fluorescence in the liver, lung, spleen, kidneys or heart of animals (**Figure S3.4B and C**). There were obvious visual differences in fluorescence between both NG-DFO and MiG-DFO in the GI tract but there was no major visual difference between the 56 and 246 nm NG-DFO conjugates at 4 h (**Figure 3.4B**). More specifically, both NG-DFO conjugates remained in the stomach and duodenum (see arrows in **Figure 3.4B**) but almost all MiG-DFO had accumulated in the large intestine at 4 h. This study confirms that the NG/MiG-DFO formulations were entrapped in the small intestine longer in fasted mice compared to MiG-DFO. In other words, all the conjugates appeared to be orally non-absorbable but micron-sized polymeric carriers transited through the GI tract 2-3 times faster than smaller nanometer-sized carriers.
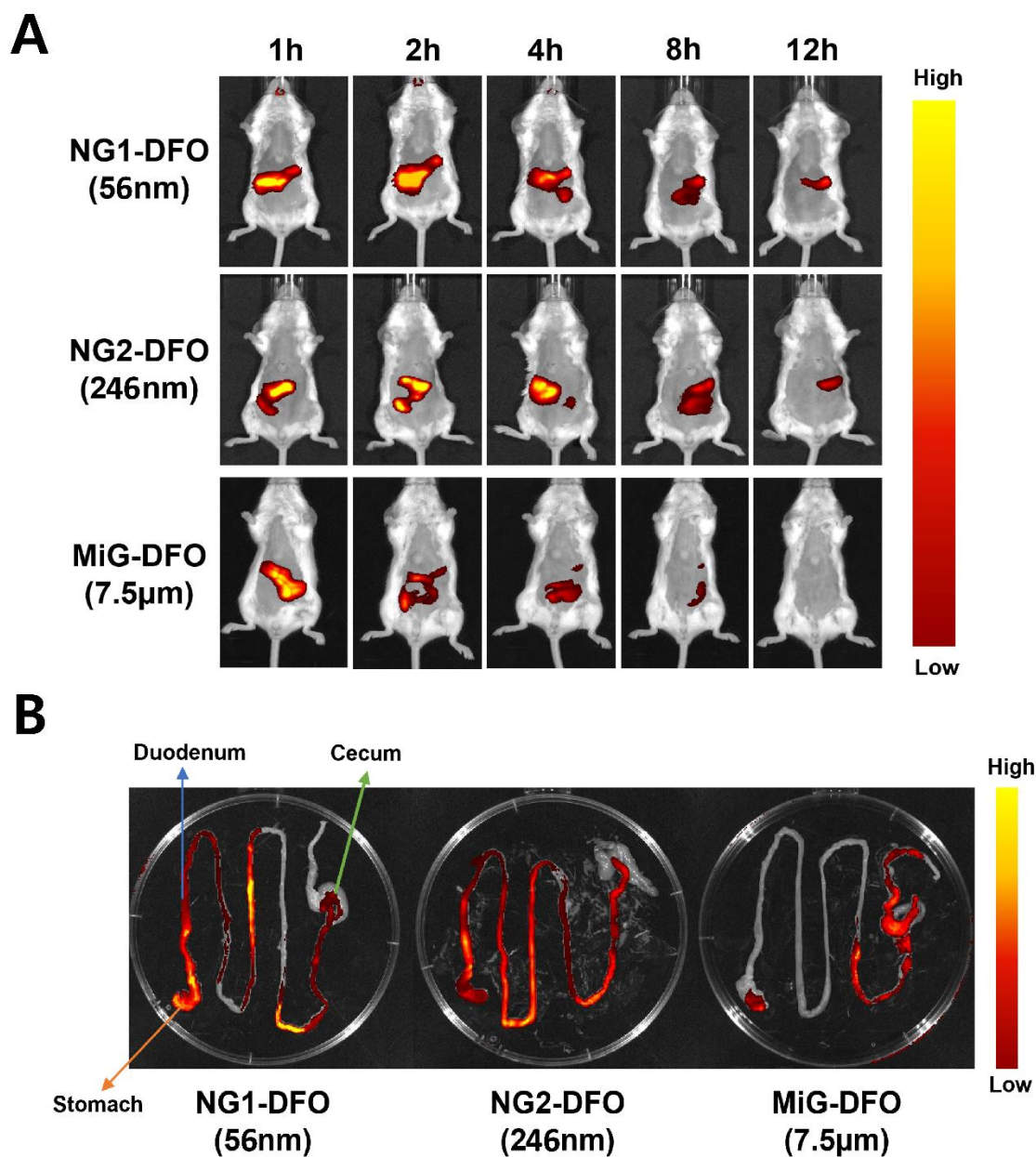
Figure 3.4. Fasted female Balb/C mice were orally gavaged with NG-DFO or MiG-DFO conjugates (500 mg/kg of DFO) and fluorescence images were taken at each indicated time point up to 12 h. The intensity of fluorescence (counts) was measured through IVIS. (A) Comparison in fluorescence of GI tract of mice administered different conjugates. (B) Ex vivo data of mice 4 h after oral gavage of conjugates. Results showed apparent difference between NG-DFOs and MiG-DFO, indicating the larger micron-sized conjugate transited faster.

In vivo transit studies suggest that MiG-DFO transit in the mice GI tract was faster than NG-DFO conjugates. To investigate this further, NG/MiG-DFO conjugates were administered as before at 500 mg/kg equivalent DFO and GI tract organs collected at 4 h (**Figure 3.5**). Thin GI tract specimen from animals were membrane stained with Fm^{TM} 1-43 Fx and imaged using CLSM. The confocal results clearly show fluorescence from nanosized formulations entrapped between the villi of the duodenum for both NG1-DFO and NG2-DFO whereas there was no fluorescence detected in duodenum treated with MiG-DFO (**Figure 3.5 and Figure S3.5**). This suggests that smaller NG-DFO conjugates transit time may be slower due to entrapment in the intestinal mucosa compared to larger MiG-DFO.
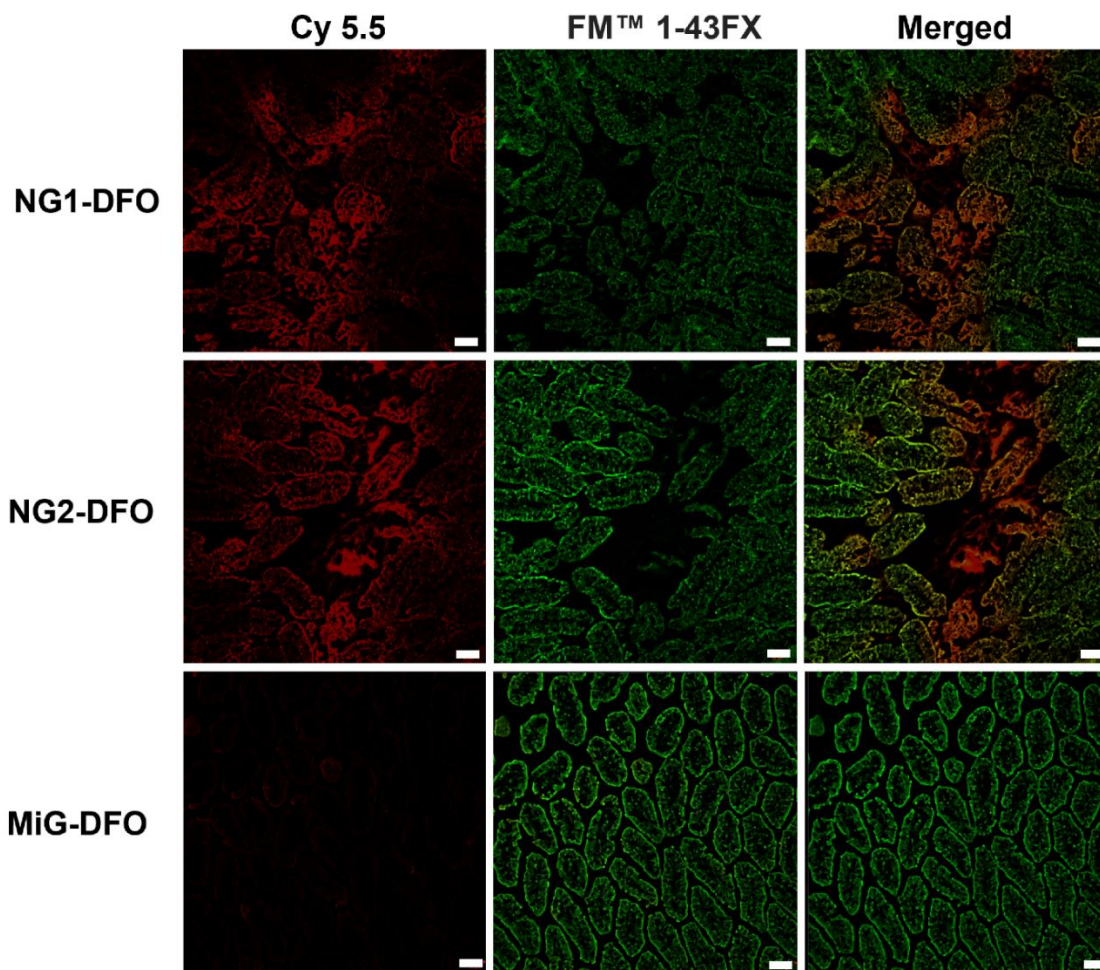
Figure 3.5. Confocal images of Cy 5.5 labeled NG/MiG-DFO in mice duodenum at 4 h (scale of 25 µm). Results reveal fluorescence from nanosized formulations entrapped between the villi of the duodenum for both NG1-DFO and NG2-DFO whereas there was no fluorescence detected in duodenum treated with MiG-DFO.

3.4.5 Safety and efficacy of NG/MiG-DFO at reducing iron absorption

The safety of NG/MiG-DFO formulations on the GI tract of mice was monitored by administering NG/MiG-DFO conjugates (500 mg/kg equivalent of DFO) every 12 h for 30 days to mice fed normal chow. After 30 days, mice were sacrificed, and stomach, small and large intestines were collected for immunohistology studies. Results indicate that there was no acute pathological sign of damage in the GI tract of animals administered NG/MiG-DFO (**Figure 3.6**), most likely because the conjugates appear to be poorly absorbed across the gut with little cumulative effect over time since all the conjugates eventually eliminate from the body.
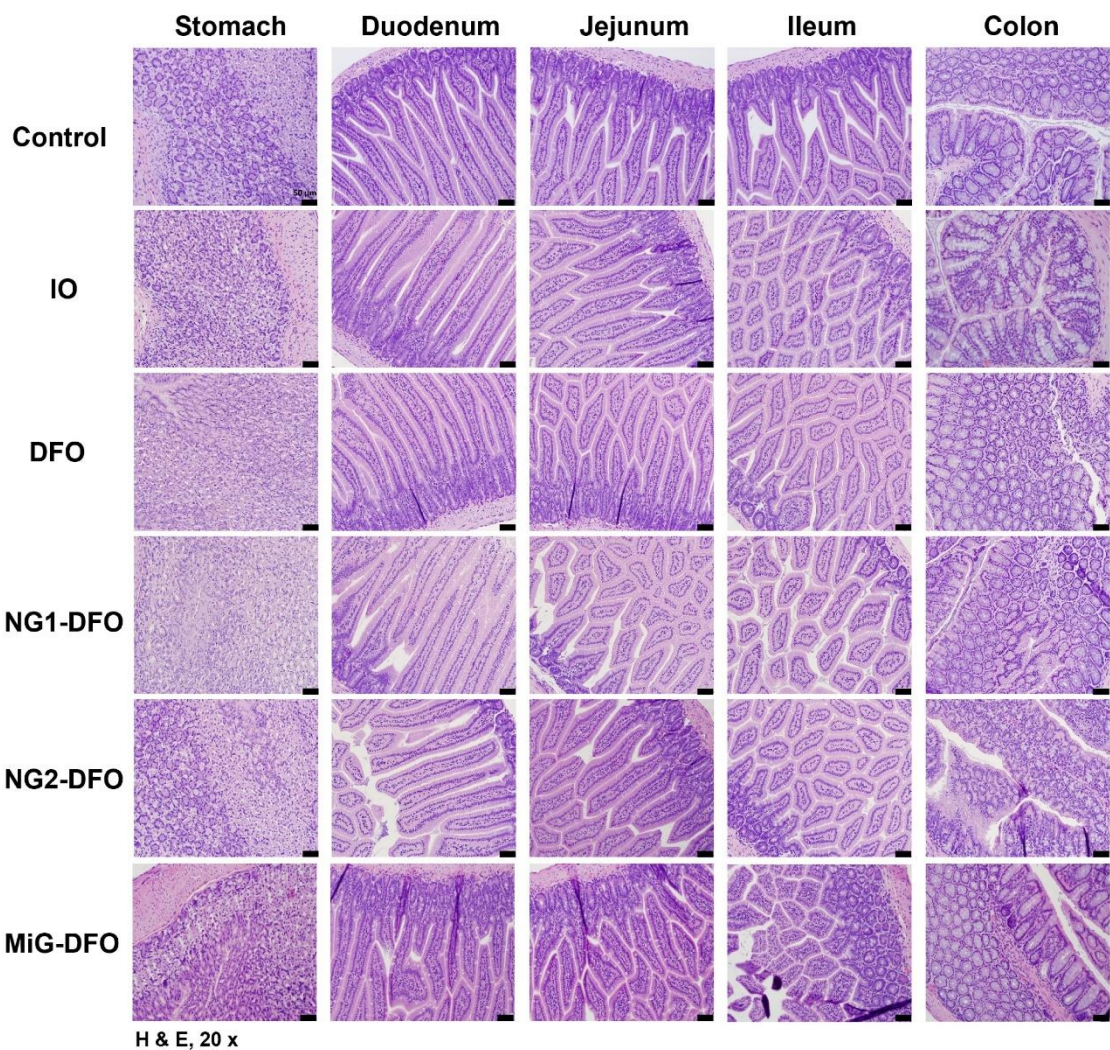
Figure 3.6. Evaluation of GI toxicity of oral gavage of DFO or NG/MiG-DFO every 12 h for 4 weeks. All groups showed no evidence o GI tract toxicity. All data shown with scale-bar of 50 µm.

A dietary iron-overload mouse model was established to examine the pathological effect of excessive dietary iron in the body. To establish the dietary iron overload mouse model, a group of female Balb/C mice (6 – 8 weeks) were fed mice chow containing 2% carbonyl iron ad libitum for 30 days. At the end of the month, mice were euthanized, and blood serum and organs were collected. Mouse ferritin ELISA confirmed that mice fed an IO diet exhibit significantly elevated

serum ferritin levels (3949 ± 48 ng/ml) to more than a 4-fold increase compared to mice fed normal chow (948 ± 78 ng/ml).

For the efficacy study (**Figure S3.6A**), mice were divided into five groups consisting of mice fed normal chow (control) and mice fed 2 % carbonyl iron chow (IO-chow plus no treatment, IO-chow plus free DFO, IO-chow plus NG1-DFO, IO-chow plus NG2-DFO, and IO-chow plus MiG-DFO). From Day 1 to Day 28 of the experiment, mice had free access to each designated chow ad libitum; treatment groups were administered free DFO or NG/MiG-DFO conjugates via oral gavage every 12 h for 4 weeks. The body weights of mice were measured and recorded every 4 days to ensure that the mice are fed regularly without high iron chow or NG/MiG-DFO conjugates induced toxicity. Result showed that mice gained weight similarly within the groups fed with normal chow or high iron chow (**Figure S3.6B**), indicating that the high iron diet or the conjugates did not induce GI discomfort. At the 2-week and 4-week timepoint, mice were fasted for 12 h prior to sacrifice and blood serum and organs (GI tract and liver) were collected. Serum ferritin was measured at 2 weeks (**Figure S3.6C**) and 4 weeks (**Figure 3.7A**) using a mouse ferritin ELISA assay and iron concentration in livers was measured through ICP-MS at week 2 (**Figure S3.6D**) and week 4 (**Figure 3.7B**). In addition, livers and duodenums were stained with Perl's iron blue for histological studies to detect iron accumulation in the tissues.

Overall, mice fed high iron diet that were administered NG/MiG-DFO exhibited significantly lower serum ferritin levels compared to untreated (IO-control) or DFO-treated animals after 2 weeks, with no statistical significance between NG and MiG-DFO formulations (**Figure S3.6C**). At 4 weeks, the serum ferritin levels from mice oral gavage with both NG1-DFO and NG2-DFO

exhibited similar ferritin levels (NG1-DFO 1562 ± 148 ng/ml, NG2-DFO 1715 ± 232 ng/ml) compared to control mice fed normal chow mice (Control, 1190 ± 75 ng/ml) but DFO-treated mice had 4 times more ferritin in their serum (6701 ± 482 ng/ml), indicating that oral gavage of free DFO was not effective at chelating dietary iron and indirectly keeping ferritin levels down. Interestingly at week 4, mice treated with MiG-DFO displayed lower ferritin levels (3229 ± 386 ng/ml) compared to untreated (8001 ± 340 ng/ml) or DFO-treated mice (6701 ± 482 ng/ml) but was significantly less effective than smaller sized NG-DFO conjugates at reducing serum ferritin levels (**Figure 3.7A**).

The efficacy of NG/MiG-DFO conjugates at reducing dietary iron absorption was also confirmed by analyzing liver iron concentration using ICP-MS (**Figure S3.6D and Figure 3.7B**). Livers from experimental groups were cryo-dried, digested, and the iron concentration was measured in each sample. Iron levels in the livers of untreated IO-mice (3359 ± 30 ppm) increased significantly to a 3-fold increase compared to that of the normal control (926 ± 158 ppm) at 4 weeks. (**Figure 3.7B**) Also, IO mice treated with free DFO showed no difference in iron concentration (3386 ± 153 ppm) compared to the untreated IO-control. On the other hand, livers of IO mice administered both NG-DFOs (NG1-DFO 1502 ± 94 ppm, NG2-DFO 1603 ± 77 ppm) and MiG-DFO (1833 ± 85 ppm) were able to similarly inhibit iron accumulation in the liver (no statistical differences).

Iron accumulation in the liver and gut was further visualized by histochemical analysis by staining the tissue with Perl's Prussian blue (**Figure 3.7C**). In the untreated IO-control liver, more clusters of blue corresponding to iron were observed (see arrows) compared to the normal control

group. Free DFO administration was ineffective at inhibiting iron uptake into the liver. On the other hand, there was no staining of iron observed in the livers of both NG1-DFO and NG2-DFO mice and only some evidence of minor iron accumulation in the liver of MiG-DFO animals. Since the duodenum of the small intestine is responsible for absorbing a vast majority of dietary iron,[46] duodenum tissues were also analyzed by histochemistry. A number of blue-stained iron clusters were observed in the villi of both untreated IO- and DFO-treated mice but there was no iron accumulation observed in the duodenum of the two NG-DFO groups. Interestingly, we did see some evidence of some iron accumulation in the duodenum of mice administered MiG-DFO.

Overall, this study demonstrates that NG/MiG-DFO conjugates may be taken prophylactically with food to reduce dietary iron absorption. Statistically there was a difference in serum ferritin reduction levels between both NG-DFO and MiG-DFO formulations although this did not translate to statistically significant differences in the liver iron concentrations measured. In spite of this, all the data does point to some advantage to using nanometer-sized particles for chelating dietary iron that could relate to their slower transit time through the GI tract. This may also partially be explained in terms of numbers of particles available for distribution and chelation of iron during the digestion of food. These formulations were administered orally to mice on an equivalent DFO basis therefore there were likely more nanometer-sized particles conjugated to DFO available compared to fewer but larger micrometer-sized DFO-conjugates prepared.
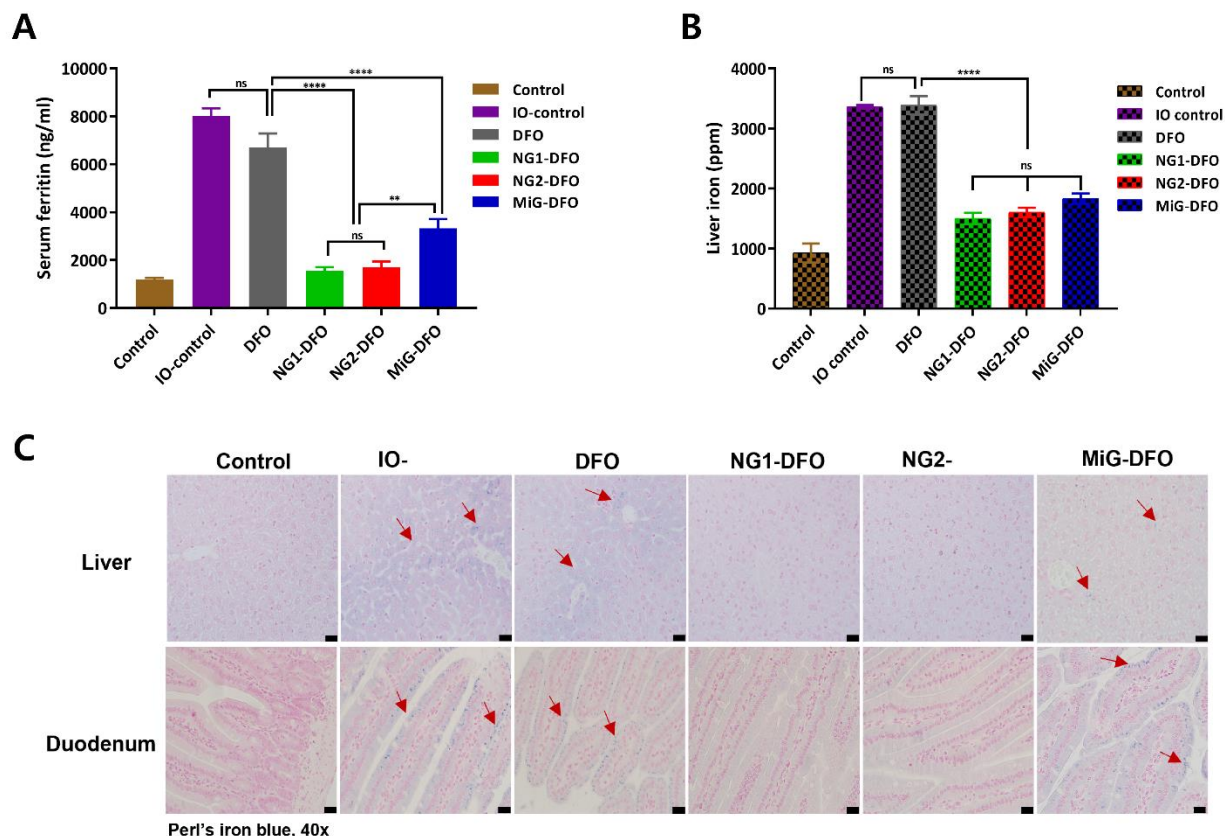
Figure 3.7. Prophylactic efficacy of dietary iron absorption of NG-DFOs and MiG-DFO conjugates were evaluated in a dietary mouse model of iron overload. After 4 weeks, mice were sacrificed, blood serums and organs were collected; (A) serum ferritin level and (B) iron concentration in the liver. (C) Efficacy of formulations at reducing iron absorption after oral gavage with NG-DFOs and MiG-DFO was assessed via histochemical staining with Perl's Prussian blue. The majority of dietary iron accumulate in the liver and in the villi of the duodenum as blue dots, see arrows. Results indicate that NG- and MiG-DFO treated conjugates can drastically help reduce accumulation of iron into these respective tissues compared to untreated IO-control and free DFO-treated mice. Data shown with scale-bar of 25 µm. All results are presented as mean ± SD (n = 6) where * p < 0.05, **p < 0.01, *** p <0.001, and ****p < 0.0001.

3.4.6 Efficacy of NG/MiG-DFO at reducing iron-induced liver damage

Increased iron accumulation into the liver can induce hepatocellular apoptosis and other related toxicity issues.[50] Excess dietary iron therefore can induce significant acute liver damage in mice. To investigate how effective prophylactic formulations are at inhibiting iron-induced liver damage, liver enzymes Alanine aminotransferase (ALT) and Aspartate transferase (AST) were measured, and the liver was H&E stained and analyzed by histopathology. There was no significant elevation of ALT and AST enzymes observed in all the mice treated after 2 weeks, however at 4 weeks the ALT level of IO-untreated mice increased approximately 4-fold and the AST level increased approximately 1.5-fold compared to the normal control (**Figure 3.8A and B**). In IO-DFO treated groups, the enzymes levels were also significantly more elevated compared to the normal control. Encouragingly in mice fed the high iron diet that were administered NG/MiG-DFO, liver enzymes were not as elevated at 2 and 4 weeks. Interestingly both NG-DFO groups showed similar enzyme levels compared to the normal control group, but MiG-DFO was statistically not as effective as the NG-DFO formulations. These results further demonstrate that NG-DFO formulations are more efficient at moderating iron-induced liver damage caused by excess dietary iron.

Iron-induced liver damage was also monitored by histopathological analyses (**Figure 3.8C**). There was notable evidence of inflammatory cells (black arrows) and apoptotic cells (red arrows) present in the liver of IO-control and DFO-treated groups whereas NG/MiG-DFO treated groups did not display such features. This is more evidence of damage or inflammation in the liver since neutrophil activity has been reported to correlate with increasing iron[50]. In the DFO treated mice,

97

there was no observable increase in inflammatory cells but there was an apparent elevation of apoptotic or necrotic cells observed. In contrast, NG/MiG-DFO treated mice livers displayed no evidence of inflammation or iron-induced liver damage to cells.
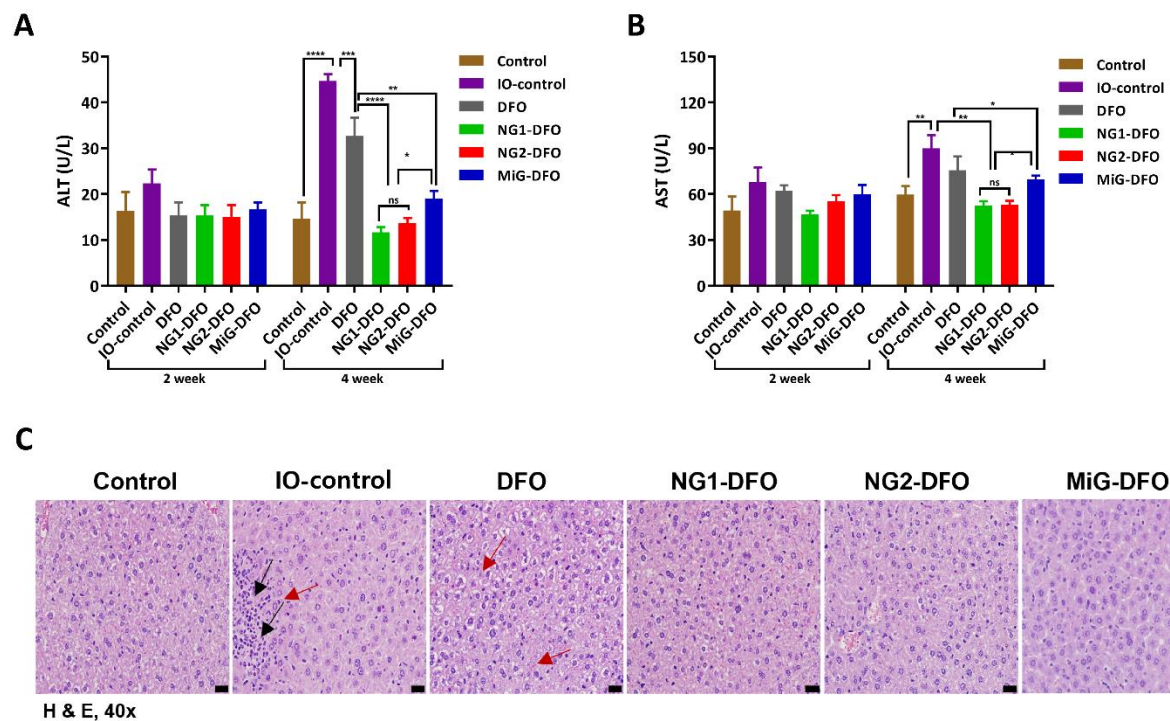
Figure 3.8. The ability to reduce iron-induced liver toxicity was confirmed in mouse livers treated with NG/MiG-DFO conjugates at 2 and 4 weeks. (A and B) Liver ALT and AST levels were significantly increased in IO and DFO groups at 4 weeks whereas NG and MiG)-DFO treated groups displayed similar levels to controls. (C) Histochemical data (scale bar of 50 µm) of mice livers at 4 weeks reveal no iron-induced toxicity in NG/MiG-DFO treated mice. All results are presented as mean ± SD (n = 6) where * $p < 0.05$, **$p < 0.01$, *** $p < 0.001$, and ****$p < 0.0001$.

3.5 Conclusions

An oral non-absorbable formulation of DFO was investigated for its ability to reduce dietary iron absorption by chelating excess iron in the gut in the presence of food containing non-heme iron. The size of these crosslinked gel formulations conjugated to DFO were prepared (NG/MiG-DFO) and their prophylactic properties were investigated in a mouse dietary model of iron overload. Free DFO was completely ineffective at reducing dietary iron absorption whereas all NG/MiG-DFO conjugates showed successful prophylactic efficacy against oral iron absorption. The larger MiG-DFO (7.4 µm) transited faster from the GI tract compared to the two NG-DFO conjugates (56 nm, 246 nm) which tended to be retained more in the villi of the duodenum, thus slowing its transit time. This slower transit time may help explain why the nanogel sized formulations were significantly more effective at chelating dietary iron based on serum ferritin concentrations and histochemical analysis of the duodenal tissue. The act of chelating dietary iron reduced acute iron-induced related accumulation and liver toxicity based on ALT/AST and liver histopathological analysis for all polymeric formulations. Overall, this non-absorbable polymeric-conjugate strategy may be a safe and feasible therapeutic option for reducing dietary non-heme iron uptake, wherein the slower transit time for nanometer-sized conjugates due to their entrapment in the gaps of the duodenal villi may be beneficial for maximizing dietary iron chelation compared to larger sized constructs.

3.6 Supplementary Information: ORALLY NON-ABSORBABLE DFO-POLYMER CONJUGATES FOR REDUCING DIETARY IRON ABSORPTION

S3.1 Materials and Instruments

Poly (ethylene glycol) diacrylate (PEG-DA, average M_n = 700), acrylamide, glycidyl methacrylate (GMA), ammonium persulfate (APS), dioctyl sulfosuccinate (AOT), Brij30, Span® 85, hexane, cyclohexane, N,N,N′,N′-tetramethylethylenediamine (TEMED), sodium periodate (NaIO$_4$), sodium cyanoborohydride (NaCNBH$_3$), glycine, EtOH, NaOH, HCl, N-ethyl-N'-(3-dimethylaminopropyl)-carbodiimide hydrochloride (EDC), N-hydroxysuccinimide, porcine pepsin, porcine pancreatin were purchased from Sigma Aldrich (St. Louis, MO). Desferrioxamine mesylate (DFO) was purchased from Hospira, Inc. (Lake Forest, IL). Human epithelial colorectal adenocarcinoma (Caco-2) cell line was purchased from American Type Culture Collection (ATCC). Dulbecco's modified eagle medium (DMEM) without pyruvate, heat-inactivated fetal bovine serum (FBS), penicillin/streptomycin solution (100×), nonessential amino acids (100×), DMSO (99.5% purity), Hank's Balanced Salt solution (HBSS), Dulbecco's Phosphate-Buffered Saline without CaCl$_2$ and MgCl$_2$, Cypate 5.5 (Cy5.5), DAPI, N-(3-triethylammoniumpropyl)-4-(4-(dibutylamino)styryl) pyridinium dibromide (FM^{TM} 1-43 FX) were purchased from Thermo Fisher scientific. Trypsin, ethylenediaminetetraacetic acid (EDTA), Corning 12-well transwell plate were purchased from Fisher Scientific. Female Balb/C mice (6 – 8 weeks) were purchased from Jackson Laboratory, USA. Mouse ELISA kit was purchased from Immunology Consultants Laboratory, INC. Rodent chow Teklad 5053 without fluorescence and iron-overload chow (Teklad 5053 + 2% carbonyl iron, TD.190344) were purchased from Envigo (Madison, Wisc, USA).

For physicochemical analysis, ^{1}H NMR spectra were obtained using a Bruker Advance 400 MHz spectrometer. Spectramax® Plus 384 Microplate Reader (Molecular Devices) were used for UV-Vis spectra analysis. ATR-CRYSTAL FTIR (Bruker) was used for the FTIR spectra analysis. LSM710 confocal microscope (Carl Zeiss) was used for confocal laser scanning microscopy (CLSM) images of samples. Transmission electron microscopy (TEM) with the instrument JEOL-JEM1011 with an acceleration voltage of 120 kV was used for morphological analysis. Particle size and Zeta potential were measured with Zeta-sizer Nano ZS instrument (Malvern).
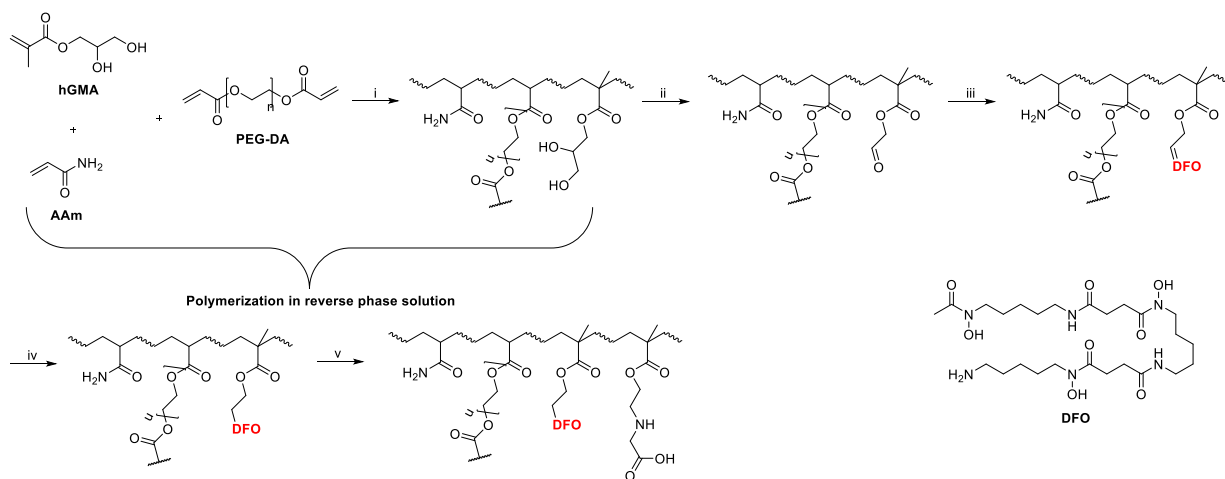
Reagents and conditions: (i)APS/TEMED, Hexane/H$_2$O, RT, overnight; (ii)NaIO$_4$, H$_2$O, RT, overnight; (iii)DFO, H$_2$O, RT, overnight; (iv)NaCNBH$_3$, H$_2$O, RT, overnight; (v)Glycine, H$_2$O, RT, overnight;

Table S3.1. Synthesis of NG or MiG-DFO conjugates. Monomers hGMA and AAm, and crosslinker PEG$_{700}$-DA were polymerized in water-in-oil (w/o) emulsions stabilized by surfactants. Polymeric scaffolds generated were then subsequently post-conjugated to DFO.
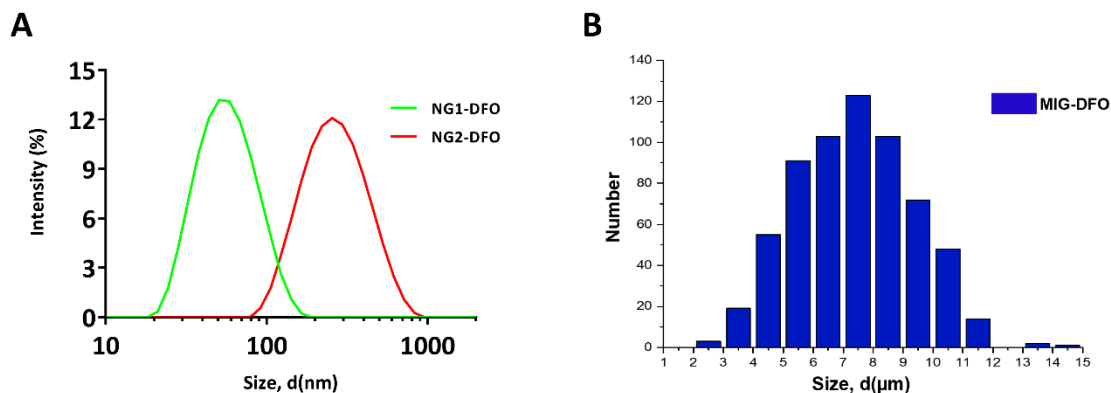
Figure S3.1. (A) Dynamic Light Scattering (DLS) data of two NG-DFO conjugates. DLS data showed sizes of NG-DFO with z-average of 56 ± 4 nm for NG1-DFO and 246 ± 8 nm for NG2-DFO. (B) MiG-DFO size was determined using ImageJ program to analyze confocal images (**Figure 2 C**). Data represents the size of MiG-DFO with z-average of 7.39 ± 1.9 µm.
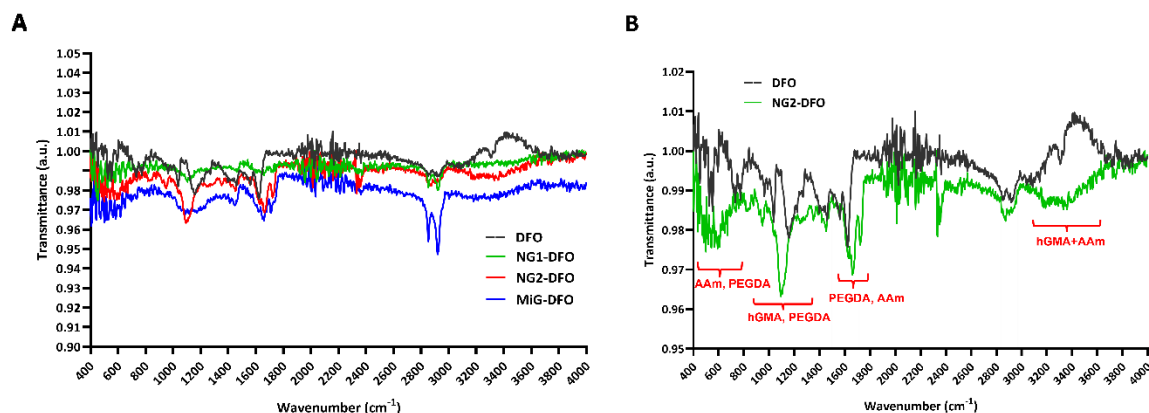
Figure S3.2. (A) FTIR spectra of NG/MiG-DFO conjugates. (B) Spectra comparison between NG2-DFO and free DFO. Peak marked in red are major peaks of monomers acrylamide (AAm) and glycidyl methacrylate (hGMA), and the crosslinker PEG-diacrylate (PEG-DA).
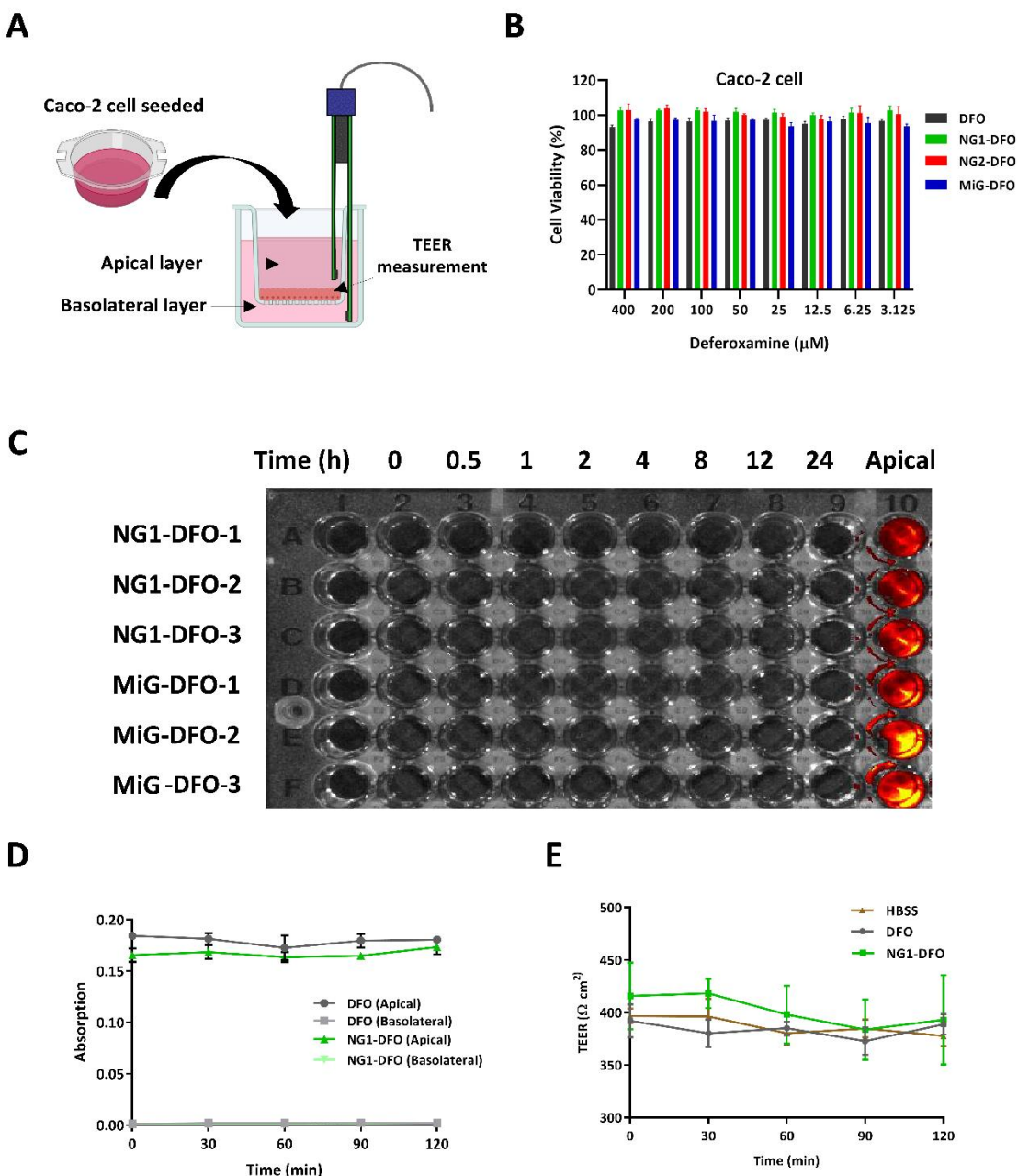
Figure S3.3. (A) The cellular permeability of NG-DFO and MiG-DFO conjugates were confirmed through caco-2 cell monolayer permeability assay. Caco-2 cells were treated with either 100 μM of equivalent DFO or NG-DFO or MiG-DFO conjugates and incubated for 24 hours. At each time point, equal amount of solution from both the apical and basolateral layers were added with Fe (III) and then tested for absorbance at 430 nm. (B) Cell viability of caco-2 cells after 24 h

incubation with free DFO or NG/MiG-DFO conjugates. (C) Basolateral fluorescence data using IVIS. Data showed that no fluorescence was observed up to 24 h timepoint for NG1 or MiG-DFO treated cells, indicating that these conjugates were not permeable through caco-2 cell monolayers. (D and E) Reduced time frame of permeability assay and TEER value measurements. In the 24 h timeframe of the same assay, DFO showed decreased TEER values and basolateral absorbance, while in this 2 h timeframe, DFO showed no permeability nor reduced TEER values.
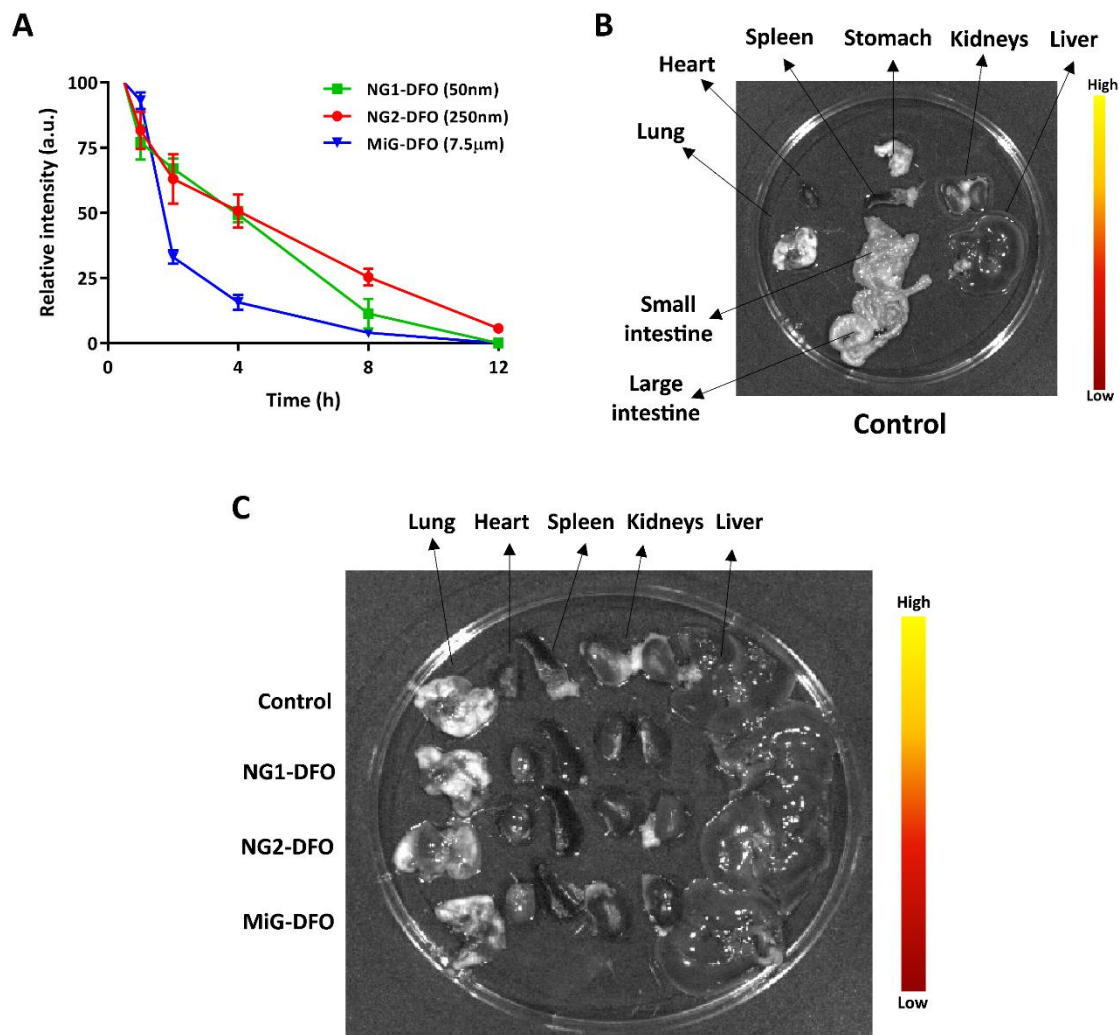
Figure S3.4. (A) Relative intensity of the fluorescence was calculated by analyzing decreasing in ROI values over time. MiG-DFO conjugate showed faster decreasing in fluorescence intensity compared to NG-DFOs. (B) Control mice will have no fluorescence observed in any organs. (C) Other organs such as liver, heart, spleen, kidney, and lung of the mice collected from all four groups did not show fluorescence, indicating that the conjugates were not absorbable by the intestine.
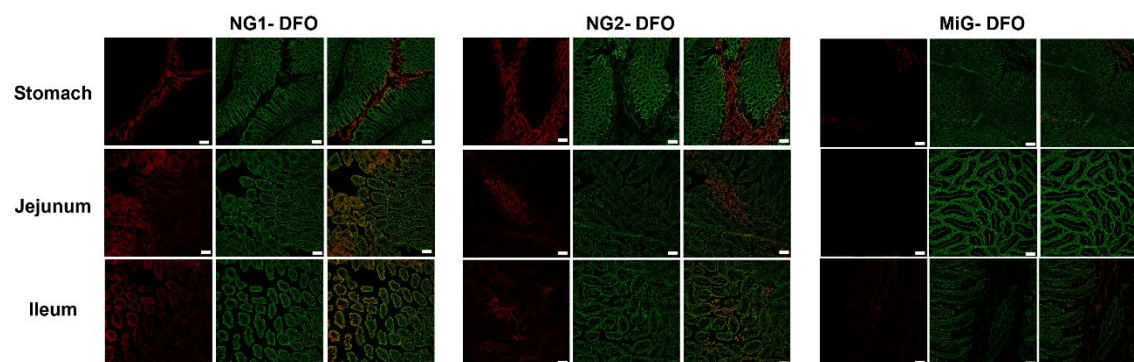
Figure S3.5. NG/MiG-DFO conjugates in other parts of GI tract. Data showed that NG1 and NG2-DFO still remained in the stomach, jejunum, and ileum after 4 h of oral gavage, while MiG-DFO was eliminated from jejunum and ileum. Although some MiG-DFO conjugate remained in the stomach, most of them was either cleared or traveled to the large intestine, indicating apparent faster clearance of MiG-DFO (Scale bar = 25 µm).
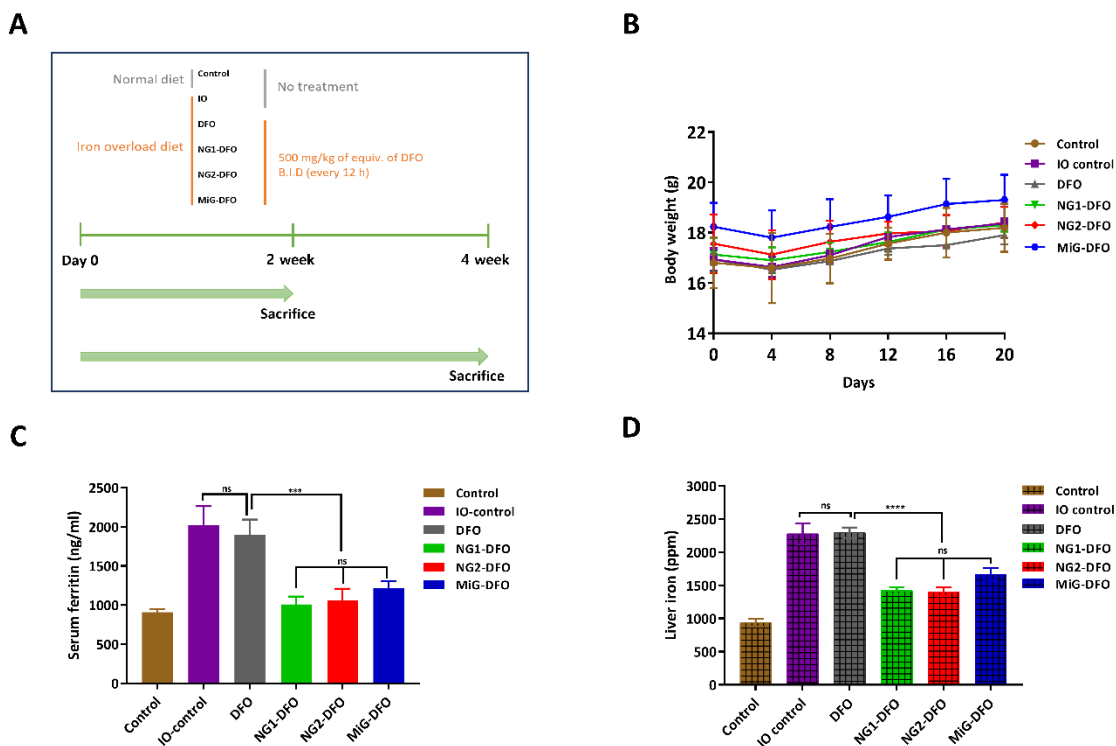
Figure S3.6. (A) The outline of in vivo efficacy study of NG/MiG-DFO conjugates in Balb/C mice. (B) Average body weight of the mice groups, (C and D) Efficacy data of NG/MiG-DFO after 2 weeks of the study. Data showed that there were significant differences between NG/MiG-DFO treated groups and free DFO-treated groups in serum ferritin levels and liver iron concentrations. However, no statistical significance was observed between NG-DFO and MiG-DFO at this time.

CHAPTER 4

CONCLUSIONS

4.1 pH-responsive Polymeric Vesicle (PV) against biofilm

The formation of biofilm, an architectural microcolony of bacteria, has become a significant burden in the healthcare industry as a result of its link to antibiotic resistance and death rate [34]. While physical removal and high-dosage interventions exhibit a certain extent of effects in combating biofilms, these methods' inability to fully eradicate biofilms result in the bacteria to gain resistance to drugs [23], and this underlines an urgent need for new therapeutic approaches to eliminate biofilm.

Here, we investigated pH-responsive "smart" polymeric vesicles (**PV**), formed from the self-association of a di-block copolymer called mPEG-*b*-p(DEAEMA), for encapsulation of the broad spectrum antibiotic apramycin (APR, as a model drug) against Pseudomonas aeruginosa biofilm. In order to address biofilm-associated multi-drug resistance (MDR), especially pertaining to the effective delivery of antibodies, the pH-responsive amphiphilic **PV** successful diffuses into the inner biofilm microenvironment and conducts controlled release of antibiotics specific to biofilm's microenvironment. With all these multifunctional advantages, we expected that **PV**, as a novel and potent nanocarrier, will generate a path towards the treatment of MDR *P. aeruginosa* biofilm-associated infections such as the urinary tract infection, as well as in ameliorating complications related to biofilm infections.

Synthesis of the polymer was conducted through RAFT polymerization followed by self-assembly into vesicles in aqueous solution. Physicochemical characterizations, including size and morphology, pH-responsive properties, and APR encapsulation efficiency were evaluated through DLS, TEM, zeta-potential analysis and TNBS-mediated UV-vis absorbance assays respectively. Antibacterial and antibiofilm assays were conducted under different pH conditions (5.0, 6.0, and 7.4) to evaluate the drug release properties of the pH-responsive vesicles. The ability of the vesicles to penetrate deep into the *P. aeruginosa* biofilm, activity against preexisting biofilms, and membrane-disrupting antibacterial properties of the vesicles were confirmed through 3D confocal microscopy and flow cytometry assays. The effects of vesicle cytotoxicity on mammalian cells in vitro were evaluated through the MTT assay.

The vesicles were characterized by an encapsulation efficiency of 48% (w/w) for apramycin and a zeta potential of +24 mV at pH 5.0. The APR-loaded vesicles decreased the MIC of the drug two-fold against *P. aeruginosa* (16 µg/ml) compared to free APR (32 µg/ml). Confocal images and flow cytometry analysis showed that the positively charged vesicles were also able to compromise the integrity of the bacterial membrane, which further enhanced the overall antibacterial efficacy observed in combination with APR. The ability of the vesicles to diffuse deep into a preexisting biofilm was confirmed through 3D confocal microscopy after incubating the biofilm with fluorophore-labeled vesicle. Efficacy against biofilm formation and ability of the APR-loaded vesicles to eradicate the preexisting biofilm was significantly improved compared to free APR or vesicle alone treatment.

In conclusion, the pH-responsive PV formed from mPEG-*b*-p(DEAEMA) significantly enhanced antibacterial and antibiofilm properties against *P. aeruginosa*. These preliminary findings may be relevant in reducing the likelihood of antibiotic resistance developing in biofilm-associated *P. aeruginosa* infections. Future directions of the study may include optimization of the vesicle for effective delivery *in vivo* to treat biofilm associated disease such as the urinary tract infections.

4.2 Prophylactic NG-DFO conjugates for dietary iron absorption

There is currently no cure for hereditary hemochromatosis (HH) due to excess dietary iron absorption and no drug on the market to prevent this type of non-transfusional iron overload (NTIO) condition. Preventative measures mainly include phlebotomy and asking HH patients to minimize dietary iron intake. In addition, traditional iron chelators such as deferoxamine (DFO) are not applicable in the treatment HH, due to their lack of efficacy in chelating dietary iron absorption. To address the unmet needs in developing an effective therapeutic approach in reducing dietary iron absorption, we proposed to investigate the feasibility of prophylactic oral non-absorbable nanogel-deferoxamine (NG-DFO) conjugates. The aim of this study was to develop diverse sizes of NG-DFO conjugates and to evaluate their retention time in the GI tract and overall long-term efficacy and safety at reducing dietary iron absorption.

Among various sizes of NG-DFO synthesized, two conjugates averaging 50 and 250 nm in diameter and bearing 16.3% and 14.9% (w/w) DFO per respective NG-DFO were investigated

further, in comparison with the larger sized microgel-DFO (MiG-DFO). Selectivity and metal competition studies with NG-DFO conjugates reveal that they can selectively chelate ferric iron. The conjugates were not cytotoxic and none of the conjugates were taken up by Caco-2 cells or penetrated the monolayer. *In vivo* studies revealed that the conjugates remained in the GI tract for approximately 12 h without being absorbed. The conjugates significantly reduced dietary iron absorption, serum ferritin and iron concentrations in the liver of Balb/C mice fed elevated iron chow for 4 weeks. Histopathology data showed that the conjugates did not induce GI toxicity and significantly reduced iron-related toxicities in the liver.

In conclusion, through this study, we confirmed that the NG-DFO conjugates displayed non-absorbable properties when orally administered, and were able to efficiently reduce dietary iron absorption, thus maintaining *in vivo* iron concentration, which further prevented iron-induced toxicities. Therefore, NG-DFO conjugates may prove useful as a potential long-term prophylactic treatment for reducing iron absorption in HH. Future directions of the study may include surface modifications of the nanogels to increase retention time in the GI tract for enhanced prophylactic efficacy.

REFERENCES

1. Begines, B., et al., *Polymeric Nanoparticles for Drug Delivery: Recent Developments and Future Prospects.* Nanomaterials, 2020. **10**(7).
2. Chan, J.M., et al., *Polymeric Nanoparticles for Drug Delivery.* Cancer Nanotechnology: Methods and Protocols, 2010. **624**: p. 163-175.
3. Elsabahy, M. and K.L. Wooley, *Design of polymeric nanoparticles for biomedical delivery applications.* Chemical Society Reviews, 2012. **41**(7): p. 2545-2561.
4. Jahangirian, H., et al., *A review of small molecules and drug delivery applications using gold and iron nanoparticles.* International Journal of Nanomedicine, 2019. **14**: p. 1633-1657.
5. Wei, H., R.X. Zhuo, and X.Z. Zhang, *Design and development of polymeric micelles with cleavable links for intracellular drug delivery.* Progress in Polymer Science, 2013. **38**(3-4): p. 503-535.
6. Hubbell, J.A. and A. Chilkoti, *Nanomaterials for Drug Delivery.* Science, 2012. **337**(6092): p. 303-305.
7. Ward, M.A. and T.K. Georgiou, *Thermoresponsive Polymers for Biomedical Applications.* Polymers, 2011. **3**(3): p. 1215-1242.
8. Lammers, T., et al., *Nanotheranostics and Image-Guided Drug Delivery: Current Concepts and Future Directions.* Molecular Pharmaceutics, 2010. **7**(6): p. 1899-1912.
9. Le, N.T.T., et al., *Recent Progress and Advances of Multi-Stimuli-Responsive Dendrimers in Drug Delivery for Cancer Treatment.* Pharmaceutics, 2019. **11**(11).
10. Ganta, S., et al., *A review of stimuli-responsive nanocarriers for drug and gene delivery.* Journal of Controlled Release, 2008. **126**(3): p. 187-204.
11. Lee, B.K., Y.H. Yun, and K. Park, *Smart nanoparticles for drug delivery: Boundaries and opportunities.* Chemical Engineering Science, 2015. **125**: p. 158-164.
12. Lee, E.S., et al., *Super pH-sensitive multifunctional polymeric micelle for tumor pH(e) specific TAT exposure and multidrug resistance.* Journal of Controlled Release, 2008. **129**(3): p. 228-236.
13. Dixon, S.J. and B.R. Stockwell, *The role of iron and reactive oxygen species in cell death.* Nature Chemical Biology, 2014. **10**(1): p. 9-17.
14. Liu, Z., et al., *Reactive Oxygen Species-Triggered Dissociation of a Polyrotaxane-Based Nanochelator for Enhanced Clearance of Systemic and Hepatic Iron.* Acs Nano, 2021. **15**(1): p. 419-433.
15. Cui, S.L., J. Qiao, and M.P. Xiong, *Antibacterial and Biofilm-Eradicating Activities of pH-Responsive Vesicles against Pseudomonas aeruginosa.* Molecular Pharmaceutics, 2022.
16. Qiao, J., S.L. Cui, and M.P. Xiong, *ROS-sensitive micelles for controlled delivery of antibiotics to combat intracellular Staphylococcus aureus-associated infections.* Journal of Materials Chemistry B, 2021. **9**(43): p. 8951-8961.
17. Hu, Q.Y., P.S. Katti, and Z. Gu, *Enzyme-responsive nanomaterials for controlled drug delivery.* Nanoscale, 2014. **6**(21): p. 12273-12286.

18. Thambi, T. and D.S. Lee, *Stimuli-responsive polymersomes for cancer therapy.* Stimuli Responsive Polymeric Nanocarriers for Drug Delivery Applications: Advanced Nanocarriers for Therapeutics, Vol 2, 2019: p. 413-438.

19. Choi, K.Y., et al., *Hyaluronic acid-based nanocarriers for intracellular targeting: Interfacial interactions with proteins in cancer.* Colloids and Surfaces B-Biointerfaces, 2012. **99**: p. 82-94.

20. Estrela, J.M., A. Ortega, and E. Obrador, *Glutathione in cancer biology and therapy.* Critical Reviews in Clinical Laboratory Sciences, 2006. **43**(2): p. 143-181.

21. Flemming, H.C., et al., *Biofilms: an emergent form of bacterial life.* Nature Reviews Microbiology, 2016. **14**(9): p. 563-575.

22. Stewart, P.S. and J.W. Costerton, *Antibiotic resistance of bacteria in biofilms.* Lancet, 2001. **358**(9276): p. 135-138.

23. Flemming, H.C. and J. Wingender, *The biofilm matrix.* Nature Reviews Microbiology, 2010. **8**(9): p. 623-633.

24. Hobley, L., et al., *Giving structure to the biofilm matrix: an overview of individual strategies and emerging common themes.* Fems Microbiology Reviews, 2015. **39**(5): p. 649-669.

25. Patel, R., *Biofilms and antimicrobial resistance.* Clinical Orthopaedics and Related Research, 2005(437): p. 41-47.

26. Michiels, J.E., et al., *In Vitro Emergence of High Persistence upon Periodic Aminoglycoside Challenge in the ESKAPE Pathogens.* Antimicrobial Agents and Chemotherapy, 2016. **60**(8): p. 4630-4637.

27. Percival, S.L., et al., *Antimicrobial tolerance and the significance of persister cells in recalcitrant chronic wound biofilms.* Wound Repair and Regeneration, 2011. **19**(1): p. 1-9.

28. Klein, R.D. and S.J. Hultgren, *Urinary tract infections: microbial pathogenesis, host-pathogen interactions and new treatment strategies.* Nature Reviews Microbiology, 2020. **18**(4): p. 211-226.

29. Delcaru, C., et al., *Microbial Biofilms in Urinary Tract Infections and Prostatitis: Etiology, Pathogenicity, and Combating strategies.* Pathogens, 2016. **5**(4).

30. Huang, D.N., et al., *Functionalized biomaterials to combat biofilms.* Biomaterials Science, 2020. **8**(15): p. 4052-4066.

31. Koo, H., et al., *Targeting microbial biofilms: current and prospective therapeutic strategies.* Nature Reviews Microbiology, 2017. **15**(12): p. 740-755.

32. Lynch, A.S. and G.T. Robertson, *Bacterial and fungal biofilm infections.* Annual Review of Medicine, 2008. **59**: p. 415-428.

33. Liu, F.Q., et al., *Quaternary Ammonium Salt-Based Cross-Linked Micelles to Combat Biofilm.* Bioconjugate Chemistry, 2019. **30**(3): p. 541-546.

34. Fulaz, S., et al., *Nanoparticle-Biofilm Interactions: The Role of the EPS Matrix.* Trends in Microbiology, 2019. **27**(11): p. 915-926.

35. Choi, W., et al., *Quantitative Interpretation of Hydration Dynamics Enabled the Fabrication of a Zwitterionic Antifouling Surface.* Acs Applied Materials & Interfaces, 2020. **12**(7): p. 7951-7965.

36. Hu, D.F., et al., *Surface Charge Switchable Supramolecular Nanocarriers for Nitric Oxide Synergistic Photodynamic Eradication of Biofilms.* Acs Nano, 2020. **14**(1): p. 347-359.

37.   Shibu, E.S., et al., *Nanomaterials formulations for photothermal and photodynamic therapy of cancer.* Journal of Photochemistry and Photobiology C-Photochemistry Reviews, 2013. **15**: p. 53-72.

38.   Ballatore, M.B., et al., *Photodynamic Inactivation of Bacteria Using Novel Electrogenerated Porphyrin-Fullerene C-60 Polymeric Films.* Environmental Science & Technology, 2015. **49**(12): p. 7456-7463.

39.   Kumar, M.S. and A.P. Das, *Emerging nanotechnology based strategies for diagnosis and therapeutics of urinary tract infections: A review.* Advances in Colloid and Interface Science, 2017. **249**: p. 53-65.

40.   Liu, Z., et al., *ROS-triggered degradable iron-chelating nanogels: Safely improving iron elimination in vivo.* Journal of Controlled Release, 2018. **283**: p. 84-93.

41.   Liu, Z., et al., *Enzymatically Biodegradable Polyrotaxane-Deferoxamine Conjugates for Iron Chelation.* Acs Applied Materials & Interfaces, 2016. **8**(39): p. 25788-25797.

42.   Liu, Z., et al., *Oxidation-Induced Degradable Nanogels for Iron Chelation.* Scientific Reports, 2016. **6**.

43.   Bahamondez-Canas, T.F., et al., *PEGylation of Tobramycin Improves Mucus Penetration and Antimicrobial Activity against Pseudomonas aeruginosa Biofilms in Vitro.* Molecular Pharmaceutics, 2018. **15**(4): p. 1643-1652.

44.   Knop, K., et al., *Poly(ethylene glycol) in Drug Delivery: Pros and Cons as Well as Potential Alternatives.* Angewandte Chemie-International Edition, 2010. **49**(36): p. 6288-6308.

45.   Kocak, G., C. Tuncer, and V. Butun, *pH-Responsive polymers.* Polymer Chemistry, 2017. **8**(1): p. 144-176.

46.   Brissot, P., et al., *Haemochromatosis.* Nature Reviews Disease Primers, 2018. **4**.

47.   Ceci, A., et al., *Pharmacotherapy of iron overload in thalassaemic patients.* Expert Opinion on Pharmacotherapy, 2003. **4**(10): p. 1763-1774.

48.   Powell, L.W., R.C. Seckington, and Y. Deugnier, *Haemochromatosis.* Lancet, 2016. **388**(10045): p. 706-716.

49.   Utzschneider, K.M. and K.V. Kowdley, *Hereditary hemochromatosis and diabetes mellitus: implications for clinical practice.* Nature Reviews Endocrinology, 2010. **6**(1): p. 26-33.

50.   Wood, M.J., R. Skoien, and L.W. Powell, *The global burden of iron overload.* Hepatology International, 2009. **3**(3): p. 434-444.

51.   Wang, J.A. and K. Pantopoulos, *Regulation of cellular iron metabolism.* Biochemical Journal, 2011. **434**: p. 365-381.

52.   Buss, J.L., F.M. Torti, and S.V. Torti, *The role of iron chelation in cancer therapy.* Current medicinal chemistry, 2003. **10**(12): p. 1021-1034.

53.   Buss, J.L., et al., *Iron chelators in cancer chemotherapy.* Current topics in medicinal chemistry, 2004. **4**(15): p. 1623-1635.

54.   Lee, P., et al., *Intravenous-Infusion Pharmacokinetics of Desferrioxamine in Thalassemic Patients.* Drug Metabolism and Disposition, 1993. **21**(4): p. 640-644.

55.   Jahangirian, H., et al., *A review of small molecules and drug delivery applications using gold and iron nanoparticles.* International journal of nanomedicine, 2019. **14**: p. 1633.

56.   Bentur, Y., M. McGuigan, and G. Koren, *Deferoxamine (desferrioxamine). New toxicities for an old drug.* Drug Saf, 1991. **6**(1): p. 37-46.

57.   Hallaway, P.E., et al., *Modulation of Deferoxamine Toxicity and Clearance by Covalent Attachment to Biocompatible Polymers.* Proceedings of the National Academy of Sciences of the United States of America, 1989. **86**(24): p. 10108-10112.

58.   Liu, Z., et al., *Multifunctional Polymeric Micelles for Combining Chelation and Detection of Iron in Living Cells.* Advanced Healthcare Materials, 2017. **6**(17): p. 1700162.

59.   Liu, Z., et al., *ROS-triggered degradable iron-chelating nanogels: Safely improving iron elimination in vivo.* J Control Release, 2018. **283**: p. 84-93.

60.   Liu, Z., et al., *Enzymatically Biodegradable Polyrotaxane–Deferoxamine Conjugates for Iron Chelation.* ACS Applied Materials & Interfaces, 2016. **8**(39): p. 25788-25797.

61.   Ooya, T. and N. Yui, *Synthesis and characterization of biodegradable polyrotaxane as a novel supramolecular-structured drug carrier.* Journal of Biomaterials Science, Polymer Edition, 1997. **8**(6): p. 437-455.

62.   Martins, M., et al., *Presence of Extracellular DNA in the Candida albicans Biofilm Matrix and its Contribution to Biofilms.* Mycopathologia, 2010. **169**(5): p. 323-331.

63.   Qao, J., et al., *Terpyridine-Micelles for Inhibiting Bacterial Biofilm Development.* Acs Infectious Diseases, 2018. **4**(9): p. 1346-1354.

64.   Cole, S.J., et al., *Catheter-Associated Urinary Tract Infection by Pseudomonas aeruginosa Is Mediated by Exopolysaccharide-Independent Biofilms.* Infection and Immunity, 2014. **82**(5): p. 2048-2058.

65.   Ciofu, O. and T. Tolker-Nielsen, *Tolerance and Resistance of Pseudomonas aeruginosa Biofilms to Antimicrobial Agents-How P. aeruginosa Can Escape Antibiotics.* Frontiers in Microbiology, 2019. **10**.

66.   Lin, S.P., et al., *Phenotypic detection and polymerase chain reaction screening of extended-spectrum beta-lactamases produced by Pseudomonas aeruginosa isolates.* Journal of Microbiology Immunology and Infection, 2012. **45**(3): p. 200-207.

67.   Mulcahy, L.R., V.M. Isabella, and K. Lewis, *Pseudomonas aeruginosa Biofilms in Disease.* Microbial Ecology, 2014. **68**(1): p. 1-12.

68.   Qiao, J., et al., *Synthesis and evaluation of an amphiphilic deferoxamine:gallium-conjugated cationic random copolymer against a murine wound healing infection model of Pseudomonas aeruginosa.* Acta Biomaterialia, 2021. **126**: p. 384-393.

69.   Lee, N.Y., W.C. Ko, and P.R. Hsueh, *Nanoparticles in the Treatment of Infections Caused by Multidrug-Resistant Organisms.* Frontiers in Pharmacology, 2019. **10**.

70.   Xiong, M.H., et al., *Bacteria-Responsive Multifunctional Nanogel for Targeted Antibiotic Delivery.* Advanced Materials, 2012. **24**(46): p. 6175-6180.

71.   Pang, X., et al., *Bacteria-Responsive Nanoliposomes as Smart Sonotheranostics for Multidrug Resistant Bacterial Infections.* Acs Nano, 2019. **13**(2): p. 2427-2438.

72.   Zhou, J.Y., et al., *Characterization and optimization of pH-responsive polymer nanoparticles for drug delivery to oral biofilms.* Journal of Materials Chemistry B, 2016. **4**(18): p. 3075-3085.

73.   Li, P.L., et al., *Design of pH-Responsive Dissociable Nanosystem Based on Carbon Dots with Enhanced Anti-biofilm Property and Excellent Biocompatibility.* Acs Applied Bio Materials, 2020. **3**(2): p. 1105-1115.

74.   Ye, M.Z., et al., *pH-Responsive Polymer-Drug Conjugate: An Effective Strategy to Combat the Antimicrobial Resistance.* Advanced Functional Materials, 2020. **30**(39).

75.   Stoodley, P., et al., *Biofilms as complex differentiated communities.* Annual Review of Microbiology, 2002. **56**: p. 187-209.

76. Fulaz, S., et al., *Ratiometric Imaging of the in Situ pH Distribution of Biofilms by Use of Fluorescent Mesoporous Silica Nanosensors.* Acs Applied Materials & Interfaces, 2019. **11**(36): p. 32679-32688.

77. Qiao, J., et al., *Antibacterial and potentiation properties of charge-optimized polyrotaxanes for combating opportunistic bacteria.* Journal of Materials Chemistry B, 2018. **6**(33): p. 5353-5361.

78. Ashok, B., et al., *In vitro characterization of PEGylated phospholipid micelles for improved drug solubilization: Effects of PEG chain length and PC incorporation.* Journal of Pharmaceutical Sciences, 2004. **93**(10): p. 2476-2487.

79. Kang, A.D., et al., *Invitro Apramycin Activity against multidrug-resistant Acinetobacter baumannii and Pseudomonas aeruginosa.* Diagn Microbiol Infect Dis, 2017. **88**(2): p. 188-191.

80. Sashidhar, R.B., A.K. Capoor, and D. Ramana, *Quantitation of Epsilon-Amino Group Using Amino-Acids as Reference-Standards by Trinitrobenzene Sulfonic-Acid - a Simple Spectrophotometric Method for the Estimation of Hapten to Carrier Protein Ratio.* Journal of Immunological Methods, 1994. **167**(1-2): p. 121-127.

81. Geisow, M.J., *Fluorescein Conjugates as Indicators of Subcellular Ph - a Critical-Evaluation.* Experimental Cell Research, 1984. **150**(1): p. 29-35.

82. Abbaszadegan, A., et al., *The Effect of Charge at the Surface of Silver Nanoparticles on Antimicrobial Activity against Gram-Positive and Gram-Negative Bacteria: A Preliminary Study.* Journal of Nanomaterials, 2015. **2015**.

83. Slavin, Y.N., et al., *Metal nanoparticles: understanding the mechanisms behind antibacterial activity.* Journal of Nanobiotechnology, 2017. **15**.

84. Khalikova, E., P. Susi, and T. Korpela, *Microbial dextran-hydrolyzing enzymes: Fundamentals and applications.* Microbiology and Molecular Biology Reviews, 2005. **69**(2): p. 306-+.

85. Gebreyohannes, G., et al., *Challenges of intervention, treatment, and antibiotic resistance of biofilm-forming microorganisms.* Heliyon, 2019. **5**(8).

86. Situ, J.Q., et al., *Specific targeting of A54 homing peptide-functionalized dextran-g-poly(lactic-co-glycolic acid) micelles to tumor cells.* International Journal of Nanomedicine, 2015. **10**: p. 665-675.

87. Andrews, N.C., *Disorders of iron metabolism.* N Engl J Med, 1999. **341**(26): p. 1986-95.

88. Borgna-Pignatti, C., *Modern treatment of thalassaemia intermedia.* Br J Haematol, 2007. **138**(3): p. 291-304.

89. Aessopos, A., M. Kati, and D. Farmakis, *Heart disease in thalassemia intermedia: a review of the underlying pathophysiology.* Haematologica, 2007. **92**(5): p. 658-65.

90. Aessopos, A., et al., *Cardiac involvement in sickle beta-thalassemia.* Ann Hematol, 2009. **88**(6): p. 557-64.

91. Brissot, P., et al., *Haemochromatosis.* Nat Rev Dis Primers, 2018. **4**: p. 18016.

92. Pippard, M.J., et al., *Iron absorption and loading in beta-thalassaemia intermedia.* Lancet, 1979. **2**(8147): p. 819-21.

93. Pootrakul, P., et al., *The effect of erythroid hyperplasia on iron balance.* Blood, 1988. **71**(4): p. 1124-9.

94. Kontoghiorghe, C.N. and G.J. Kontoghiorghes, *Efficacy and safety of iron-chelation therapy with deferoxamine, deferiprone, and deferasirox for the treatment of iron-loaded*

patients with non-transfusion-dependent thalassemia syndromes. Drug Des Devel Ther, 2016. **10**: p. 465-81.

95. Cuthbert, J.A., *Iron, HFE, and hemochromatosis update.* J Investig Med, 1997. **45**(9): p. 518-29.

96. Ghisalberti, C.A., et al., *Nonabsorbable Iron(III) binding polymers: Synthesis and evaluation of the chelating properties.* Polymer Testing, 2020. **90**.

97. Wang, Y., et al., *Nanogel-DFO conjugates as a model to investigate pharmacokinetics, biodistribution, and iron chelation in vivo.* International Journal of Pharmaceutics, 2018. **538**(1-2): p. 79-86.

98. Maisel, K., et al., *Nanoparticles coated with high molecular weight PEG penetrate mucus and provide uniform vaginal and colorectal distribution in vivo.* Nanomedicine, 2016. **11**(11): p. 1337-1343.

99. Xu, Q.G., et al., *Impact of Surface Polyethylene Glycol (PEG) Density on Biodegradable Nanoparticle Transport in Mucus ex Vivo and Distribution in Vivo.* Acs Nano, 2015. **9**(9): p. 9217-9227.

100. ul-haq, M.I., et al., *Design of Long Circulating Nontoxic Dendritic Polymers for the Removal of Iron in Vivo.* Acs Nano, 2013. **7**(12): p. 10704-10716.

101. Hubatsch, I., E.G.E. Ragnarsson, and P. Artursson, *Determination of drug permeability and prediction of drug absorption in Caco-2 monolayers.* Nature Protocols, 2007. **2**(9): p. 2111-2119.

102. Srinivasan, B., et al., *TEER Measurement Techniques for In Vitro Barrier Model Systems.* Jala, 2015. **20**(2): p. 107-126.

103. Ayala, J.E., et al., *Standard operating procedures for describing and performing metabolic tests of glucose homeostasis in mice.* Disease Models & Mechanisms, 2010. **3**(9-10): p. 525-534.

104. Porter, J.B., et al., *A trial to investigate the relationship between DFO pharmacokinetics and metabolism and DFO-related toxicity.* Cooleys Anemia, 1998. **850**: p. 483-487.

105. Di Nicola, M., et al., *Functional and Structural Abnormalities in Deferoxamine Retinopathy: A Review of the Literature.* Biomed Research International, 2015.